VRIJE UNIVERSITEIT BRUSSEL

Graduation thesis submitted in partial fulfilment of the requirements for the degree of Master in Science: Physics and Astronomy

INVESTIGATION OF THE RADAR SIGNAL PROPERTIES OF NEUTRINO-INDUCED PARTICLE CASCADES IN ICE USING MARES

Jannes Loonen

June 2024

Promotors: Prof. Dr. Krijn de Vries   Prof. Dr. Nick van Eijndhoven
Supervisor: Enrique Huesca Santiago

Sciences & Bio-Engineering Sciences

Abstract

High-energy neutrinos form an ideal cosmic messenger to probe the high-energy universe. As such, detecting these weakly interacting particles is crucial. A neutrino will induce a high-energy particle cascade upon interaction with a dense medium, like ice. This cascade can be detected utilizing the commonly used optical Cherenkov or Askaryan radio detectors. In this thesis, a third novel detection technique is investigated based on radar. With radar, the ionization trail left in the wake of the high-energy particle cascade is detected instead of the actual cascade itself. A detailed study is performed on the radar signal properties of neutrino-induced particle cascades in ice using an existing simulation software called MARES. A well-chosen bistatic radar setup is fixed for all simulations which allows for a straightforward interpretation of the geometrical setup. The main quantity of interest is the amplitude of the waveform or peak voltage. It is investigated how the observed peak voltage changes depending on the direction of the cascade but also other quantities like the lifetime of the electrons making up the ionization trail are investigated. Probing the peak voltage as a function of the cascade direction reveals three distinct features and the main goal was to identify their physical origin. It became clear from numerous simulations that the three effects at play are Cherenkov effects, diffraction, and phase coherence within the ionization trail. To confirm the latter effect, a mathematical expression was derived to be able to describe the amount of phase coherence inside the ionization trail at a certain time. Comparing the phase coherence with the peak voltage as a function of the cascade direction revealed similar patterns indicating that phase coherence is one of the major effects driving the observed radar signals. Still, it was concluded that there is often a rather complex interplay between the three different effects at once.

Acknowledgements

I want to start by thanking my promoters Prof. Dr. Krijn de Vries and Prof. Dr. Nick van Eijndhoven. They were always able to ask me the right questions during our weekly meetings, reminding me to stay critical of my work. Their enthusiasm and interest in the results I presented during these meetings kept me motivated throughout the entire year. I want to express my gratitude to my supervisor Enrique Huesca Santiago. His enormous patience during our hours-long meetings helping me to get set up with the MARES software and the cluster, learning how to use GitHub and answering all of my questions was unprecedented. Working together with all three of you throughout this entire year was not only educational but also pleasant. You have helped me to become the scientist that I am today, for which I'm very grateful.

I would like to thank my fellow students and friends. These past five years have been hard, but struggling through them with all of you made it much easier. I will cherish the fun lunch and train talks we had as well as the card games we played to kill the long breaks we had between lectures. I want to thank all of you for creating an atmosphere in which I was able to be myself and grow into the person I have become today.

Finally, I want to thank my parents and sister for their love and support for all these years. Even though physics is often puzzling to you, you always tried to understand and listen to what I had to say. You were there when I needed a sympathetic ear and ventilated my frustrations. Mama, Papa and Jone thank you.

Contents

Chapter 1

Introduction

The neutrino is probably one of the most shy family members of the Standard Model [1]. The existence of neutrinos was already predicted in the early twentieth century when radioactive decay was discovered, but it took almost 50 years before they were discovered experimentally [2]. Despite being present in large numbers in the universe, they are hard to detect due to their weakly interacting nature. Because of that, they are probably among the least understood particles in the Standard Model. They exist in three different flavours that oscillate from one to another when propagating. This oscillatory behaviour was discovered in 2001 [3] and proved neutrinos are massive particles. This discovery raised a new question: are neutrinos Dirac or Majorana particles? The Standard model treats neutrinos as Dirac particles, implying that anti-neutrinos are fundamentally different from neutrinos. Still, neutrinos are the only known particles that could be Majorana in nature meaning that the particle is its own anti-particle. If Majorana particles, a natural explanation for the observed lightness of neutrinos would arise from the so-called seesaw mechanism [1]. Until the present day, the nature of the neutrino remains an open question. A different unknown about the neutrinos is their absolute mass as neutrino oscillation experiments are only able to determine the mass squared difference between the different neutrino flavours [1].

Still, even though neutrinos are not yet fully understood, their observation can answer some open questions in other branches of physics. Cosmic rays are charged particles that are constantly bombarding the Earth's atmosphere. They consist mainly of protons but can be heavier nuclei as well and appear over a vast energy range. When a cosmic ray interacts with a molecule in the atmosphere, it results in a so-called air shower. This name is chosen appropriately as the interaction of the cosmic ray leads to a chain reaction in which lots of secondary particles are produced. Drawing the tracks of all these secondary particles resembles the water droplets from an actual shower. Cosmic rays are observed to have energies starting from 10^9 eV up to 10^{20} eV[1] [4]. The origin of the ultra-high-energy cosmic rays (UHECRs) with energies $E > 10^{18}$ eV still forms a major open question as it is unknown which mechanism in the universe can produce these cosmic rays. Unravelling this mystery is hard as the flux of these UHECRs drops quickly resulting in the need for large-scale detectors. On top of that, cosmic rays are charged particles and are therefore deflected by the numerous magnetic fields they come across when travelling towards Earth. Hence, cosmic rays do not point straight back towards their source. Fortunately, there seems to be a way to resolve this. UHECRs can interact with the ambient gas at their production site. This leads mainly to the production of both neutral and charged pions that subsequently decay in gamma-ray photons and high-energy neutrinos. The benefit of gamma rays and neutrinos is that they are not deflected by magnetic fields and point straight back towards their source. Due to their common origin, observing these gamma rays and neutrinos provides a possibility to solve the mystery of the origin of UHECRs. Unfortunately, gamma rays suffer from absorption and scattering effects when travelling towards Earth and could lead to not observing the radiation. Neutrinos do not suffer from this as they are weakly interacting. Therefore, they can easily pass through lots of interstellar gas unharmed. This is both a benefit and downside of neutrinos. On the one side, neutrinos produced at far away distances will easily reach Earth, but once they do, they are difficult to detect.

[1] The corresponding flux values at those energies are 1 particle per m^2 per second at 10^9 eV and 1 particle per km^2 per century at 10^{20} eV [4].

As high-energy neutrinos provide a candidate to solve the mysteries around UHECRs, detecting them is crucial. At present day, there exist multiple techniques for detecting high-energy neutrinos [5]. All these techniques try to detect, in some way or another, the secondary particles produced when the neutrino interacts with its surroundings. This interaction leads to a particle cascade similar to the one from cosmic rays. When the neutrino interacts, preferably in a dense and signal transparent medium, like for instance ice, secondary particles are produced. These particles move at relativistic speeds through the ice and interact with the ice molecules to produce more particles. This results in a cascade-like effect and an extensive amount of highly energetic particles. Due to their relativistic speeds, the secondary particles will emit Cherenkov radiation, a radiation mechanism that only occurs in a relativistic context [6]. The Cherenkov light can be detected using optical sensors. The IceCube Neutrino Observatory [7] is an example of an experiment that adopts this technique. When the secondary particles travel through the ice, they can strip off electrons creating a negative charge excess in the cascade front. The coherent Cherenkov radio emission from these particles can be detected using radio antennas and is called Askaryan radiation. The Radio Neutrino Observatory in Greenland (RNO-G) [8] is an example of an experiment aiming to detect neutrinos through the Askaryan radio emission. A third novel detection technique is presented in this thesis. When the energetic secondary particles travel through the medium, they leave behind a dense trail of ionized electrons. Recent work [9] has proven that this macroscopic ionization trail can be detected using classical radar techniques. In this thesis, a detailed study is conducted of the radar echo signal properties from neutrino-induced particle cascades in ice. This forms the first steps towards reconstructing the properties of the primary neutrino, i.e. the energy and arrival direction, and forms the basis for the future Radar Echo Telescope for Neutrinos (RET-N) [10, 11]. The signal properties are studied using a novel simulation software called MARES: A Macroscopic Approach to the Radar Echo Scatter from high-energy particle cascades [12]. This software treats the passage of the particle cascade through the medium fully analytically instead of via Monte Carlo techniques. The fact that MARES is analytical and written in C++, makes it a fast simulation tool.

In Chapter 2, a brief history of astroparticle physics is given and the different cosmic messengers forming the branches of multi-messenger astronomy are outlined.

In Chapter 3, the focus is directed to neutrino astronomy in particular, covering the different detection techniques for neutrinos in detail and some of the major experiments adopting these techniques.

In Chapter 4, the theory behind the simulation software MARES is explained. The first step in completing this thesis was reproducing some of the previous results obtained using the MARES software. These results are shown and discussed. On top of that, some new results are found regarding the required simulation dimension in MARES. The relation between the primary energy of the neutrino and the maximum number of electrons alive in the ionization trail as well as the relation between the primary energy and the peak voltage of the radar echo signal is investigated.

In Chapter 5, a detailed study of the radar echo signal properties is performed. This study uses MARES to simulate the events, but extensive additional code was written in Python in order to analyze the simulated data and make conclusions. In this chapter, the effect of the cascade direction on the radar echo signal for a fixed and well-chosen bistatic radar setup is probed. This study led to the creation of the so-called 2D peak voltage plot. In this plot, three distinct and non-trivial features were discovered and the main goal of this thesis was to find their physical origin. As it turned out, slit-like diffraction, Cherenkov effects and phase coherence are the three main contributions that are believed to be working together in a non-trivial way in certain situations. These conclusions were made, based on extensive research of the effects of certain parameters on the simulations, by transforming the time series to a frequency domain using a Fourier transformation and by investigating the phase information inside the ionization trail. From the latter, a parametrization was developed for the phase coherence that shows similar patterns as the peak voltage shows for different cascade directions in the so-called angular plots.

Chapter 2

Astroparticle physics and multi-messenger astronomy

2.1 A brief history of astroparticle physics

The birth of astroparticle physics took place in 1912 when Victor Hess discovered cosmic rays (CRs) [4, 13, 14, 15]. At the beginning of the 20$^{\text{th}}$ century, scientists discovered that their electroscopes[1] discharged over time without any external contact but air. It was believed that this effect was induced by the ionising radiation of radioactive elements in Earth's crust, slightly ionising the air. As the flux of these ionising particles would decrease with increasing altitude, it was expected to see the effect fade away when performing measurements higher up in the atmosphere. As such, Victor Hess performed his famous balloon experiments in 1912 trying to measure the amount of ionisation in the air at different altitudes. He came to the surprising discovery that after reaching an altitude of around 2 km, the ionisation levels increase. This proved that the source responsible for the ionisation of the air is not of terrestrial origin at this altitude, but rather of cosmic origin. Two years later, a different scientist named Werner Kohlhöster confirmed Hess's discovery by performing measurements at even higher altitudes. In Figure 2.1, the measurements of both Hess and Kohlhöster are shown. After a break in fundamental research due to World War I, numerous other experiments were conducted in the subsequent years confirming the conclusion of Hess and Kohlhöster. In 1927, Skobeltzyn, took the first picture of the tracks of cosmic rays using a Wilson cloud chamber[2] and it was established that Earth is constantly bombarded with charged particles.

The discovery of cosmic rays proved that there must be extraterrestrial sources producing energetic charged particles. This was a standalone important discovery, but on top of that, also led to significant new insights in the field of fundamental particle physics and the zoo of particles and their interactions it tries to describe [4, 13]. From the Wilson cloud chambers, it was established that the ionizing particles detected using these devices were not necessarily the so-called primary, or original, particles, but quite often the secondary particles produced in the interaction of the primary. When a primary particle enters the Earth's atmosphere, it can interact with the atoms within and produce new particles. By using the cloud chamber in combination with a magnetic field, various elementary particles like pions and kaons as well as the positron were discovered. The secondary particles can subsequently decay and their daughter particles can once again undergo interactions within the atmosphere. This leads to a cascade-like effect and the development of a so-called extensive air shower, for the first time discovered in 1938 by Pierre Auger and his group [16]. In the period from 1930 up until World War II, cosmic ray physics was the ideal field to study fundamental particle physics as the accelerators available at the time could not reach the energies of the secondaries from cosmic rays interactions. Starting in 1950, particle accelerators became powerful enough to compete in energy with cosmic ray experiments and study the interactions under controlled conditions. As such, cosmic rays, and in general astroparticle physics, became less popular as most particle physicists went to accelerator

[1] An electroscope is an old scientific device used to measure the amount of electric charge present on an object via its movement induced by the electrostatic force.

[2] A cloud chamber is a device that highlights the tracks of particles by means of condensing water vapour and was invented by Charles Thomson Rees Wilson [13].

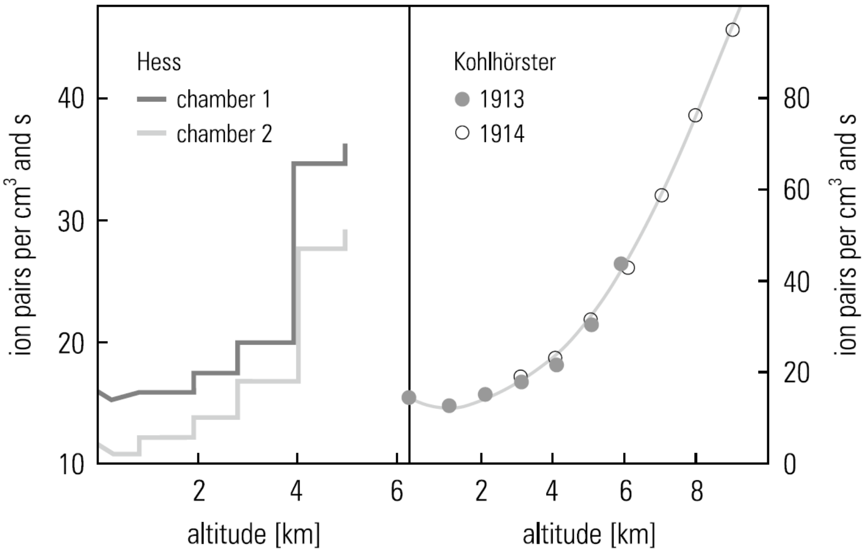

Figure 2.1: The flux of ionising particles as a function of atmospheric altitude. Measurements of Hess (*left*) and Kohlhörster (*right*). Figure from [14].

experiments [4].

After a period of approximately 30 years, in 1980, astroparticle physics was reborn [4, 13]. Thanks to significant progress in other fields like particle physics, establishing the Standard Model, and cosmology, discovering the Cosmic Microwave Background (CMB) [17] and building the ΛCDM Big Bang model [18], the field of astroparticle physics made a comeback. In order to explain for example Big Bang nucleosynthesis[3] and dark matter, elements from both cosmology and particle physics are needed [4]. An important example that led to the revival of the field in the eighties, was the observation of SN 1987A in the Large Magellanic Cloud and the accompanying burst of extragalactic neutrinos [20]. An upper limit on the neutrino mass could be derived from the arrival time, and the fact that the source was extragalactic, allowed for finding a lower limit on the neutrino lifetime [14]. On top of that, gamma-ray emission from the event proved that heavy elements like iron and nickel were produced in the explosion which was in good agreement with the existing supernova models, like for example neutrino-driven explosions [21].

Over the past four decades, astroparticle physics has grown into an interdisciplinary field between particle physics, cosmology, and astrophysics. It does not only study cosmic rays - consisting of protons, heavier nuclei, electrons and positrons - but also gamma rays and neutrinos, across a wide range of energies. All of these particles can come from different sources like the Sun, supernovae (SNe), Active Galactic Nuclei (AGN), Gamma-ray Bursts (GRBs) and more. Therefore, a rich pool of phenomena can be studied with astroparticle physics. In addition, as physics is probed at energies higher than what can typically be achieved in accelerators, studies beyond Standard Model physics are also part of astroparticle physics. Examples are neutrino oscillations [1], dark matter [14], and magnetic monopoles [14]. From the above, it is clear that astroparticle physics is an elaborate field and closely related to multi-messenger astronomy.

2.2 Multi-messenger astronomy

The word astronomy is often colloquially associated with looking at stars through an optical telescope, but astronomy is much broader than that. The optical light humans can perceive is only a very small fraction of the entire electromagnetic (EM) spectrum. As such, there exist multiple different observatories that investigate the cosmos in different wavelength bands. Below, a list is given of some observatories for each frequency domain. It should be noted that this list is not exhaustive and arbitrarily composed.

[3]Big Bang nucleosynthesis is a subfield in nuclear physics that tries to explain the primordial abundances of chemical elements like hydrogen, deuterium and lithium from neutron capture processes happening during the earliest stages of the universe [19].

1. **Radio** observatory: Very Large Array (VLA) [22]
2. **Microwave** observatory: Planck Space Observatory [23]
3. **Infrared** observatory: James Webb Space Telescope (JWST) [24]
4. **Optical** observatory: Hubble Space Telescope [25]
5. **Ultra-violet** observatory: Galaxy Evolution Explorer (GALEX) [26]
6. **X-ray** observatory: Chandra X-ray Observatory [27]
7. **Gamma-ray** observatory: Fermi Gamma-ray Space Telescope (Fermi) [28]

EM radiation suffers some effects when propagating towards Earth. It is often absorbed by interstellar gas and dust located along the line of sight between the source and observer. On top of that, high-energy gamma-ray photons suffer from additional interactions with low-energy photons, like the ones from the Cosmic Microwave Background (CMB). As such, some sources can become completely opaque.

The discovery of cosmic rays by Hess opened up a new possibility to probe the universe apart from EM observations. These cosmic rays can reach ultra-high energies, $\sim 10^{20}$ eV, and have to be produced by the most

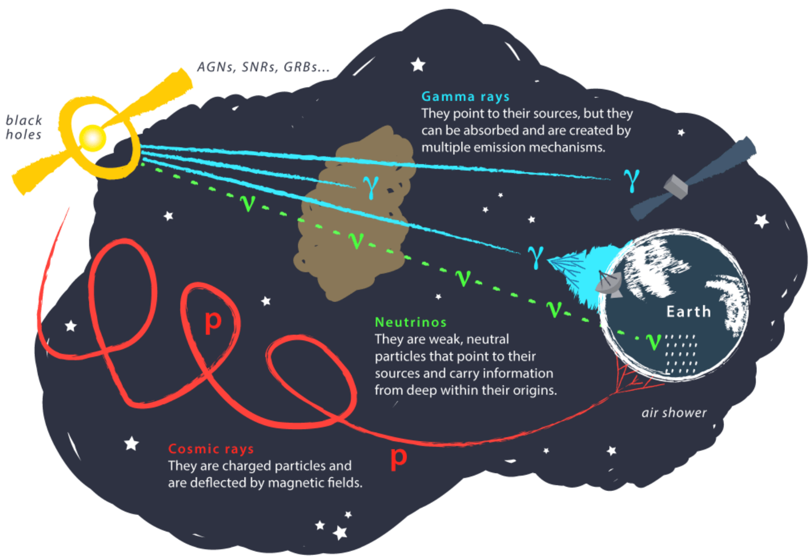

Figure 2.2: An artist visualisation of the propagation of multiple cosmic messengers originating from the same source. The CRs (p) are deflected by magnetic fields on their way to Earth. Photons (γ) and neutrinos (ν) do not suffer from this as they are chargeless. Photons experience attenuation by passing through interstellar clouds or interacting with the CMB. Neutrinos travel unharmed in a straight path from the source to the observer. Figure from [29].

energetic events in the universe. Since cosmic rays are charged particles, their trajectory is deflected by the numerous magnetic fields they come across when propagating towards Earth. As such, they do not trace back to their source. Neutrinos do not suffer from the difficulties photons and cosmic rays experience: they have no charge so they are not deflected by magnetic fields and interact rarely with their surroundings allowing them to fly through any interstellar cloud unharmed. Unfortunately, the fact that neutrinos are weakly interacting makes them difficult to detect on Earth and large-scale observatories need to be built to observe them. Still, neutrinos are ideal particles for astronomical observations that have led to the development of neutrino astronomy which forms one of the major branches of multi-messenger astronomy. Neutrino astronomy will be the topic of Chapter 3. In this work, the attention is directed towards the high-energy universe and as such, the detection of high-energy CRs, gamma rays, and high-energy neutrinos of which the latter is the main focus. Figure 2.2 shows an artist's visualisation of these high-energy cosmic messengers on their way to Earth.

In the following sections, each of these three cosmic messengers is discussed in more detail. As is clear from the above, each messenger has its upsides and downsides. This has led to the development of multi-messenger astronomy combining all the research from the three cosmic messengers to build a global understanding of the high-energy universe. Figure 2.3 illustrates the importance of multi-messenger astronomy. This figure shows the flux for each of the cosmic messengers as a function of their energy. It becomes clear that the shape of the flux spectra is comparable for each cosmic messenger but shifted towards different energy ranges. Neutrinos originate from, for example, charged pion decays produced in CR interactions, and these CR interactions can also produce neutral pions, which in turn decay into gammas. This is explained in more detail in Section 2.4 and 2.5 As such, there should be some relation between the three cosmic messengers due to their common origin leading similar patterns in the observed spectra in Figure 2.3.

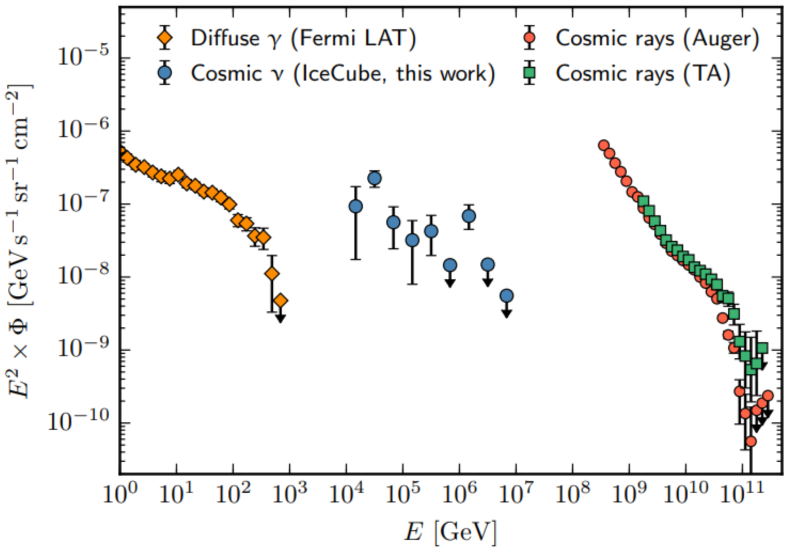

Figure 2.3: The flux measurements for γ-rays, neutrinos and CRs respectively observed by Fermi-LAT [28], IceCube [7], Pierre Auger [30] and the Telescope Array (TA) [31]. Figure from [32].

2.3 Cosmic rays

In this section CRs and how they can be accelerated towards high energies using different acceleration mechanisms are discussed. Sections 2.4 and 2.5 will cover gamma rays and neutrinos and how they can be produced by these high-energy CRs.

2.3.1 Flux spectrum

The flux spectrum of CRs has been measured, see Figure 2.4a, by multiple different experiments. The discontinuities in this figure are of physical nature and can be explained in a rather elegant way when considering what is called the Hillas criterion [4]. The Hillas criterion estimates the upper bound on the energy of a particle accelerated by a certain mechanism. Examples of such acceleration sites are the shock waves in a supernova remnant (SNR), AGN, GRBs, pulsars and more. The Hillas criterion determines the maximal energy by assuming that the charged particle needs to be confined in the physical size of the accelerator to be accelerated by it. This corresponds with assuming that the charge gyrates with a radius found by equating the centripetal and Lorentz force. This yields the formula for the maximal energy [4],

$$E_{max} = qBR \, , \tag{2.1}$$

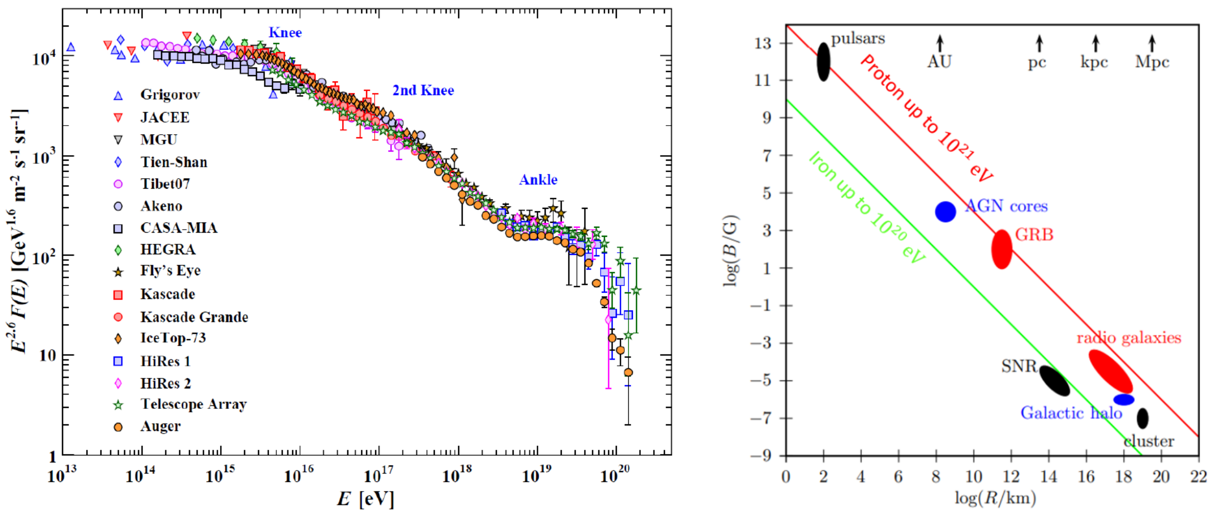

(a) (b)

Figure 2.4: (a) The cosmic ray spectrum. Note that it is rescaled to make the knees and ankle more clear. (b) Hillas relation for different acceleration sites as a function of their characteristic size R and magnetic field strength B. Figures from [4] and [33].

where q is the charge of the particle, B the average magnetic field strength and R the size of the accelerator. Note that in the derivation of this formula, the momentum of the particle corresponds with its energy as the rest energy can be safely ignored at these high energies [4]. Hence, Equation (2.1) represents to which maximal energy a certain acceleration site with size R can accelerate a particle before it escapes the system and stops gaining energy. In Figure 2.4b a graphical representation of the Hillas criterion is given for different accelerators and cosmic rays.

Using the Hillias criterion, an explanation for the specific form of the CR spectrum in Figure 2.4a can be given. The first discontinuity called, the first knee, is situated at $E = 10^{15}$ eV. Exceeding this energy level, protons can no longer be accelerated by SNRs in the Milky Way, leading to a sudden drop in the observed flux. From Equation (2.1), it is clear that heavier nuclei, with larger q, can be accelerated up to larger E by the same accelerator. This explains the origin of the second knee: at larger energies even the heavier nuclei are not accelerated anymore by SNRs. The region between the second knee and the ankle is believed to be the transition region from a galactic to an extragalactic source of CRs. At energies exceeding the ankle, $E \approx 10^{19}$ eV, all sources are believed to be extragalactic.

2.3.2 Particle acceleration mechanisms

There exists more than one way to accelerate CRs to high energies. Two well-known acceleration mechanisms are listed below but it should be noted that more mechanisms, like for example magnetic reconnection [34], do exist.

1. **Diffusive shock acceleration** [35]: It was proposed by Enrico Fermi that shock waves in a plasma are the ideal site to accelerate charged particles. As the shock wave moves through the plasma, it sweeps up particles. These charged particles will move back and forth across the shock front several times due to the magnetic field scattering them. Each time a particle crosses the shock front, it gains an energy proportional to $\frac{\Delta E}{E} \propto \frac{V_s}{c}$, where V_s is the speed of the shock front. This mechanism is also known as first order Fermi acceleration.

2. **Stochastic acceleration** [35]: Fermi also proposed that charged particles interacting with interstellar clouds could be accelerated towards high energies. These clouds can be seen as irregularities in the galactic magnetic field and act as a mirror deflecting the particle. If the magnetic mirror is moving

towards the particle, it will transfer energy. If the mirror moves away from it, the particle will lose energy. The key to acceleration is that the amount of head-on interactions dominates. The particle gains energy every time it scatters off the mirror following the relation $\frac{\Delta E}{E} \propto \left(\frac{V}{c}\right)^2$, where V is the speed of the cloud. Due to the quadratic dependency, this mechanism is often called second order Fermi acceleration.

First order Fermi acceleration is more efficient than the second order due to the additional V/c factor for second order Fermi acceleration [35].

2.3.3 Particle cascades and the Heitler model

When a CR hits an atom, it will create new secondary particles. These secondary particles can subsequently interact with the medium and produce other particles. This process can repeat itself multiple times leading to a cascade-like effect. Hence, CRs can produce so-called particle cascades. When the target atom is specifically an atom in the Earth's atmosphere, the particle cascade is called an air shower. In this section, the development of an EM particle cascade through the Heitler model [36] is discussed. An EM particle cascade only considers photons, electrons and positrons. A realistic cascade has also hadronic content, predominantly in the form of neutral and charged pions. For simplicity reasons, only the Heitler model is considered but a hadronic extension and a good overview of this model can be found in [36].

The EM cascade described by Heitler starts with a single high-energy photon that splits up into an e^-e^+-pair. This pair of electrons will subsequently emit a photon via the bremsstrahlung mechanism described in Section 2.4.1. The repetition of the photon splitting up into an e^-e^+-pair and the emission of bremsstrahlung creates the particle cascade, as shown in Figure 2.5. In the Heitler model it is assumed that each particle splits up when a fixed distance is travelled called the splitting length, $d = \lambda_r \ln(2)$ where λ_r is the radiation length[4]. On top of that, each time a particle splits, it distributes its energy equally over the two daughter particles. Hence, the energy of each particle at a splitting level n is

$$E_n = \frac{E_{n-1}}{2} = \frac{E_p}{2^n} , \tag{2.2}$$

where E_p is the energy of the original particle or primary inducing the cascade. The primary has finite energy, so it becomes clear from Equation (2.2) that the energy of particles at large splitting levels decreases drastically in comparison to the primary. At some point, the energy of the particles will not be sufficiently high enough to keep on supporting the subsequent splittings and the cascade stops developing. This energy is called the critical energy E_c, and indicates at what point pair production and bremsstrahlung can no longer be supported and energy losses start to dominate [36].

From these assumptions, both the maximum number of particles N_{max} and the size of the cascade n_c are reached when $E_n = E_c$. Hence, it can be found from the fact that $N = 2^n$ and Equation (2.2) that [36]

$$\begin{cases} n_c = \frac{\ln E_p/E_c}{\ln 2} \\ N_{max} = 2^{n_c} \end{cases} \tag{2.3}$$

Qualitatively the relations in Equation (2.3) imply that the maximum number of particles inside the cascade scales linearly with the primary energy and the location of the maximum, or depth, scales logarithmically with the primary energy. These are the two main features of real particle cascades the Heitler model can reproduce [36].

[4]The radiation length of a certain material indicates how many energy a particle loses when traversing it. It is defined as the distance the particle has to travel to lose e^{-1} of its original energy via bremsstrahlung.

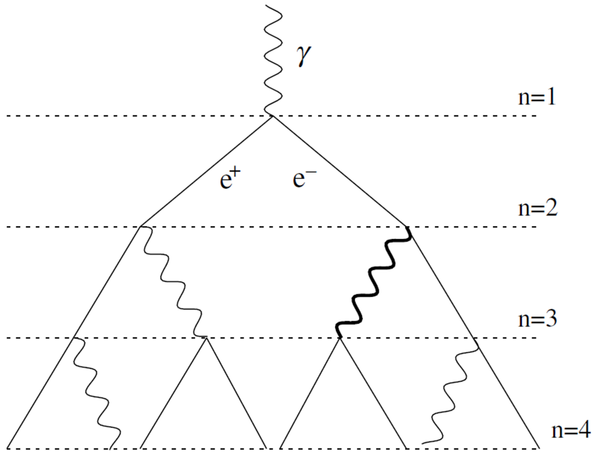

Figure 2.5: A schematic overview of the Heitler model describing an EM particle cascade up to the fourth splitting level. Figure from [36].

2.4 Gamma rays

Gamma rays are also an important high-energy cosmic messenger. They are produced by numerous different sources that can be of galactic or extragalactic origin. In the Milky Way, bright gamma-ray sources are for example SNRs, pulsars and X-ray binaries [37]. Extragalactic sources are for example AGN, GRBs and starburst galaxies [37]. The combination of all of these sources makes up the observed gamma spectrum in Figure 2.3. It should be noted that the gamma rays observed on Earth have different energies than originally emitted by the source. As already mentioned, interactions of the gamma ray with surrounding matter and background photons decrease the gamma ray's energy. On top of that, both Doppler shifts and cosmological redshifts cause the observed energy to change.

2.4.1 Production

Gamma rays are photons that carry an energy of more than 100 keV and are therefore the most energetic photons in nature. In order to produce these energetic photons, charged leptons or hadrons must be accelerated up to high energies. There exist multiple mechanisms for their production and they are generally divided into two main classes: leptonic and hadronic.

When leptons, such as electrons, are accelerated using one of the mechanisms described in Section 2.3.2, they can emit electromagnetic radiation in the form of gamma rays through [35, 37]:

1. **Synchrotron radiation**: This type of emission occurs when a relativistic charged particle gyrates in the presence of a magnetic field. Due to the relativistic speed of the particle, the emission will be strongly beamed into a cone-like shape with an opening angle of Γ^{-1}, where Γ is the Lorentz factor. On top of that, the dominant frequency peak will be up-shifted towards higher frequencies leading to gamma ray emission. The power of synchrotron radiation scales as $\propto m^{-4}$, with m the mass of the particle. Hence this mechanism is more efficient for low-mass leptons, like electrons, than heavier hadrons, like protons.

2. **Bremsstrahlung**: When a relativistic charged particle passes close to an atomic nucleus, its trajectory can be deflected due to EM interactions. This results in the particle accelerating and emitting forward-beamed electromagnetic radiation.

3. **Inverse Compton scattering**: This process involves relativistic charged particles that up-scatter low-energy photons into gamma rays. It is the exact opposite of Compton scattering [38], and is given by the reaction,
$$e^- + \gamma_{low} \rightarrow e^- + \gamma_{high} \, . \tag{2.4}$$
The low-energy photons γ_{low} can be CMB, infrared, optic or X-ray photons.

The main hadronic process responsible for the emission of high-energy gamma rays is the decay of neutral pions (π^0). Pions are produced when accelerated hadrons, like protons, interact with each other or a photon. CR protons are thus the perfect ingredient to produce pions. Charged and neutral pions are produced in equal amounts in these reactions. It is the production and subsequent decay of a neutral pion that can lead to the emission of two high-energy photons,

$$p + p(\gamma) \rightarrow \pi^0 \rightarrow 2\gamma \, . \tag{2.5}$$

2.5 Neutrinos

Neutrinos, and more specifically high-energy neutrinos, are the main topic of this writing. As such, a more detailed overview is given than for the CRs and gamma rays. Since neutrinos are chargeless and only interact via weak interactions, they are probably one of the least understood fundamental particles in the Standard Model. This section starts with presenting the history of neutrinos and their remaining open questions followed by a discussion on neutrino sources and their high-energy production.

2.5.1 History

The first proposal that neutrinos exist, dates back to the discovery of radioactivity in the early twentieth century [3, 39]. From beta decay experiments it became clear that the energy of the emitted electron, the β particle, forms a continuous spectrum as opposed to alpha and gamma decay where the emitted particle always has a single fixed energy value. This was a puzzling result as it would violate the conservation of energy. It was Wolfgang Pauli who suggested in 1930 that there was an additional particle emitted in the beta decay reaction that was not observed in the experiments. Two years later, in 1932, Enrico Fermi wrote down his well-known theory of β-decay [40] explaining how an electron together with Pauli's unseen particle can be emitted by a nucleus and named this particle a *neutrino*. As the emission of this neutrino is always accompanied by an electron, it is called an electron neutrino (ν_e). It was only in 1954 that the electron neutrino was proven to exist experimentally by Cowan and Reines [2]. When a radioactive nucleus decays via β-decay, it emits an electron and an antineutrino. This antineutrino can subsequently interact with a proton via the interaction,

$$\bar{\nu}_e + p \rightarrow n + e^+ \, , \tag{2.6}$$

also known as inverse β^+-decay. Cowan and Reines put a large vessel filled with hydrogen right in front of a nuclear reactor. This allowed them to have a strong source of antineutrinos that fly through lots of protons. They were able to detect the positron and neutron created in the interaction described in Equation (2.6) and such proved the existence of antineutrinos predicted by Pauli and Fermi. It earned them the Nobel Prize in 1995 [3].

Neutrino flavours: The electron has two heavier brothers, called the muon (μ) and tauon (τ) that each have their neutrino counterpart called respectively the muon neutrino (ν_μ) and tauon neutrino (ν_τ). These two neutrino flavours were discovered many years after Cowan and Reines observed the ν_e. In 1964, the ν_μ was discovered by the Brookhaven experiment from the decay of pions, kaons and muons produced in accelerator experiments [39]. The discovery of the ν_τ took many more years and was for the first time observed by the DONUT experiment at Fermilab in 2000 [39]. These discoveries helped in solving the solar neutrino problem.

Neutrino oscillations: For a long time it was believed that neutrinos were massless particles. If the neutrinos have masses that are slightly different from each other, a certain flavour neutrino could oscillate into another flavour when propagating through vacuum or matter. When considering only two neutrino flavours, it can be proven that the survival probability of an electron-neutrino is given by [1],

$$P(\nu_e \rightarrow \nu_e) = 1 - \sin^2(2\theta) \sin^2\left(\frac{\Delta m^2 L}{4E_\nu}\right) , \tag{2.7}$$

where θ is called the mixing angle, $\Delta m^2 = m_1^2 - m_2^2$ with m_i the mass of the i-th mass eigenstate, E_ν is the energy of the neutrino and L is the distance along the neutrino's direction of flight when it interacts. Hence, from Equation (2.7), it is clear that neutrino oscillations and masses are two closely related topics. If neutrino oscillations are observed in nature, only the mass-squared difference between the flavours can be deduced. Nonetheless, observing these oscillations would be compelling evidence of neutrino masses.

One of the longest-lasting mysteries in neutrino physics was the solar neutrino problem, solved in 2002 by observations from the Sudbury Neutrino Observatory (SNO) experiment. In 1920, it was proposed that the energy generated by the Sun originates from nuclear fusion processes [3]. These processes would produce a large amount of neutrinos and make the Sun a strong source of neutrino emission. The Brookhaven experiment, more commonly called the Homestake experiment, used the inverse beta decay of chlorine

$$\nu_e + {}^{37}\mathrm{Cl} \rightarrow e^- + {}^{37}\,\mathrm{Ar} \tag{2.8}$$

to detect the neutrinos from the Sun. Solar neutrinos were detected, but only one-third of what was predicted by the standard solar model (SSM) [3]. This was a surprising discovery and took almost 40 years to solve. The SNO experiment was able to solve the solar neutrino problem in 2002 by using heavy water[5] instead of chlorine [3]. The deuterium atoms (D) in the heavy water allowed for two types of interactions, the so-called charged current (CC) and neutral current (NC) interactions:

$$\begin{aligned} \nu_e + D &\rightarrow p + p + e^- \ (\mathrm{CC}) \\ \nu + D &\rightarrow p + n + \nu \ (\mathrm{NC}) \ . \end{aligned} \tag{2.9}$$

Because of the additional NC interaction in the SNO experiment, it became also sensitive to other flavours of neutrinos. As such, they could measure the ν_e flux and total neutrino flux at the same time. They concluded that the total neutrino flux is consistent with what is predicted by the SSM and that only one-third of the total flux consists of ν_e, consistent with what Homestake observed 40 years prior. This observation offered conclusive proof that neutrinos oscillate during their journey from the Sun to Earth. Apart from SNO, other experiments like SuperKamiokande also observed neutrino oscillations [3]. Hence, all these experimental results were of fundamental importance in the discovery of neutrino masses.

2.5.2 Open questions

Since the discovery of neutrino oscillations at the start of the 21$^{\text{st}}$ century, neutrino physics has gained much more attention. As such, long-lasting open questions about the nature of neutrinos are under full investigation by multiple research groups.

Dirac or Majorana nature: The standard model predicts that neutrinos are Dirac particles instead of Majorana particles. A Majorana particle is its own antiparticle and was first theoretically proposed by Ettore Majorana in 1937. If neutrinos are massless particles, a Majorana description becomes equivalent to a Dirac description [41]. As of today, the question on their nature is still unanswered. One of the most promising ways to find out the answer to this question is via the nuclear decay process called neutrinoless double beta decay ($0\nu\beta\beta$) [42].

Absolute neutrino mass: Neutrino oscillation experiments can only deliver measurements of the mass-squared differences between the neutrinos. Hence, the absolute mass of neutrinos is still unknown. From cosmological considerations it is found that the $\sum m_\nu < 0.2$ eV [43]. This value is model-dependent as it is based on a cosmological model combined with observations of structure formation in the early universe. $0\nu\beta\beta$ can also be used to find an upper limit on the absolute mass of neutrinos [43], but just like the cosmological methods, it is model-dependent as $0\nu\beta\beta$ requires the neutrinos to be Majorana particles. A third model-independent method exists for determining the absolute mass of neutrinos. This is done via single beta decay experiments of tritium (^{3}H) [43]. The energy of the emitted β particle from the decay of ^{3}H follows a spectrum. By looking at the tail of this distribution, an upper limit on the neutrino mass can be determined. KATRIN [44] is an example of such a tritium experiment. They were able to set a world-leading limit on neutrino masses for tritium-based experiments of $m_\nu < 0.8$ eV with a 90% confidence level [44].

[5] Heavy water is H_2O where regular hydrogen is replaced by deuterium, hydrogen with one neutron in the nucleus [3].

2.5.3 High-energy neutrino production

The production of high-energy neutrinos is closely related to the hadronic origin of gamma rays, discussed in Section 2.4.1. When a CR interacts with its surroundings, it can lead to the production of high-energy neutrinos through the decay of charged pions ($\pi^{\pm}$). To simplify the discussion, only cosmic ray protons are considered. This is a good approximation for CR primary energies below 10^{17} eV. As it turns out, recent results show that above this energy threshold, the mass composition of CRs favours heavier species [45]. A second assumption will be made as well. When a CR interacts with its surroundings, it can either be with matter or with a radiation field. It is a good assumption to consider most astrophysical matter consists of hydrogen, and thus protons. Hence, two interactions will be considered: pp-interactions and $p\gamma$-interactions. Both lead to the production of new particles such as pions, kaons, protons and neutrons. In the case of neutrino production, pions are the main contributor and will be considered solely [4, 46]. As these pion production mechanisms require hadronic models, only an overview is sketched without going into the detail of the physical interactions inducing them.

1. ***pp*-interactions**: When a CR proton with high enough energy, in a fixed-target scenario this corresponds with $E_p \geq 1.22$ GeV [46], hits matter in the interstellar medium (ISM), it can produce pions according to,

$$p + p \rightarrow \begin{cases} p + p + \pi^0 & \text{(fraction 2/3)} \\ p + n + \pi^+ & \text{(fraction 1/3)}\ , \end{cases} \tag{2.10}$$

   where the fractions are determined from an isospin symmetry argument[6] [46]. It should be noted that CR protons with energies below the threshold energy of 1.22 GeV are considered to be low-energy CRs. Hence, they are of no interest in this work and the condition is assumed to be satisfied. Even more so, the high-energy CRs carry enough energy to produce more than one pion, both neutral and charged, in a single inelastic pp-collision.

2. ***pγ*-interactions**: CRs can also interact with radiation fields and produce pions. This is mainly done through Δ^+-resonance at the threshold energy of the process [4]. The dominant channels in the pion production are therefore,

$$p + \gamma \rightarrow \Delta^+ \rightarrow \begin{cases} p + \pi^0 & \text{(fraction 2/3)} \\ n + \pi^+ & \text{(fraction 1/3)}\ , \end{cases} \tag{2.11}$$

   where once again isospin symmetry can be used to find the fractional contributions of the two channels. If the CR proton has energy significantly above the threshold energy, multiple pions can be produced from a single $p\gamma$-interaction.

Now that it is established how pions can be produced through both pp-interactions and $p\gamma$-interactions, the production of the neutrinos themselves can be discussed. As neutrinos are weakly interacting particles, only the weak decay of charged pions produced in pp-interactions and $p\gamma$-interactions can lead to neutrino production:

$$\begin{cases} \pi^+ & \rightarrow \mu^+ + \nu_\mu \rightarrow e^+ + \nu_e + \bar{\nu}_\mu + \nu_\mu \\ \pi^- & \rightarrow \mu^- + \nu_\mu \rightarrow e^- + \bar{\nu}_e + \nu_\mu + \bar{\nu}_\mu\ . \end{cases} \tag{2.12}$$

The neutral pions will decay into photons as discussed in Section 2.4.1.

From the discussion above it becomes clear that the neutrino and gamma-ray energy are strongly correlated. As they have a common origin through the interaction of CRs, the energies of the three cosmic messengers are related by $E_\nu \approx E_\gamma/2 \approx E_p/20$ [47], where E_p is once again the energy of the original CR proton.

[6] Isospin is a flavour symmetry in the quark sector and is conserved during strong interactions. As the u and d quark have very similar masses, the isospin symmetry $u \leftrightarrow d$ and $\bar{u} \leftrightarrow -\bar{d}$ is almost an exact symmetry in nature. The neutral pion forms a $|\pi^0\rangle = \frac{1}{\sqrt{2}}(u\bar{u} - d\bar{d})$ state that is invariant under the above transformation. The charged pions transform into each other when performing an isospin transformation: $|\pi^+\rangle = u\bar{d}$ and $|\pi^-\rangle = \bar{u}d$. As such the neutral pion production gains an extra factor of two.

2.5.4 Neutrino populations

To end the introduction on neutrinos, an overview is given of the different neutrino populations. This classification is mainly based on the production mechanism and the subsequent accessible energy range of the neutrino. A good summary can be found in [48], and the predicted neutrino flux as a function of energy for for each population is shown in Figure 2.6.

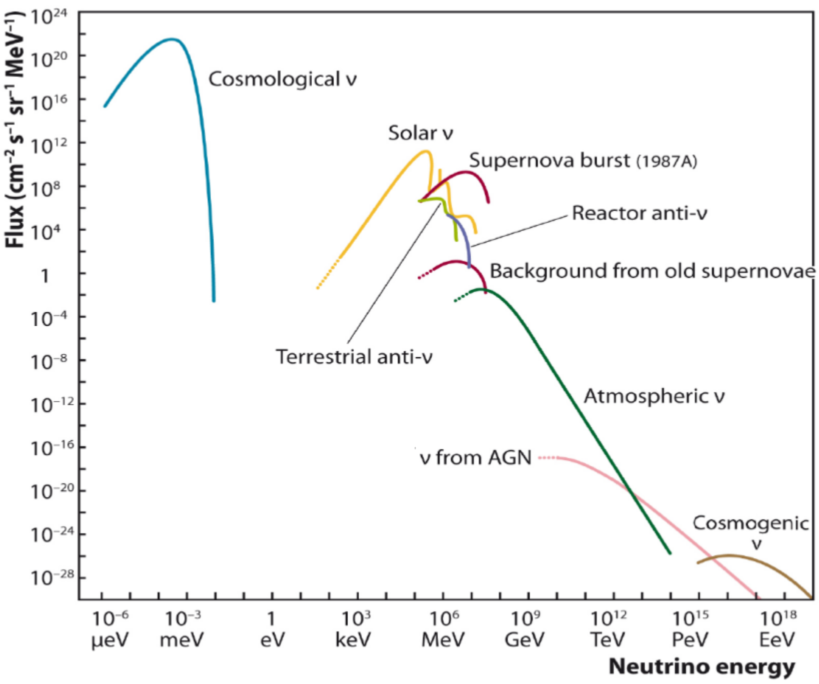

Figure 2.6: An overview of the different neutrino populations and their flux spectra. Figure From [48].

Cosmogenic neutrinos: The most energetic neutrinos arise from the $p\gamma$-interaction between an ultra-high-energy cosmic ray (UHECR), $E_p \geq 10^{18}$ eV, and the CMB. Since the CMB photons are low-energetic, the threshold energy for the $p\gamma$-reaction to occur is high and must be at least $E_p = 4 \times 10^{19}$ eV. Consequently, only UHECRs can produce neutrinos in this way. This is also known as the Greisen–Zatsepin–Kuzmin (GZK) limit [49, 50, 51] and is believed to cause the sudden drop in the CR flux in Figure 2.4a at the corresponding energy. To this day, these so-called cosmogenic neutrinos have not yet been observed, but this is one of the goals of radio neutrino observatories like RNO-G [8] and RET-N [10].

Astrophysical neutrinos: Some astrophysical objects possess the ability to accelerate hadrons, such as protons, towards high energies using the mechanisms described in Section 2.3.2. Hence, these astrophysical objects, for example, AGN, become sources of CRs. When this source is embedded in a region of dense material or radiation, the CRs can interact via the pp-interaction and $p\gamma$-interaction and produce neutrinos. These neutrinos are called astrophysical neutrinos. In Figure 2.6 the flux spectrum of astrophysical neutrinos expected to be produced by AGN is shown. It should be noted that other cosmic accelerators, like for example pulsars, could potentially produce astrophysical neutrinos.

Atmospheric neutrinos: Some CRs can escape the accelerator site without interacting. When these CRs reach the Earth, they will interact with the nuclei in the atmosphere and produce a cosmic ray air shower. This air shower is the result of consecutive interactions by the secondary particles creating new particles over and over again, leading to a cascade-like effect. Typically, lots of pions are produced in these showers that will decay into neutrinos as given by Equation (2.12). These neutrinos are called atmospheric neutrinos and form a background for experiments searching for astrophysical neutrinos.

As can be seen from Figure 2.6, there exist numerous other populations of neutrinos. These low-energy neutrinos have typically energies below 1 MeV and are therefore not of main interest in this work. Still, to be complete the sources are briefly discussed. As already mentioned in Section 2.5.1, the neutrino was discovered from experimental research regarding radioactive decay. The neutrinos from these processes are called reactor neutrinos. In Section 2.5.1 it was also mentioned that the Sun forms a bright source of low-energy neutrinos. The observation of these neutrinos was crucial in the discovery of neutrino oscillations and neutrino masses. As already mentioned, the observation of neutrinos from SN 1987A was important in the revival of astroparticle physics. When a massive star is at the end of its life, the core will collapse. During the collapsar the entire core is depleted from the degenerate electrons through electron captures by protons producing lots of neutrons and neutrinos. These neutrinos escape from the core, cooling it, and power the explosion of the outer layers of the star [21]. This makes supernova explosions a bright source of low-energy neutrinos. The last source of neutrinos is the so-called cosmological neutrinos. These neutrinos were produced shortly after the Big Bang and should form an isotropic background of neutrinos similar to the CMB for photons [52].

Chapter 3

Neutrino astronomy

This chapter discusses how high-energy neutrinos can be observed in experimental setups through the particle cascade they induce upon interaction with their surrounding. Both optical and radio detectors can be built to observe these secondary particles. In Section 3.1, optical detection through the emission of Cherenkov radiation is discussed together with the IceCube Neutrino Observatory. In Section 3.2, the radio detection of neutrinos is discussed using Askaryan radiation together with the Radio Neutrino Observatory in Greenland. In Section 3.3, a novel detection technique based on radar is discussed together with the Radar Echo Telescope experiment. Radar is the main focus of this thesis as an investigation of the signal properties from this detection technique is performed using a simulation software called MARES.

3.1 Optical Cherenkov emission

When a neutrino induces a particle cascade in a dense medium like for example ice, the (charged) secondary particles will move on average with speeds close to the speed of light in vacuum. The light itself only propagates with speed $v \sim c/n$, where n is the refractive index of ice. A special radiation mechanism arises called Cherenkov radiation. The optical part of this radiation field is observed by detectors such as IceCube and allows for reconstructing the neutrino's original energy and direction.

3.1.1 Cherenkov radiation

When a charged particle is moving at relativistic speeds through a dielectric, exceeding the local speed of light, EM waves with a specific continuous spectrum and geometrical shape will be emitted. This effect is called Cherenkov radiation and is the reason why underwater nuclear reactors show a typical blue glow. This section is dedicated to give a brief overview of the mechanism behind the radiation [6, 53, 54].

In the early days of radioactive studies, it was believed that the bluish light emitted by a material that was exposed to radioactive radiation was a consequence of ionization. Rather quickly, it was discovered that the colour of the light was material independent and that the emission formed a continuous spectrum, as opposed to the typical discrete spectrum expected from ionization effects [53]. On top of that, Pavel Alekseyevich Cherenkov discovered that the light has unique polarisation and directional properties [53]. These four observations made it indisputable that the light was not a form of luminescence but something different.

When a charged particle is moving through a dielectric medium, it will polarise the electrons of the material's atoms due to its Coulomb field. This creates an entire track of polarised electrons. It is important to note that the electrons themselves are not excited or removed from the atom, they are slightly displaced creating small dipoles [53], as shown in Figure 3.1. These dipoles will emit spherical wavelets when they relax and cease to exist. Depending on the speed of the charged particle traversing the material, the wavelets originating from each of these dipoles will interact constructively or destructively. The crucial condition for having constructive interference is the fact that the charged particle must move at a speed larger than the speed of light in the material, the latter is also referred to as the phase velocity [53]. In this case the cylindrical symmetry around the particle's track is broken and a net dipole field is created, as shown in Figure

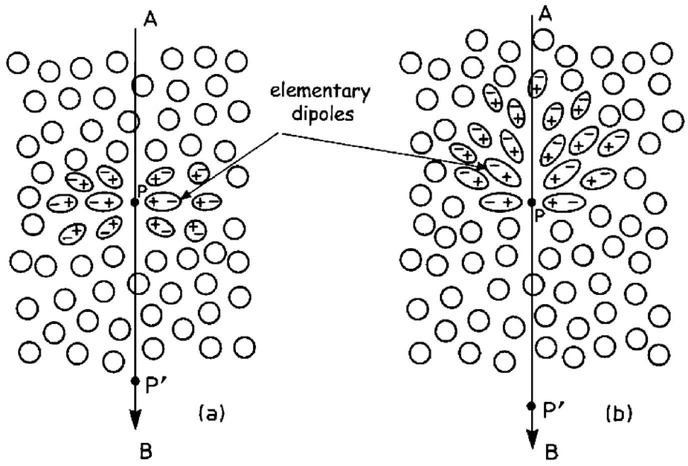

Figure 3.1: An illustration of the polarising effect of a charged particle moving through a dielectric material. The charged particle moves respectively with a velocity smaller (a) and bigger (b) than the local speed of light. Figure from [54].

3.1. The resulting wavelets will interact constructively and a cone-like shape is created for the wavefront as is illustrated in Figure 3.2. As can be seen from this figure, the Cherenkov cone is the electromagnetic equivalent of a sonic blast created by for example a jet crossing the sound barrier.

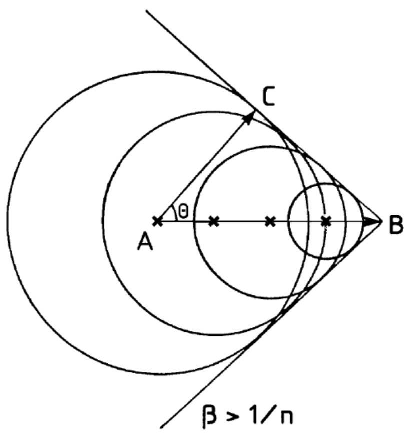

Figure 3.2: An illustration of the Cherenkov cone when a charged particle is moving at a speed v larger than the phase velocity of the material c/n. Figure from [54].

There are two ways of determining the opening angle θ_c of the Cherenkov cone. The first approach considers simple geometrical arguments, while the second derivation uses conservation of energy and a quantum description of light as photons. Assume a charged particle is moving from point A to B in Figure 3.2, with a speed exceeding the phase velocity of the material. If the particle moves along the AB line, it polarises the electrons with the rise of spherical wavelets. This is denoted by the crosses in the figure. The wavelets will constructively interfere and form a straight wavefront corresponding with the BC line. If the charged particle travelled the distance $AB = v\Delta t$ in a time Δt, then the distance travelled by the light in that same amount of time is $AC = (c/n)\Delta t$, where c is the speed of light in vacuum and n the refractive index of the material. Using simple geometric identities it is found from Figure 3.2 and the values above that [53]

$$\cos\theta_c = \frac{1}{\beta n}\,, \tag{3.1}$$

where $\beta = v/c$. In [55], the derivation of Equation (3.1) is done starting from the conservation of momentum and the quantum description of light using photons.

Not only has the Cherenkov radiation a specific directionality as described above, it has a unique polarisation as well. The electric field lays in the plane defined by the particle direction and the propagation direction of the wavefront. The magnetic field is always tangent to the surface of the cone [53]. It was also proven that the frequency spectrum of Cherenkov radiation is given by the Frank-Tamm equation [53],

$$\frac{d^2E}{dx d\omega} = \frac{q^2}{4\pi}\mu(\omega)\omega\left(1 - \frac{c^2}{v^2 n^2(\omega)}\right) . \tag{3.2}$$

This equation describes the amount of energy E that is emitted per unit length travelled x and per frequency ω. Both the permeability μ and refractive index n change depending on the frequency of the emitted light. In this equation, q and v are respectively the particle's electric charge and velocity and c is the speed of light in vacuum. It can be shown that around the visible part of the electromagnetic spectrum, Equation (3.2) is proportional to the frequency, hence resulting in the characteristic observed blue light in underwater nuclear reactors [53].

3.1.2 Geometrical Cherenkov effect

To end the discussion about Cherenkov radiation it is noted that the name Cherenkov radiation or effect is often used to refer to different things, depending on the field of research. In radar physics and cosmic ray radio detection, talking about Cherenkov radiation is often meant to point to the geometrical effect and not the actual mechanism itself. In other words, there will exist a viewing angle θ between the source of EM radiation and the observer such that all signals emitted by the source arrive at the same time at the observer. It will turn out that this angle is exactly given by the Cherenkov cone angle in Equation (3.1). When in this thesis the Cherenkov effect is mentioned, it only refers to the geometrical effect.

The proof of the above statement is based on the schematic setup shown in Figure 3.3. The source starts at the blue dot and will keep emitting light while propagating along the x-axis with a speed v. The observer is indicated by the red cross. An important concept in physics is that of the retarded time t'. Due to the finite

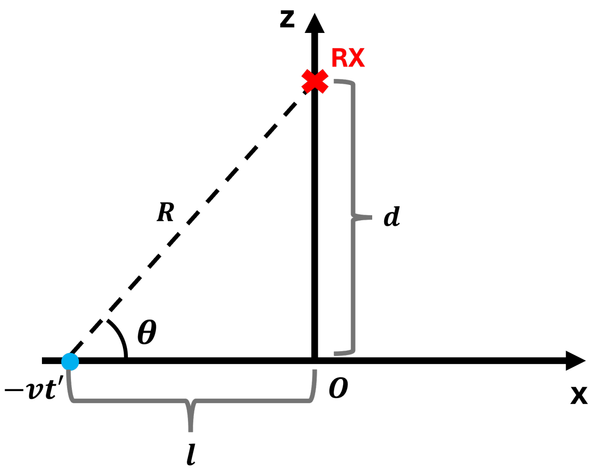

Figure 3.3: A schematic overview of the geometrical Cherenkov effect. In red the observer (RX) is shown and in blue a source emitting light while traveling at a speed v along the x-axis.

speed of light, information needs time to travel to the observer. As such, measuring the electric field at the observer at a time t implies that the electric field created by the source needs to be evaluated at the retarded time. This retarded time is given by

$$t' = t - \frac{R}{c/n} , \tag{3.3}$$

where R is the distance between the source and observer and c/n is the speed of light in the considered medium. From Figure 3.3, it can be found that the distance between the source and observer is

$$R = \sqrt{l^2 + d^2} \ . \tag{3.4}$$

Defining $t = t' = 0$ when the source is at O moving with a speed v along the $+x$-axis, $l = -vt'$. By combining Equation (3.3) and Equation (3.4) it is found that

$$t = t' + \frac{n}{c}\sqrt{(-vt')^2 + d^2} \ . \tag{3.5}$$

The derivative with respect to t' is taken in the above equation to find

$$\begin{aligned} \frac{dt}{dt'} &= 1 + \frac{n}{c}\frac{2v^2t'}{2\sqrt{(-vt')^2 + d^2}} \\ &= 1 - n\frac{v}{c}\frac{(-vt')}{R} \\ &= 1 - n\beta\frac{l}{R} \\ &= 1 - n\beta\cos\theta \ , \end{aligned} \tag{3.6}$$

where $\beta = v/c$ and $\cos\theta = l/R$ as can be seen from Figure 3.3. Equation 3.6 indicates that all signals emitted over a time interval dt' are observed in a time interval dt. Hence, when this derivative becomes zero, it implies that all signals emitted over a finite time interval dt' are observed at the exact same moment, leading to an EM sonic boom. From Equation (3.6) it is found that this happens when

$$\cos\theta = \frac{1}{n\beta} \ , \tag{3.7}$$

which, as predicted, is the same as Equation (3.1). If the source of light is moving near the speed of light, $\beta \approx 1$, the geometrical Cherenkov angle will be non-zero as long as $n > 1$. In this work, ice is the main medium with $n_{ice} = 1.78$, such that the geometrical Cherenkov angle predicted by Equation (3.7) is $\theta_c = 55.82°$.

To end the discussion about the geometrical Cherenkov effect, the relation between t and t' given in Equation (3.5) is explicitly shown in Figure 3.4 for $n = 1.78$ and $\beta \approx 1$. Note that the axis in this figure shows t' vertically and t horizontally and as a consequence, the derivative $dt'/dt \to +\infty$ as observed in the figure. On top of that, it becomes clear that the signals first emitted by the source, do not necessarily arrive earlier at the observer. This is a consequence of the fact that the particle propagates through the ice at a speed near the speed of light in vacuum, which is larger than the local speed of light.

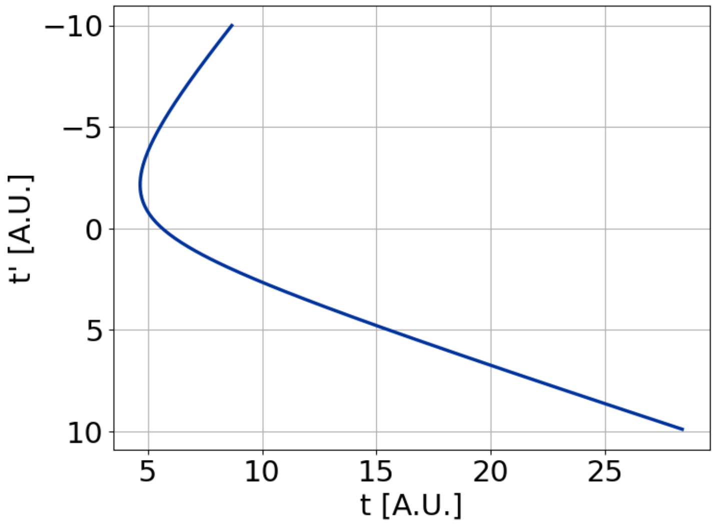

Figure 3.4: A visual representation of the relation between t and t' for $n = 1.78$ in Equation (3.5). Note that the axes are inverted with respect to the equation resulting in the fact that the derivative $dt'/dt \to +\infty$.

3.1.3 IceCube Neutrino Observatory

The IceCube Neutrino Observatory is an optical Cherenkov detector located at the South Pole. Construction ended on December 18, 2010, and approximately took six years [7]. The experiment has multiple goals of which it has already completed its primary objective: the detection of high-energy astrophysical neutrinos and the identification of source candidates as for example the observation of a neutrino excess from the Seyfert galaxy NGC 1068 [56]. Studies regarding dark matter [57] and neutrino oscillations [58] are also conducted using data collected by IceCube.

A schematic drawing of the IceCube Neutrino Observatory can be found in Figure 3.5. It has two main components: the IceCube In-Ice Array and IceTop. The IceCube In-Ice Array is buried 1450 m beneath the surface and reaches down to 2450 m. It consists of 86 vertical strings that are each 1000 m long and equipped with 60 Digital Optical Modules (DOMs), the sensors, spaced 17 m apart along the string [7]. The strings are arranged in a hexagonal shape with a horizontal separation of 125 m. This specific design yields a total of 5160 sensors in a detector volume of 1 km^3 and makes IceCube most sensitive to astrophysical neutrinos in the energy range between 1 TeV and 1 PeV. The central eight strings inside the detector are spaced more compactly with an average horizontal distance of 72 m. The first DOM along these strings is positioned at a depth of 1750 m where the ice has become the clearest, and the first ten DOMs have a spacing of 10 m [7]. The other 50 DOMs are spaced at 7 m distance from each other along the string. This setup allows IceCube to also detect less energetic neutrinos in an energy range between 10 – 100 GeV. This subset of strings in the IceCube In-Ice Array is called DeepCore.

IceTop is a CR air shower detector located right on top of the in-ice array as can be seen from Figure 3.5. It consists out of 81 stations positioned in the same pattern as the in-ice array. Each station has two tanks filled with ice and each tank is equipped with two downwards facing DOMs. Icetop is sensitive to CRs in the PeV to EeV energy range [7].

As neutrinos are weakly interacting particles, IceCube cannot detect them directly. Just like a high-energy CR, a neutrino can interact with an ice molecule and induce a particle cascade of secondary (charged) particles. As these charged particles are moving close to the speed of light in vacuum, they will emit Cherenkov radiation along their trajectory, as discussed in Section 3.1.1. The Cherenkov light from these particles is detected by the DOMs. These DOMs can measure the energy deposition at their location using a high-tech photomultiplier tube (PMT). For details regarding the description of these DOMs is referred to [7]. By determining the time difference between detected signals in different DOMs, the direction of the secondary particles can be reconstructed and with that, the direction of the primary neutrino.

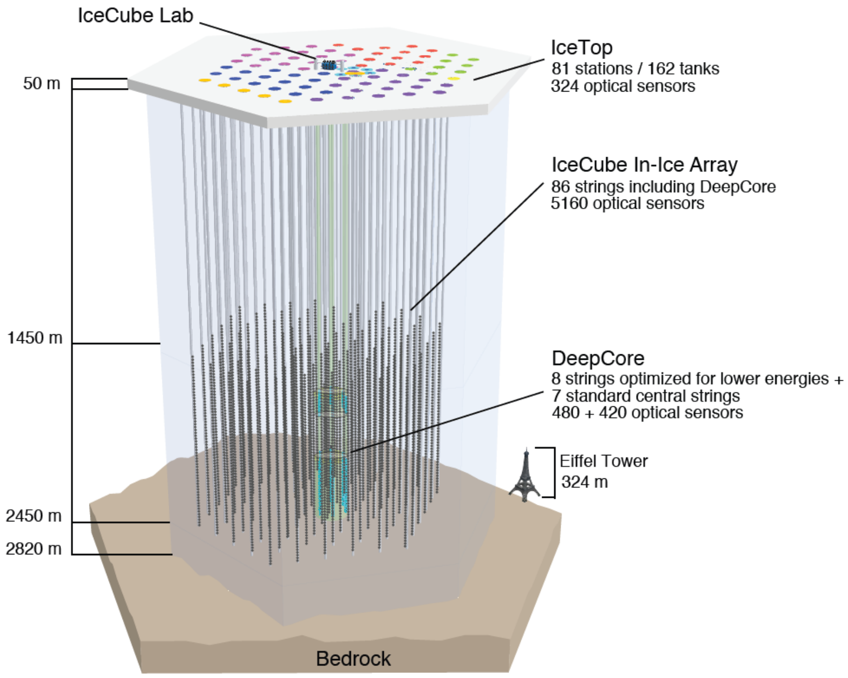

Figure 3.5: A schematic overview of the IceCube Neutrino Observatory. The IceCube Lab is the central operations and data acquisition building of the experiment. The Eifel Tower is drawn to scale beside the experiment to give perspective on the shear size of the detector. Figure from [7].

A high-energy neutrino can interact in two different ways in the ice. Either via a Charged Current (CC) interaction or a Neutral Current interaction (NC). As the name suggest, in a CC interaction a charged $W^{\pm}$-boson is exchanged. Hence, this interaction will produce the corresponding lepton of the neutrino and breaks up the nucleus N and leaves behind debris of hadrons X

$$\nu_l + N \xrightarrow{W} l + X \ . \tag{3.8}$$

In the NC interaction, the neutrino scatters of the nucleus via the exchange of a neutral Z^0-boson. The nucleus will once again break up into a jet from this scattering process

$$\nu_l + N \xrightarrow{Z} \nu_l + X \ . \tag{3.9}$$

The combination of the neutrino flavor and the interaction it underwent, leaves behind a characteristic footprint in the IceCube detector. There exist three main topologies, shown in Figure 3.6. The NC interaction of all three neutrino flavours and the CC interaction of an ν_e produces what is called a (single) cascade topology [59]. A double bang cascade originates from the charged current interaction of a ν_τ producing a tauon that subsequently decays at a different location in the detector. The charged current interaction of ν_μ produces a muon that travels like a clean track through the ice. These track topologies can also be produced by muons originating from atmospheric air showers or from the decay of the tauon from a CC ν_τ interaction.

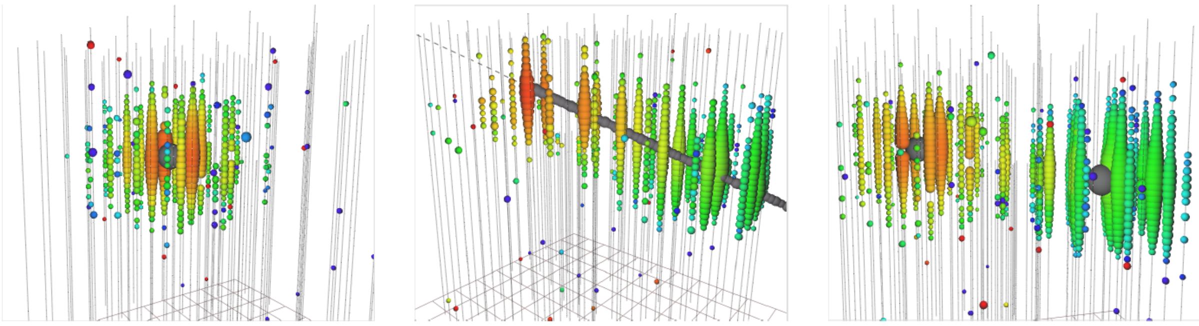

(a) Cascade (b) Track (c) Double bang

Figure 3.6: Simulations of the three main topologies in the IceCube detector. (a) Is the cascade event created by NC interactions of all neutrino flavours and CC interactions of ν_e. (b) The track topology induced by a muon travelling through the detector. This muon can originate from the CC interaction of a ν_μ, the decay of a tauon, or from atmospheric air showers. (c) The double bang topology induced by the CC interaction of a ν_τ and the subsequent decay of the produced tauon in the CC interaction. Figure from [59].

3.2 Askaryan radiation

When a particle cascade traverses through a medium, its high-energy particles can knock out electrons from the atoms and the positrons inside the cascade can annihilate. Hence, an electron excess is created that will emit coherent Cherenkov radiation. This is called the Askaryan radiation effect first proposed by Gurgen Ashotovich Askaryan in 1961 [60]. From Equation (3.2), it is clear that Cherenkov radiation has a continuous spectrum. As such, the emission can be observed in any wavelength. In the case of Askaryan radiation, coherent emission from different electrons forming a macroscopic charge distribution is observed. A necessary condition for coherence is that the physical size of the charge distribution d is smaller than the observed wavelength λ. This can be understood when picturing an EM wave with a certain wavelength being emitted from a macroscopic collection of charges. If $\lambda \gg d$, the phase offset at the observer from waves emanating at different points in the charge distribution becomes negligible. As such, the emission from the different electrons constructively interferes, leading to a clear strong signal at that particular wavelength. The typical size of this charge excess strongly depends on the density of the medium. In air, $d \sim O(10\text{ m})$ while in more dense media like ice, $d \sim O(0.1\text{ m})$ [60]. As such, Askaryan radiation can be detected from both air showers induced by CRs as well as neutrino-induced particle cascades in ice. The latter will be of most interest in this work and an experiment implementing this detection technique for neutrinos is discussed in the next section.

3.2.1 Radio Neutrino Observatory Greenland

The Radio Neutrino Observatory Greenland (RNO-G) is located at the Summit Station in Greenland and is the first radio neutrino observatory oriented towards the Northern sky [8, 61]. Its main scientific goal is to observe high-energy neutrinos above 10 PeV by detecting the Askaryan radio emission from the particle cascade. Construction of the experiment started in 2021 and as of today, already seven stations have been installed and are collecting data. RNO-G builds on previous experiments that have extensively tested and optimised the radio detection technique for example the Radio Ice Cherenkov Experiment (RICE) [62] and the Askaryan Radio Array (ARA) [63].

The RNO-G experiment will consist of 35 stations spread out over a grid with 1.25 km spacing. Each station is identical and completely autonomous. In Figure 3.7 a schematic overview is given of the detector layout as well as the design of the RNO-G stations. The stations consist of three strings that are lowered into the Greenlandic ice to about 100 m depth and equipped with multiple radio antennas at different depths. There are nine Log Periodic Dipole Antennas (LPDA) located at 3 m below the surface. Three of these antennas are pointed upwards to be able to identify or veto signals originating from CRs and human backgrounds [61].

The antenna arrays located at greater depths along the string, either have a horizontal or vertical polarisation. Using both polarisations allows to determine the polarization of the recorded signals and as such the orientation of the Cherenkov cone, which eventually yields the neutrino direction.

When completed, RNO-G will be the largest neutrino observatory in the Northern Hemisphere with a detector surface ~ 50 km^2 that can probe neutrinos in an energy regime where current neutrino detectors, as for example IceCube, fall short in statistics due to the extremely low flux. On top of that, the characteristic attenuation of radio waves in ice is ~ $O(1\text{ km})$, while optical light scatters out ~ $O(100\text{ m})$ length scales. This allows for building large scale radio observatories with fewer instrumentation compared to optical observatories.

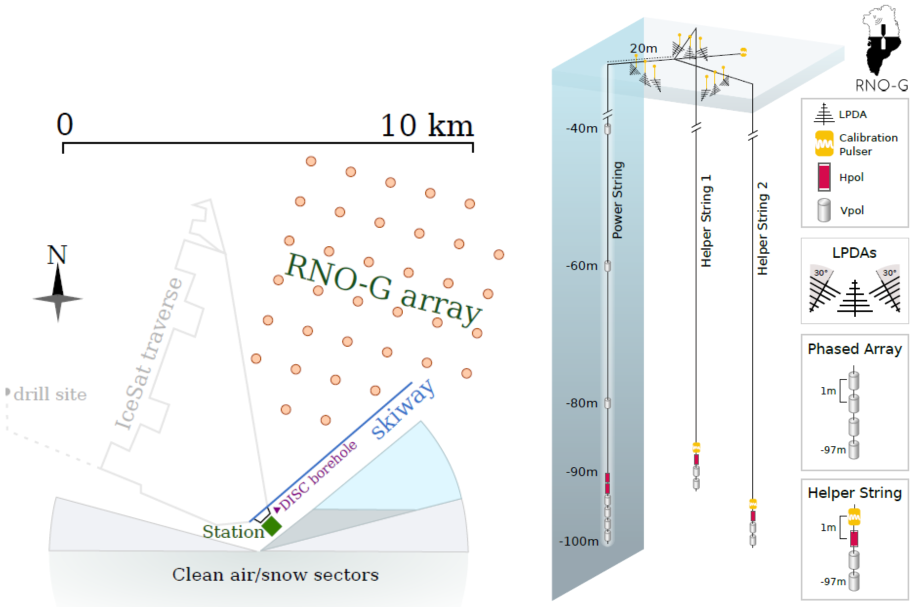

(a) (b)

Figure 3.7: (a) A top view of the planned RNO-G layout consisting of a total of 35 stations. (b) A schematic drawing of such an RNO-G station. Figures from [8] and [61].

3.3 Radar

This thesis focuses on a specific detection technique to investigate high-energy neutrino-induced particle cascades: Radio Detection and Ranging also known as *radar* [64]. As the name suggests, radar uses electromagnetic signals to detect and locate nearby objects. Just like sound waves get reflected when they hit an object, electromagnetic waves do too. This allows for sending out electromagnetic pulses and detecting their subsequent reflections. From these reflections, the location and velocity of the object can be determined. In its early days, during World War II, radar was a technique predominantly used by the military to detect enemy aircrafts and ships. In present days, the use of radar has expanded towards other domains as well. It is for example used in air traffic control and surveillance systems, but also in different scientific fields like astronomy and geology.

When high-energy neutrinos interact in matter, they produce a relativistic cascade of particles. These relativistic particles can subsequently ionize the surrounding medium creating a trail of nonrelativistic electrons and nuclei. Recent works [65, 66, 12] have shown that radar could be used to detect this ionization trail, provided it is dense. As the technique would have its peak intensity in the 10 – 100 PeV energy range, it would be able to cross the bridge between the other two detection techniques, Cherenkov and Askaryan detectors.

3.3.1 History

It was already suggested in 1941 by Blackett and Lovell [67] that radar could also be used as a detection technique for extensive air showers induced by high-energy cosmic rays. When such showers propagate through the atmosphere towards the Earth's surface, they strip off electrons from air molecules and leave behind a dense ionisation trail. Both scientists believed that this trail could act as a reflector of radio waves, provided its density was high enough. Blackett and Lovell showed that cosmic rays interacting at an altitude of 10 km with primary energies $E_p \geq 10^{16}$ eV could produce ionisation trails with sufficiently large reflection coefficients [67]. Such cosmic ray particle cascades were already detected by Auger and his group in 1938 [16] and hence the detection technique showed potential. Unfortunately, both Blackett and Lovell overlooked one very important fact in their calculations. The electrons in the ionization trails are not free but collide with the air molecules at a non-negligible rate. As such, collisional dampening has to be taken into account in the calculations, which reduces the returned power quite drastically. This fact was pointed out in a letter to Blackett by the scientist named T.L. Eckersley, but due to the chaos of World War II, the letter never got delivered to him [68]. Therefore, Lovell unknowingly started a radar experiment in 1941 at Jordell Bank in Manchester, UK, to detect the radio reflections of cosmic rays, doomed to never yield any discoveries. Finally, in 1946 after World War II had ended, the issue of collisional dampening pointed out by Eckersley reached the eyes and ears of Balckett and Lovell. Still, Lovell, showed that the most energetic cosmic rays could be detected using radar if a larger antenna was used. At the end of the year 1946, they concluded that all the observed reflected signals originated from meteors [69] instead of cosmic rays, in agreement with previous work [70]. Hence, both Balckett and Lovell threw in the towel on the radar detection technique of high-energy cosmic rays.

In 2000 the technique was revisited and led in the subsequent decade to the deployment of a full-scale experiment called the Telescope Array RAdar (TARA) [71]. Until the present day, TARA has not yet observed the in-air radar signal from a high-energy cosmic ray and other work has proven that the in-air detection via radar is not feasible [72].

Fortunately, this did not mean the end of the radar detection technique for relativistic particle cascades. It became clear from all the previous efforts of in-air detection that the electron density in the ionization trail is too small to result in a detectable radar signal. Hence, it intuitively made sense that if such particle cascades can develop in a denser medium than air, for example ice, the resulting ionization would be compressed in a smaller region leading to a higher electron density. Several groups [65, 66, 12] investigated this possibility. All of these studies agreed radar detection would be possible, but depends strongly on parameters like the electron lifetime and collision rate which are not well known for dense media like ice.

3.3.2 Experiment T576 at SLAC

In 2020 experiment T576 at the Stanford Linear Accelerator Center (SLAC) [9] observed for the first time a radar signal from a high-energy particle cascade, induced by an electron beam. As this result was the first proof of the feasibility of the radar detection technique, this section is dedicated to the experiment.

The SLAC National Accelerator Laboratory is located in California, USA. It is a linear particle accelerator that can accelerate electrons to energies of 50 GeV. The T576 experiment used a SLAC electron beam to hit a high-density polyethylene (HDPE) target and produced a particle cascade with properties similar to an in-ice neutrino-induced cascade with $E_p \sim 10^{19}$ eV [9].

They used one transmitter antenna (TX) to broadcast continuous-wave radio into the target and three receiver antennas (RX) to detect the radar reflection. A schematic overview of the setup can be found in Figure 3.8. Two types of antennas were used in the setup: a Vivaldi-style, ultra-wide-band antenna and a log-periodic dipole antenna. Both types of antennas were operating at around $\sim$ 2 GHz. During the different runs, the position of both the TX and RXs were changed and data was collected for each setup. This allowed for performing geometry-independent data analysis [9].

In the data analysis, numerous sources of background had to be taken into account. These background sources can exceed the actual radar signal by a factor of 10-100 and therefore need to be carefully removed from the data [9]. One of the main sources of background is the so-called beam splash. This background originates from the movement of the beam from the beampipe into air and its subsequent movement into the HDPE target. During this movement the refractive index changes, which can lead to the emission of electromagnetic radiation, and thus radio waves. The other main background signal was the continuous-wave emission from the TX antenna.

After a filter process separating the actual radar signal from the background, a time-frequency spectrogram was made showing a clear excess signal at frequencies similar to the transmit frequency of 2 GHz and with a duration of a few nanoseconds [9]. This was observed at different antenna positions. These signals were compared with theoretical predictions produced using the *Radioscatter* [73] and *MARES* [12] simulation software and were in good agreement. It was investigated if the signal could be a consequence of a random background fluctuation. The probability of this being the case was found to be completely negligible [9].

As such, the T576 experiment at SLAC was the first definitive observation of the radar echoes from a high-energy particle cascade with similar properties to an in-ice neutrino-induced particle cascade. This showed that the technique is promising for detecting neutrinos in a different way than the more conventional approaches using Cherenkov and Askaryan detectors. This led to the development of an experiment called the Radar Echo Telescope (RET) discussed in full detail in the next section.

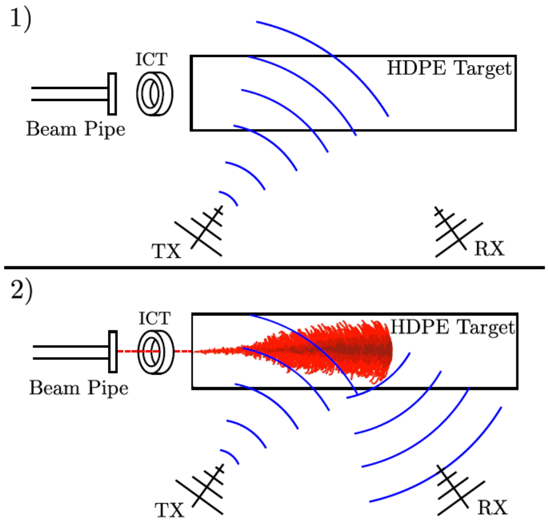

Figure 3.8: Illustration of the radar method for the T576 experiment at SLAC. Panel 1) shows how the transmitter antenna (TX) illuminates the plastic target. Panel 2) shows how a particle cascade induced by the electron beam leaves behind an ionization trail (red) that reflects the transmitted signal towards a receiver antenna (RX). Figure from [9].

3.3.3 The Radar Echo Telescope

The Radar Echo Telescope (RET) is a developing experiment that aims to detect ultra-high energy neutrinos (UHEN), $E_p \geq 10$ PeV. This experiment will consist of two main phases. The Radar Echo Telescope for Cosmic Rays (RET-CR) [74] will be deployed first to test the radar echo technique in nature after the successful lab results from the T576 experiment [9]. The Radar Echo Telescope for Neutrinos (RET-N) [10] will be deployed in a second phase to search for UHEN in an energy regime, 10 – 100 PeV, difficult to probe with other existing neutrino experiments.

RET-CR

When a cosmic ray with primary energy above 10 PeV interacts in the atmosphere, its extensive air shower can reach Earth's surface. The typical energy deposited by this air shower is around 10% of the primary energy for an ice sheet at high altitude, $\sim$ 2 km [74]. As most of the shower energy is centred around the cascade axis, the initial air shower can propagate further into the ice as a dense secondary cascade of roughly 10 m long and with a radius of approximately 10 cm. As ice is a thousand times more dense than air, the secondary cascade can presumably create an ionization trail detectable by radar. Hence, the existing air showers from cosmic rays are used as the in-nature equivalent of the electron beam in the T576 experiment hitting ice as a target instead of plastic. RET-CR will thus probe the radar technique in nature.

The experimental concept of RET-CR is shown in Figure 3.9. The setup consists of two main parts: the surface detector and the radar echo detector [74]. The surface detector consists of an array of scintillator

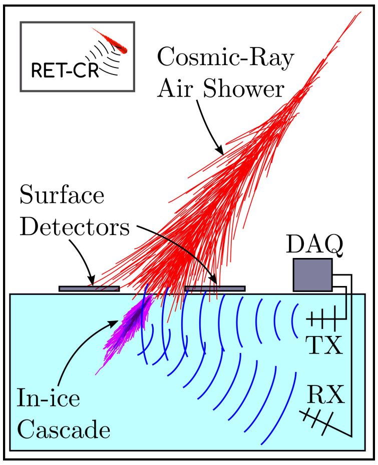

Figure 3.9: The experimental concept of RET-CR. A cosmic ray interacts in the atmosphere and induces an extensive air shower that reaches the icy surface. A secondary more dense cascade propagates further in the ice and is detected via radar using a bistatic setup. Figure from [74].

plates[1] to detect the extensive air shower from a cosmic ray reaching the surface. The surface detector has two main goals. First, provide a trigger for the radar system to collect data. Second, to be used to reconstruct the air shower. The surface detector will be composed of multiple stations. Each of these stations consists of two scintillators separated over a distance of 20 m, a SKALA radio antenna that operates at a frequency range 30 − 300 MHz, a power system, and a data acquisition system (DAQ) [74]. As the surface detector is used to trigger, it ensures that only cosmic rays with sufficiently high enough energy, $E_p \geq 10^{16.5}$ eV, are detected using radar and that the DAQ system does not overload [74]. The goal is to reconstruct parameters such as the energy, arrival direction and vertex position of the in-ice cascade using the radar detection technique. The surface detector array allows for an independent reconstruction of these parameters and can be used to validate the radar reconstruction [74]. It has to be noted that using the particle detectors as triggers, various radar trigger systems can be tested. As the future RET-N experiment will detect neutrinos, only a radar trigger can be used. Hence, testing is important and crucial for the success of RET-N [74].

The radar echo detector consists of a phased array transmitter (TX)[2] and eight receiver antennas (RX). The TX phased array consists of 8 vertically polarized antennas that are buried 2 – 20 m below the ice surface [74]. As the secondary cascade only penetrates in the first 10 m of the ice, the highest sensitivity is required in this region. The phased array allows for having a beamed gain pattern that is maximised near the surface and has a full azimuthal coverage [74]. Currently, a prototype of the RET-CR experiment is being deployed in Greenland.

RET-N

RET-N is a yet-to-be-deployed experiment and forms the second phase in the RET experiment. The information in this section is therefore completely based on the proceeding [10] and will cover the detector layout and expected sensitivity of the experiment. It should be noted that the final results for both can change based on the ongoing studies regarding the signal properties, the subject of this thesis, and reconstruction.

[1] A scintillator is a material that emits light when charged particles pass through. They are commonly used in particle detectors [75].

[2] A phased array is an antenna setup that allows for creating high gain in a specific direction. By letting multiple antennas constructively and destructively interfere with each other, directional gain patterns can be created. This pattern depends on the type of antenna used, the number of antennas and their relative positions. An educational and clear video explaining the concepts behind phased arrays can be found here.

In Figure 3.10, the proposed layout of a single detector station is shown. The entire setup is located 1.5 km deep in the ice. The reason why the detector is placed at such large depths is to stay far away from the firn. The ice layer in for example Greenland is formed via the compression of snow accumulated over time, and with that, creates a large density gradient in the top ~ 100 m of ice. The propagation of radio waves in this firn is rather complex and can lead to additional uncertainties in reconstruction [10]. By placing the detector station way below the firn, a constant refractive index of ice can be assumed, n_{ice} = 1.78, and no ray-tracing is required [10]. The detector station can contain a single central isotropic TX or an array of multiple TX antennas. In the presented simulation study, the TX emits continuous waves of 250 MHz at 40 kW of effective radiated power [10]. A total of 27 RX antennas are used in one detector station. These antennas are spread out over three different layers, each layer containing nine antennas. As can be seen from Figure 3.10, the three layers are stacked on top of each other with a separation distance of 20 m. In every layer, the RX antennas are placed in a circle centred around the TX antenna at a radial distance of 200 m.

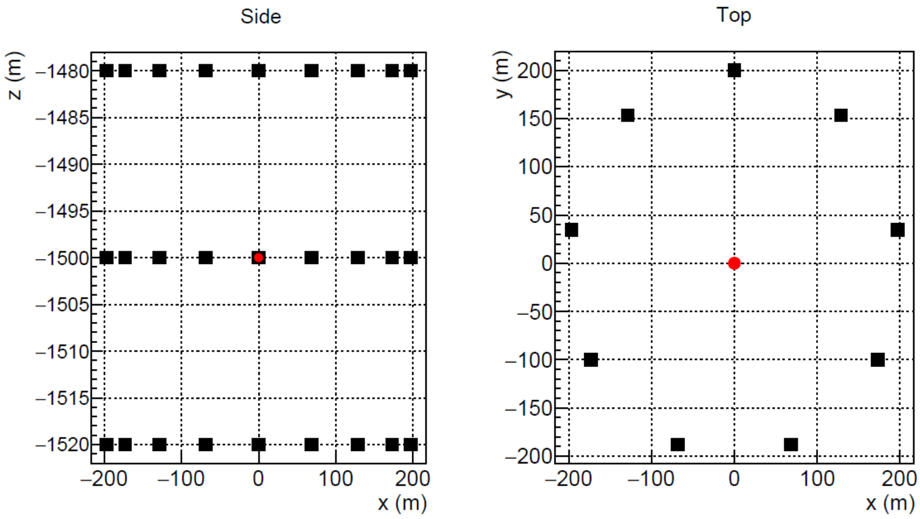

Figure 3.10: The experimental setup of a RET-N detector station viewed from the side and top. The receiver antennas are indicated in black and the transmitter in red. Figure from [10].

The expected sensitivity of RET-N for 10 detector stations, as described above, is shown in Figure 3.11. This sensitivity is obtained from simulations using the RadioScatter software by generating 5×10^5 events in a cylindrical shaped volume of ~ 35 km^3, with height 2.8 km and radius 2 km [10]. From these simulations, it becomes clear that RET-N should have an excellent sensitivity in the energy range PeV − EeV. Increasing the number of stations would of course increase the sensitivity and should allow RET-N to probe the most energetic neutrinos.

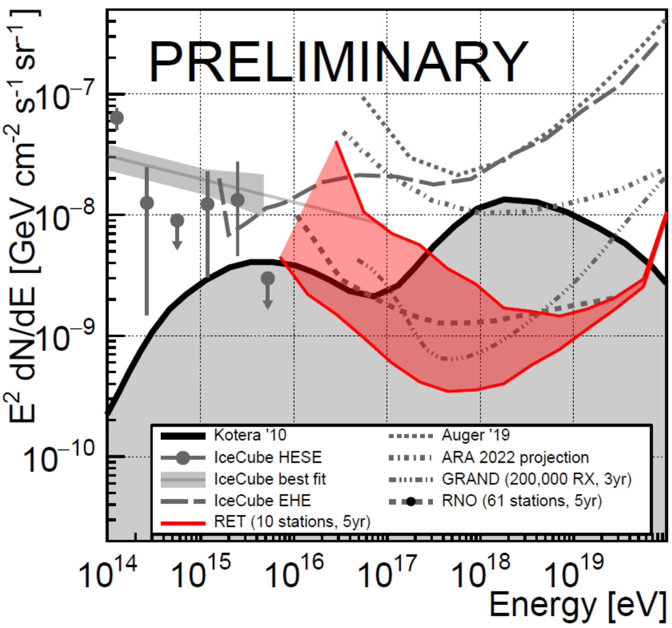

Figure 3.11: An overview of the sensitivity of multiple experiments as a function of the energy of the primary neutrino. RET-N is shown in red for a 10-station detector setup. The band shows the sensitivity for different trigger conditions. Figure from [10].

Chapter 4

MARES: A simulation tool for radar detection of high-energy particle cascades

In this chapter, an overview is given of the simulation software MARES [12]. MARES stands for Macroscopic Approach to the Radar Echo Scatter and is a simulation tool designed to study the radar echo signals from high-energy particle cascades. The goal of this thesis is to investigate the radar signal properties of neutrino-induced particle cascades in ice for the future RET-N experiment. The MARES software is used extensively in the pursuit of this goal. It is noted that MARES is completely developed by Enrique Huesca Santiago and Krijn de Vries [12] and not by the author of this thesis.

As the investigation of the signal properties is fully based on MARES and the model it adopts, a part of this writing is dedicated to it. First, the model behind MARES is summarized and follows the official paper [12], though a detailed derivation and additional background information can be found in Appendix A. Second, in order to get familiar with using MARES, the first part of the thesis consisted of reproducing the results from the paper [12]. On top of that, some new additional verifications regarding simulation parameters and more are discussed at the end of this chapter.

4.1 Introduction

Simulating high-energy particle cascades is generally done through two different methods. The first approach uses Monte Carlo techniques to simulate the passage of a particle through a certain material. A well-known example of such software is GEANT4 [76]. Radioscatter [73] is a particle-level-based simulation that uses GEANT4 to simulate the particle cascade, after which it calculates the radar echo signal from the cascade. Generally, Monte Carlo techniques are computationally heavy. In the case of a particle cascade, the energy of the primary determines how many particles are being produced. From the Heitler model in Section 2.3.3 it became clear that this can be quite a lot, hence leading to longer computational times. The second method treats the problem analytically. MARES is an example of such an approach. The benefit of analytical models is that they are often much faster than Monte Carlo techniques. Still, analytical models often require making assumptions and simplifications in treating the problem which leads to the loss of some physical accuracy in the simulations. Therefore, both simulation techniques are complementary used in physics.

The radar detection technique tries to observe the radar echo signal from the ionization trail left in the wake of the particle cascade. Hence, this is sort of a three-body problem: the electric field of the transmitter antenna is observed by the receiver antenna through the ionization trail that acts as a mirror. As will become clear later on, this makes the interpretation of the results in this work sometimes rather difficult. The model behind MARES treats this problem analytically by first calculating the secondary electric field emitted by a single electron observed by a receiver antenna. Next, it makes the required assumptions to group multiple of these single-particle scatters into one segment that emits coherently. This allows for reducing the computational time quite drastically. Finally, it adds up the electric fields of all segments building the entire ionization trail keeping in mind the phase offsets between them. Needless to say, this is only a general roadmap of the calculations done each time a simulation is performed in MARES. The next section summarizes the most important equations and assumptions made in the MARES model but more details together with additional background information can be found in Appendix A.

4.2 The model

The main goal of MARES is to simulate the observed electric field at the receiver antenna, given a certain transmit antenna and particle cascade. The expression of the observed electric field $\vec{E}_R$ will depend on numerous properties like for example the transmit frequency and power, but also the primary energy of the cascade and its direction. In order to find an expression for $\vec{E}_R$, the amplitude of the signal and its phase are treated separately and combined at the end. On top of that, the ionization trail is considered to be a collection of segments, where each segment has N_i number of scatterers. These scatterers are the electrons making up the trail. A visualisation of the geometry can be found in Figure 4.1

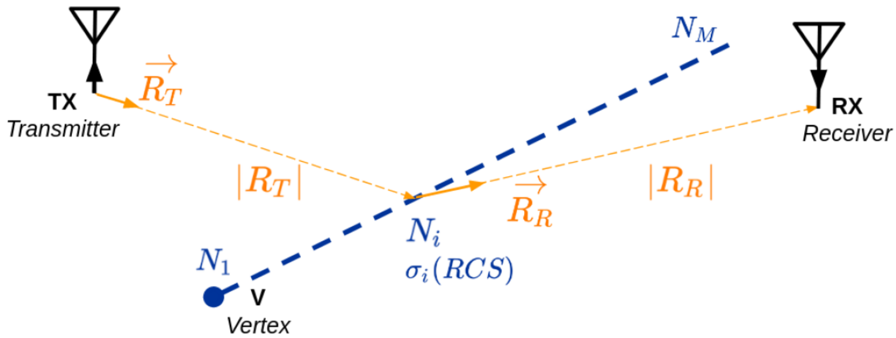

Figure 4.1: A schematic visualisation of the radar scatter from a segmented ionization trail assumed in MARES. Figure from [12].

Finding the amplitude of a macroscopic segment $|E_{R,i}|$ can be done starting from the **radar range equation** as it relates the transmitted power and the received power through a radar echo from a macroscopic object [77]:

$$P_R = P_T \frac{G_T(\theta,\phi)G_R(\theta,\phi)\lambda^2}{(4\pi)^3(R_T R_R)^2}\sigma_{RCS} \, . \tag{4.1}$$

In this equation P_T is the transmitted power, P_R the received power, $G_T(\theta,\phi)$ the gain of the transmitter, $G_R(\theta,\phi)$ the gain of the receiver, λ the transmit wavelength, R_T the distance between the transmitter and a trail segment, R_R the distance between the receiver and a trail segment and σ_{RCS} the radar cross section of a segment. The form of this equation can be understood as the power arriving from the transmitter at the the trail segment yields a factor of $P_T G_T(\theta,\phi)/(4\pi R_T^2)$. This macroscopic segment in the trail has an effective area σ_{RCS} and reflects all of its captured power towards the receiver resulting in a factor $1/(4\pi R_R^2)$. The effective area of the receiver antenna itself is $G_R(\theta,\phi)\lambda^2/(4\pi)$ and hence all the factors in Equation (4.1) are understood. The radar range equation can be transformed into an expression for the received electric field amplitude using the medium impedance Z_{ice},

$$|E_R| = \frac{\sqrt{2 Z_{ice} P_T G_T(\theta,\phi)}\sqrt{\sigma_{RCS}}}{4\pi R_T R_R} \, . \tag{4.2}$$

The unknown left in the radar range equation is the radar cross-section of the segment. As the segment consists of N_i electrons, the next step in the calculation is to determine the scattered electric field from an individual electron and its radar cross-section.

An electron inside the ionization trail is subjected to the electric field of the transmitter. Hence, the charged particle feels an external force that tries to displace it. As the electron is surrounded by ice and is not located in a vacuum, it will experience a frictional force corresponding with a dampening rate $\omega_c/(2\pi) = 100 \pm 50$ THz. These values of collisional dampening are consistent with previous works [12]. From the above, it becomes clear that the electron's motion can be modelled as a damped-driven oscillation, described in more detail in Appendix A. Hence, the solution to the equation of motion (e.o.m.) is given by

$$x_e(t) = \frac{q|E_e|}{m} W \cos(\omega t - \delta) \ , \tag{4.3}$$

where $W = 1/(|\omega^2 - i\omega\omega_c|)$ is the collisional ratio, $q|E_e|/m$ the magnitude of the driving force originating from the electric field of the transmitter, ω the anuglar transmit frequency and δ the phase shift w.r.t. the driving electric field. Now that the solution to the e.o.m. is found, the scattered electric field of the electron can be calculated from the Liénard–Wiechert potentials yielding the general expression for the electric field [38],

$$\vec{E}_{e,R} = \frac{q}{4\pi\epsilon_0} \frac{R_R}{(\vec{R}_R \cdot \vec{u})^3} [\vec{R}_R \times (\vec{u} \times \ddot{\vec{x}}_e)] \ , \tag{4.4}$$

where q is the electron charge, ϵ_0 is the permittivity in vacuum, $\vec{R}_R$ is the distance vector between the electron and receiver, $\vec{u} = c\hat{R}_R$ and $\ddot{\vec{x}}_e = \omega^2 \vec{x}_e(t)$ by taking the second order derivative of Equation (4.3). The expression for the electric field is condensed into a more usable form to finally obtain,

$$\vec{E}_{e,R} = \frac{|E_e|\omega^2 W}{R_R} \left(\frac{\sigma_{Th} G_{Hz}}{4\pi} \right)^{1/2} \hat{p} \ . \tag{4.5}$$

This final form is written as a function of the Thomson scattering cross-section $\sigma_{Th} = 8\pi r_e^2/3$ that depends on the classical electron radius r_e and the gain of a Hertzian dipole $G_{Hz} = (3/2)\sin^2\theta$. The unit vector $\hat{p}$ is the polarisation direction of the scattered wave. Finally, by substituting the above equation into the radar range Equation (4.2) the radar cross-section of an electron is found to be

$$\sigma_{RCS,e} = (\omega^2 W)^2 \sigma_{Th} G_{Hz} \ . \tag{4.6}$$

The MARES model assumes all the electrons in a single segment are emitting their radiation coherently. This is valid as long as the dimensions of the segment d_x, d_y, d_z are typically smaller than the wavelength λ_T of the EM wave probing them. Such an argument was already mentioned and discussed in Section 3.2 about Askaryan radiation. On top of that, the distance between the relevant objects also affects the phase coherence condition. There is the transmitter-segment distance R_T that needs to be taken into account as well as the segment-receiver distance R_R. Hence, phase coherence is satisfied if $d_x, d_y, d_z \ll R_T, R_R, \lambda_T$ [12]. As long as this condition holds, constructive interference between all electrons in a single segment can be assumed and the received electric field from one such segment is given by

$$|\vec{E}_{R,i}| = |N_i \vec{E}_{e,R}| \ . \tag{4.7}$$

The radar cross-section of a segment can now be derived by substituting the above expression for the received electric field into Equation (4.2) and using the derived expression for $\sigma_{RCS,e}$ in Equation 4.6,

$$\sigma_{RCS,i} = N_i^2 \sigma_{RCS,e} \ . \tag{4.8}$$

At this point, the electric field emitted by a single segment inside the ionization trail is known from the radar range equation and the just derived expression for the radar cross-section. Still, one parameter remains unknown which is the amount of electrons in a segment N_i. The ionization trail which creates the radar echo signal is the result of the relativistic particle cascade traversing the ice. As such, the electron distribution depends on the development of the particle cascade. This cascade can be modelled using a parametrization for its longitudinal and radial profile. MARES uses the Greisen profile [78] for the longitudinal dimension of the cascade given by,

$$N(X, E_p) = \frac{0.31}{\sqrt{\ln(E_p/E_{crit})}} e^{\frac{X}{X_0}(1 - 1.5\ln(s))} \tag{4.9}$$

where X is the column depth traversal by the cascade expressed in g/cm^2, E_p the energy of the primary, E_{crit} = 78.6 MeV the critical energy analogue to the one in the Heitler model described in Section 2.3.3, s the shower age [79] and X_0 = 36.08 g/cm^2 the radiation length in ice [80]. The radial profile is given by the Nishimura and Kamata parametrization [81]:

$$w(r,s) = \frac{\Gamma(4.5-s)}{\Gamma(s)\Gamma(4.5-2s)}\left(\frac{r}{r_0}\right)^{s-1}\left(\frac{r}{r_0}+1\right)^{s-1}, \tag{4.10}$$

where $\Gamma(s)$ are the classical gamma functions and r_0 the Molière radius which is defined as the radius of the cylindrical volume containing 90% of the shower's total energy. In ice r_0 = 7 cm [80]. These parametrizations do not take into account the energy losses of the relativistic particles due to ionizing their surrounding. Needless to say, as the radar detection technique depends on the ionization trail left in the wake of the cascade, it is important to take this into account. A constant average energy loss of 2 MeV/g/cm^2 is assumed.

In order to find the number of ionizing electrons, a mean ionizing energy of 69 eV is assumed. This implies that on average, around 10^5 ionization electrons are created per relativistic lepton inside the cascade per unit of length ($N_{ion,e}dX$) [12]. Hence by simply multiplying this value with the number of cascade particles yields the total number of ionized electrons at a certain depth in the shower [12]

$$n_{e,plasma}(X,r) \simeq \frac{N_{ion,e}dX}{dV}\int_r^{r+dr} N(X,E_p)w(r',s)dr' \, . \tag{4.11}$$

An example of the electron density profile described by Equation (4.11) is shown in Figure 4.2. From Figure 4.2a it is clear that the ionization profile is most dense in a very narrow region in the radial direction compared to the longitudinal. This will be characteristic for every particle cascade and will become important when investigating signal properties in Chapter 5.

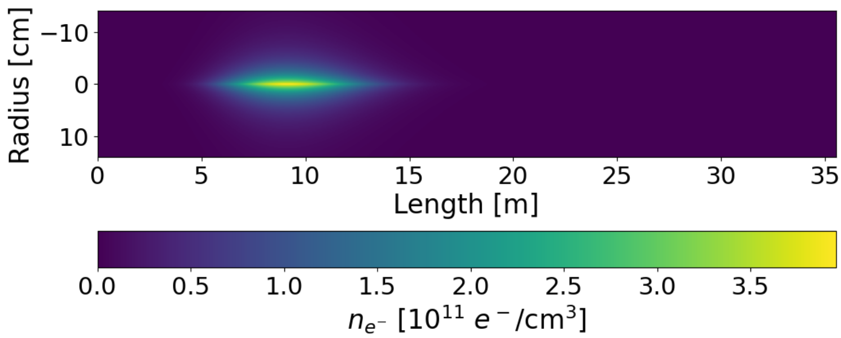

(a)

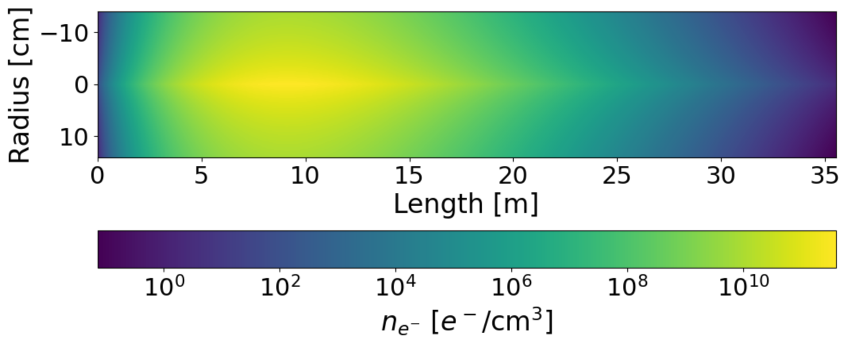

(b)

Figure 4.2: The electron density of the ionization trail left in the wake of a particle cascade. The primary energy is E_p = 1 EeV. In the top panel (a) a linear scale is used for the colour map showing the very compact region where most electrons are sitting. The bottom panel (b) shows the electron density in a log scale revealing more structure. Figures reproduced and adapted from [12].

Before continuing to the phase information of the radar echo signal, it is important to note that two additional corrections must be made to the amplitude. More details about these corrections can be found in Appendix A. The electrons have a finite lifetime, meaning they will recombine with the ice molecules after a characteristic lifetime τ. As such the number of electrons inside a segment becomes time depended. The electron density map shown in Figure 4.2 corresponds with the amount of electrons in each segment upon creation. On top of that, the electromagnetic wave is attenuated when travelling through the ice with a characteristic length L_{att} = 1.45 km and is based on actual in-situ measurements of the average attenuation length of the Antarctic ice [82]. By taking into account these corrections, the amplitude of the electric field at the receiver from a single segment is found by using the radar range equation (4.2) and the radar cross-section (4.8),

$$|E_{R,i}| = \frac{\sqrt{2Z_{ice}P_T G_T}}{4\pi R_T R_R} \sqrt{\sigma_{RCS,i}(t,t_0)}\; e^{-(R_T+R_R)/L_{att}} \;. \tag{4.12}$$

The electric field at the receiver antenna is the sum of the electric fields from all individual segments. These segments are not necessarily coherent emitters and the phase information must be taken into account. The phase for each segment $\varphi_i = kR_i - \omega t + \psi$ has three different components [12]:

1. $kR_i = k(R_T + R_R)$ is the natural phase shift that occurs due to the propagation of the EM wave when following the path transmitter-segment-receiver.
2. ωt corresponds with the shift at the receiver depending on the time of emission by the scattering segment.
3. ψ is the component taking into account the unique relative shift between segments. This phase shift originates from the damped-driven oscillation and is equal to the phase shift δ in Equation (4.3). In the over-damped case ($\omega \ll \omega_c$), this phase shift is constant and $\psi \approx -\pi/2$.

As such, the amplitude of the electric field at the receiver coming from the entire ionization trail consisting out of M segments is

$$|E_{R,plasma}(R,t)| = \left| \sum_{i=1}^{M} E_{R,i}(R_i,t)\; e^{i(kR_i - \omega t + \psi)} \right| \,, \tag{4.13}$$

where $|E_{R,i}(R_i,t)|$ is given by equation (4.12).

4.3 Reproducing results

In order to provide a cross-check and get familiar with the software, some of the previous results from the MARES paper [12] are reproduced. In this section those results are outlined and discussed as they form the starting point for the investigation of signal properties.

4.3.1 Plasma lifetime effects

An important parameter in the MARES model is the lifetime of the electrons making up the ionization trail. Therefore, the influence of this parameter on the radar echo signal is investigated by looking at the number of electrons alive in the ionization trail as a function of time and the shape of the voltage pulse observed by the receiver. In Figure 4.3, the number of electrons, for a primary neutrino with energy E_p, as a function of time is shown. The different graphs shown in this figure are calculated analytically using the equations in Section 4.2. Equation (4.9) gives the number of high energy particles in the cascade as a function of E_p and the column depth X. Each of these high-energy particles can ionize a certain number of electrons. As mentioned

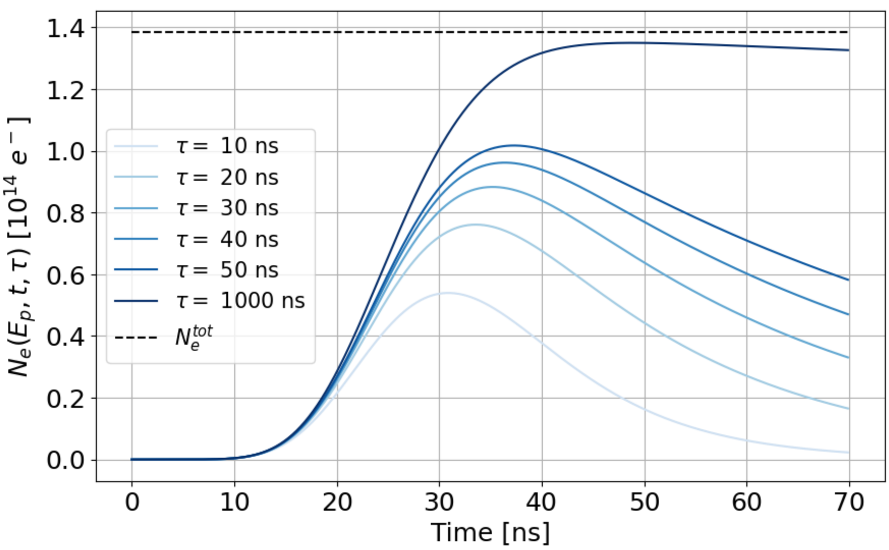

Figure 4.3: The number of ionized electrons as a function of time for a neutrino with primary energy E_p = 10 PeV. The horizontal dashed line represents the maximum number of electrons that can be generated by the cascade.

in Section 4.2, this number $N_{e,ion}$ depends on the assumed mean ionization energy per electron, chosen to be 69 eV, and the energy loss of the cascade particle, E_{loss} = 2 MeV/g/cm^2. In order to transform Equation 4.9 from a dependency on X to the time t, the column depth is replaced by $X = c \cdot \rho_{ice} \cdot t$ where it is assumed that the cascade particles move with the speed of light in vacuum and the density of ice, ρ_{ice} = 0.92 g/cm^3. Finally the formula for the number of ionization electrons alive at a certain time for a specific plasma lifetime τ is found by the convolution

$$N_e(E_p, t, \tau) = N(E_p, c \cdot \rho_{ice} \cdot t) \cdot N_{e,ion} \circledast e^{-t/\tau}\Theta(t) \,, \tag{4.14}$$

where $N(E_p, c \cdot \rho_{ice} \cdot t)$ is given by Equation (4.9) and $N_{e,ion} = 8.7 \times 10^5 e^-/ns$ is the number of electrons ionized per cascade particle assuming the previously mentioned energy loss. From Figure 4.3 it can be concluded that the peak number of electrons increases with increasing lifetime and the moment when this peak is reached occurs later. When more secondary particles are alive to scatter the incoming wave from the transmitter, a stronger radar echo will be created that is subsequently easier to detect.

In Figure 4.4 the effect of the lifetime on the voltage profile of the radar signal is investigated. It is clear from this figure that by increasing the lifetime from 1 ns to 30 ns, both the total duration of the signal and its amplitude increase. A longer lifetime increases the amount of particles alive at each instance of time leading to a stronger signal. An increase in lifetime also implies that the ionization trail is longer around to scatter. Interestingly enough, for a lifetime above 30 ns the signal duration keeps increasing but the amplitude does not. This implies that the full ionization trail is alive at a single moment in time. Evidently, increasing the lifetime will still increase the total duration of the pulse. This is illustrated by the clear exponential behaviour of the amplitude that decays more slowly when increasing the lifetime. This pattern is also expected to occur from Equation 4.14.

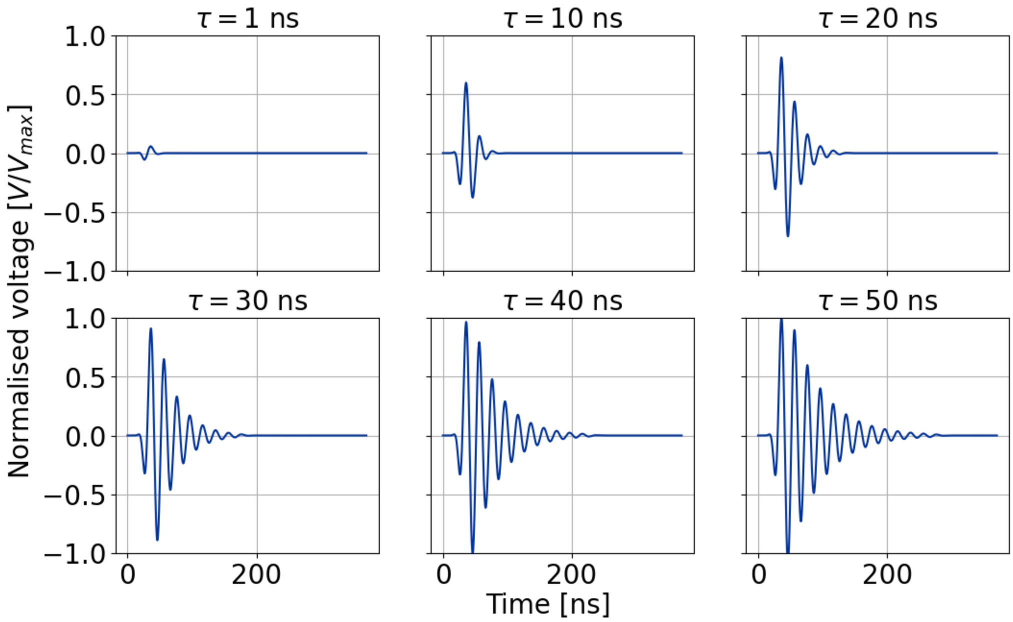

Figure 4.4: Voltage pulse shape for different plasma lifetimes. All six profiles are normalised to the peak value of the $\tau = 50$ ns.

4.3.2 Cascade direction effects

The direction of the cascade development relative to the antennas also influences the signal as the system suffers from relativistic effects due to the cascade propagating near the speed of light. A specific antenna geometry was chosen for the simulations and is shown in Figure 4.5. A transmitter antenna (TX) is located at $(0, 0, -100)$ m and a receiver antenna (RX) at $(-250, 0, 0)$ m. The cascade vertex, or starting point, is located at the origin of the reference frame. The cascade direction is indicated by the arrow in the figure and is parameterised by two angles. The zenith angle θ is the angle between the cascade direction and the z-axis. The azimuth angle lies in the xy-plane and is the angle between the positive x-axis and the projected cascade direction. This specific geometry was chosen such that the zenith angle expresses the orientation of the cascade with respect to the transmitter: $\theta = 0°$, corresponds with the cascade moving straight away from the transmitter while $\theta = 180°$ is moving head-on towards the transmitter. The azimuth angle expresses the relative orientation of the cascade with respect to the receiver: at $\phi = 0°$ the cascade is moving straight away from the receiver while at $\phi = 180°$ it is moving right at it. Given this specific detector setup, in Figure 4.6, the simulated waveform for three different cascade directions is shown for a transmit frequency of $f(TX) =$ 50 MHz. A waveform shows the voltage, or electric field, as a function of time observed by the receiver. The three cascade directions in Figure 4.6 have the same fixed zenith angle $\theta = 90°$, implying the cascade is moving in the xy-plane, but a varying azimuth angle. The three chosen angles correspond with the three most natural cases,

1. $\boldsymbol{\phi} = \mathbf{0}°$: the cascade propagates in the $+\hat{x}$-direction moving away from the receiver
2. $\boldsymbol{\phi} = \mathbf{90}°$: the cascade propagates in the $+\hat{y}$-direction moving parallel with respect to the receiver.
3. $\boldsymbol{\phi} = \mathbf{180}°$: the cascade is propagating in the $-\hat{x}$-direction moving straight towards the receiver.

As becomes clear from Figure 4.6, the shape of the waveform changes according to the cascade direction, indicating that relativistic effects are at play. When the cascade moves towards the receiver, the signal is compressed resulting in higher frequencies and a blueshift as is expected from relativistic Doppler effects. When the cascade moves away from the receiver, the opposite effect arises leading to a redshift of the signal stretching it out. When the cascade moves along the $+\hat{y}$-direction little relativistic Doppler effects are expected. More details on the theory behind the relativistic Doppler effect can be found in Appendix B. From Figure 4.6 it is clear that the amplitude also varies depending on the cascade direction. These first observations and results form the starting point for the rest of this work as they are an invitation to perform a more detailed study of the radar signal properties.

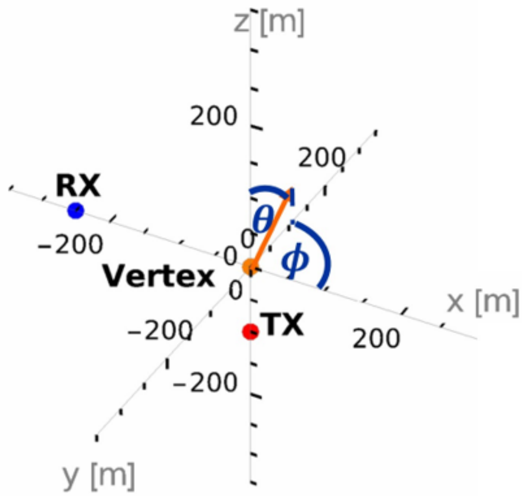

Figure 4.5: The detector setup for simulations. The transmitter (TX) is sitting at (0,0,−100) m and the receiver (RX) at (-250,0,0) m. The cascade vertex is at the origin of the reference frame. The cascade direction is indicated by the orange arrow and parameterised by the zenith angle θ and the azimuth angle ϕ.

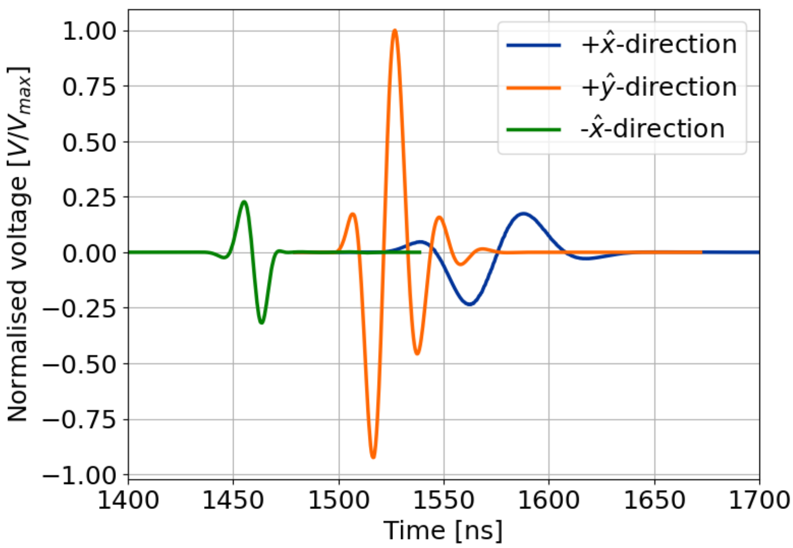

Figure 4.6: Waveforms simulated by MARES for three different cascade directions observed using a bistatic radar setup. The voltage is normalised to the peak voltage of the $+\hat{y}$-direction.

4.4 Verification of the physical correctness of MARES

In this section, some checks are performed to verify if MARES simulates the neutrino-induced particle cascade correctly. The first check tries to identify what are the minimal dimensions that need to be set in MARES in order to include all ionization electrons in the calculations. The second check is based on Figure 4.3, but instead of fixing E_p and varying τ, the opposite is done. Lastly, the relation between E_p and the peak voltage of the waveform is investigated.

4.4.1 Simulation dimensions

When MARES simulates the radar echo from the cascade, it draws an imaginary box around it and only calculates the net reflected signal from all of the ionization electrons inside this box. It is therefore important to make this box large enough such that most of the electrons are included. As the cascade is parameterised by the two profiles in Equation (4.9) and Equation (4.10), the box is parameterised by a longitudinal and radial dimension. A simple solution to this problem would be to take very large values for both dimensions, but at the cost of computational time. Therefore, it is investigated what the required lower bounds are for the size of the box in both dimensions to optimize computation time while remaining high physical accuracy for the simulation. It is common to express the longitudinal dimension in units of the interaction length L_{int} and the radial dimension in units of Molière radius r_0.

Longitudinal dimension: The approach of finding the lower bound on the longitudinal dimension is rather straightforward. Using MARES, the electron density profile of the ionization trail is simulated. This is repeated for different longitudinal dimensions of the box but a fixed radial dimension. These profiles are analogues to the one shown in Figure 4.2, but will have a different longitudinal length according to the chosen value. The radial size is taken large enough, $r = 3\ r_0$, to make sure most electrons in this dimension are included. From each of these density profiles, the total number of electrons is determined and multiplied by the energy to ionize a single electron, $E_{ion} = 69$ eV. This number gives the total energy of the ionization trail and should, due to energy conservation, be equal to the primary energy of the neutrino. For all these simulations $E_p = 1$ EeV. In Figure 4.7, the total energy inside the ionization trail is plotted as a function of the longitudinal dimension. It is clear from this figure that convergence is reached around $L = 1.5\ L_{int}$ and therefore corresponds with the lower bound for the longitudinal dimension of the simulation box. The total energy at convergence is not equal to 1 EeV. This can be explained by the fact that the profiles used in MARES to model the particle cascade only take into account the electromagnetic content of the cascade and not the hadronic part. For primary energies around 1 EeV it is expected that a minor part of the cascade is hadronic [36], explaining the energy value at convergence ~ 0.88 EeV. It is noted that the small deviations at convergence are caused by numerical fluctuations.

Radial dimension: The lower bound on the radial dimension cannot be found in an analogous way to the longitudinal dimension. The main reason is that the radial parametrization of the cascade given by Equation (4.10) does not converge. MARES takes care of this fact by renormalizing the radial particle distribution to the size of the chosen simulation box. This corresponds with squeezing the infinite radial distribution into a finite volume. Needless to say, this will always introduce an error in the simulation. Because of this fact, a slightly different approach is used to determine the lower bound on the radial dimension. First, the electron number density is simulated with MARES for different values of the radial size and a fixed longitudinal size of $L = 2\ L_{int}$. Second, for each simulation box, radial slices are taken out of the electron density profile and the corresponding energy in those slices is calculated. This corresponds with drawing horizontal lines in Figure 4.2 and summing all electrons within. The result of this procedure is shown in Figure 4.8 for four different radial sizes of the simulation box. The renormalization in MARES is clear from this figure as for every radial size the total energy adds up to the convergence value $E \sim 0.88$ EeV. This shows that MARES squeezes the infinite radial distribution into the chosen simulation box. The question remains how much MARES can squeeze without introducing too much error in the electron distribution. As the real radial distribution does not converge, instead a large radial dimension and its corresponding electron distribution are chosen as a reference to compare with. In this case, the $r = 5\ r_0$ is chosen to be the reference value. From Figure 4.8, it becomes clear that choosing a $r = 3\ r_0$ only introduces a slight error as the graph lies relatively close to the reference value. This implies that the bulk of the particles is sitting at an r-value much lower than the

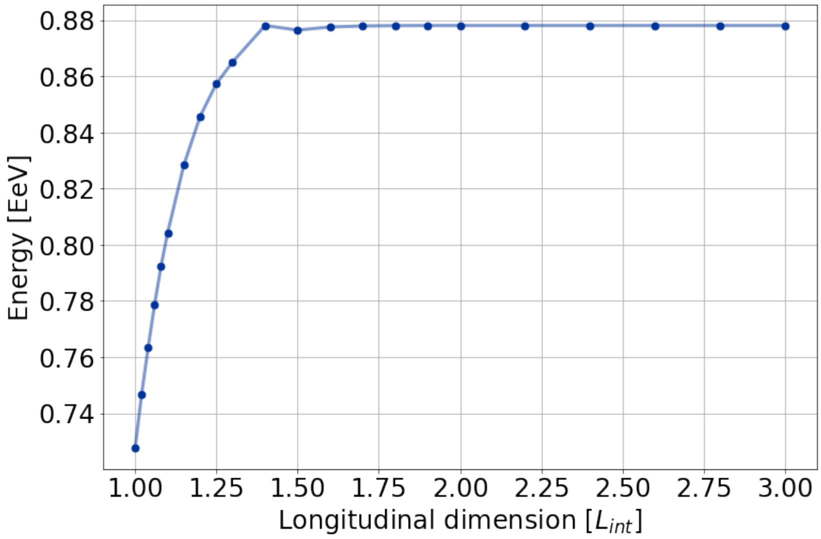

Figure 4.7: The total energy in the simulated ionization trail as a function of the longitudinal dimension of the simulation box. Convergence is reached at $L = 1.5\ L_{int}$.

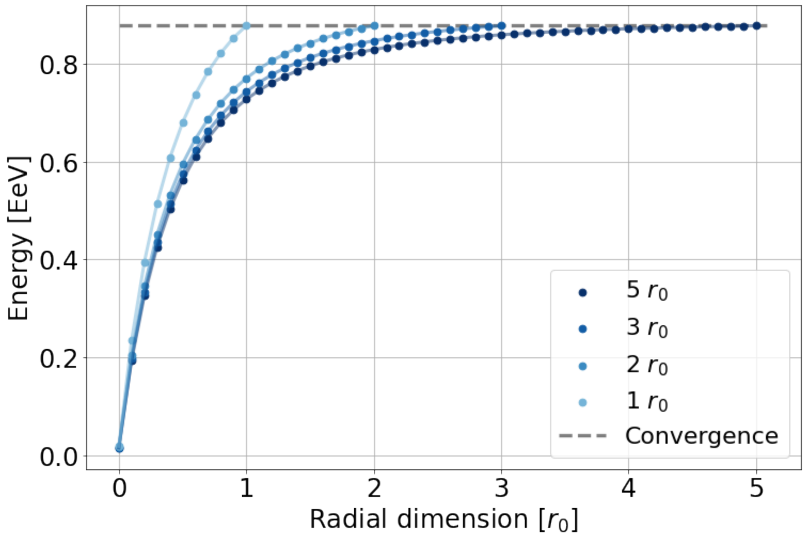

Figure 4.8: The total energy in a slice of the electron density profile as a function of the radial length of the slice taken for a simulation box with a total fixed radial size shown in the legend.

boundary of $r = 3\ r_0$. Choosing $r = 1\ r_0$, it becomes clear that this is not the case as a large discrepancy arises when comparing its graph to the reference value. This implies that the bulk of the cascade is spread over a wider range than $1\ r_0$ in the radial dimension and as such, the renormalization procedure is not appropriate. To have a more quantitative grasp on this error, the relative difference σ of the total energy between a box with radial size r_i and the reference value $r_{ref} = 5\ r_0$ is calculated. For example, when a simulation box is chosen with $r = 3\ r_0$, the total energy in this simulation box, which will be the convergence value, is compared with the value at $r = 3\ r_0$ for the reference simulation box with total size $5\ r_0$. This comparison is given by $\sigma = \left(\frac{r_i}{r_{ref}} - 1\right) \cdot 100$, where the deviation was multiplied with a factor 100 such that σ is expressed in percentage. The result for multiple radial simulation dimensions is shown in Figure 4.9. From this figure, it becomes clear that choosing a radial dimension below $r = 1.5\ r_0$ introduces an error less than 10%. To make sure the error is not too large, it is concluded that the lower bound on the radial dimension is $r = 2\ r_0$ as the error is only 5.86%. It is noted that this conclusion is depended on the choice of the reference size. Hence, the reference size should be taken carefully and ideally as large as possible. A radial dimension of $r = 5\ r_0$ is considered to be large enough based on the results shown in Figure 4.8. Following the pattern in this figure, it is clear that increasing the radial size above $5\ r_0$ will only give a small increase in accuracy with respect to the chosen reference value in this work of $r_{ref} = 5\ r_0$.

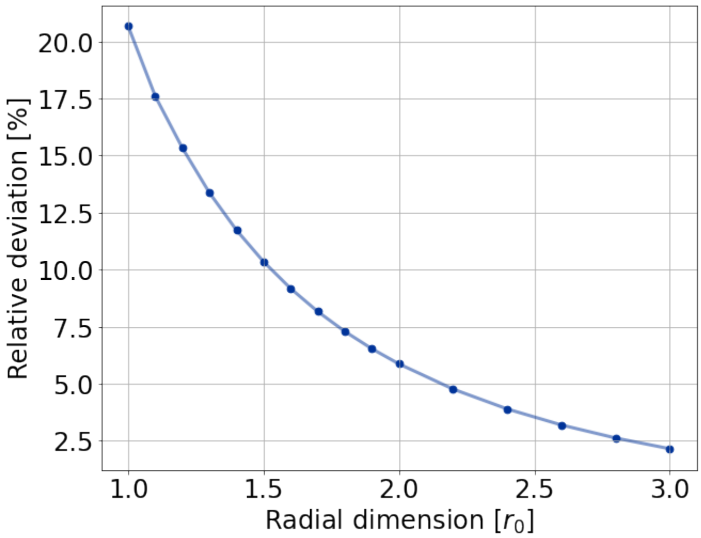

Figure 4.9: The error introduced by renormalizing the electron distribution as a function of the radial dimension of the simulation box.

From the results presented above, it was concluded to keep the simulation dimensions fixed for all simulations at $L = 2\ L_{int}$ and $r = 2\ r_0$. These values ensure convergence for the longitudinal dimension and introduce a small error for the radial dimension.

4.4.2 Primary energy versus electron number

This section is based on the results in Section 4.3.1. The electron number as a function of time is calculated for a fixed plasma lifetime, set to a realistic value $\tau = 10$ ns [83], but a varying primary energy . The result is shown in Figure 4.10. It is expected that the peak electron number $N_{e,max}(\tau)$ scales linearly with the primary energy. This is observed when looking at the figure, as the value for $N_{e,max}$ at $E_p = 75$ GeV is half of the value at $E_p = 150$ GeV. This is also verified quantitatively by plotting $N_{e,max}(\tau)$ as a function of E_p, shown in Figure 4.11. It is expected that there is a linear relationship $N_{e,max} \propto E_p$. In a log-log space, any straight line corresponds with a power law with power law index equal to the slope of the line. As such, fitting a straight line through the data points in log-log space should yield a slope $\alpha = 1$ in order to have a linear relationship between the two quantities. The fit yields a power law index of $\alpha = 0.9596 \pm 0.0017$. This is not consistent within three standard deviations σ with the expected value of $\alpha = 1$ but is presumably a consequence of some numerical errors. Therefore, it is concluded that a linear relationship is indeed observed.

The above results are all for $\tau = 10$ ns. It was observed that α changed depending on the lifetime. As no correlation is expected between the primary energy of the neutrino and the plasma lifetime of the ionization trail electrons, this is investigated a bit more in detail. First, the energy range of the primary is increased. The primary energy values for the power law fit are $E_p = 10^i$ GeV where $i = 1, 2, ..., 9$. Second, a large range of lifetimes starting from 0.1 ns to 1000 ns was taken with a stepsize of 0.5 ns. For all these lifetimes, the power law fit of $N_{e,max}$ versus E_p was performed and the power law index was retrieved. Finally, the power law index was plotted as a function of the plasma lifetime for which the result is shown in Figure 4.12. In this figure, the left panel shows a linear scale from which it is clear that the power law index changes only slightly as a function of plasma lifetime. The minimal value at 0.1 ns is $\alpha = 0.9594 \pm 0.0033$ while the maximal value at 1000 ns is 0.99858 ± 0.00016. The right panel in Figure 4.12, shows the same result but in a log-scale for the lifetime. It is clear from this figure that starting at 10 ns, the power law index remains almost the

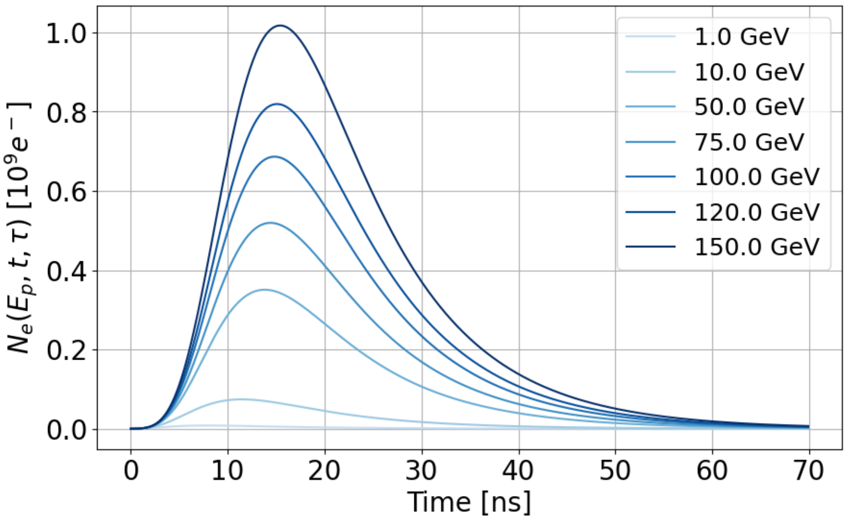

Figure 4.10: The electron number as a function of time for a fixed lifetime τ = 10 ns and different primary energies.

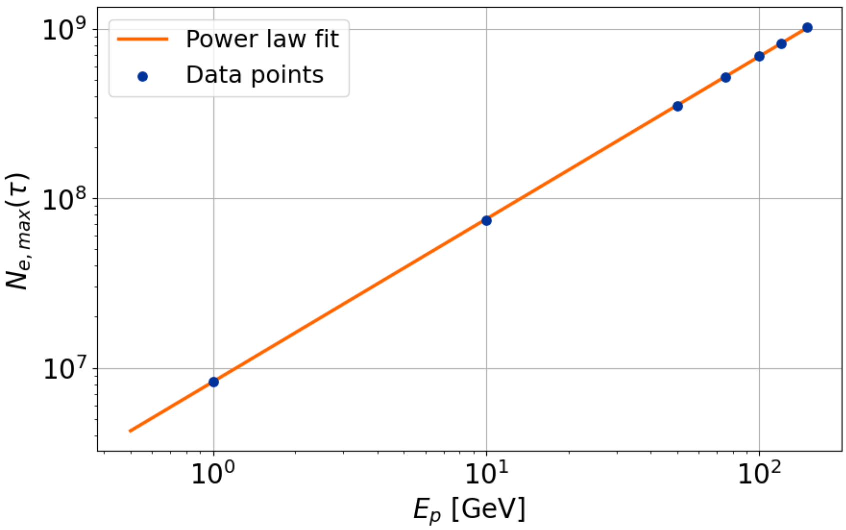

Figure 4.11: A power law fit of the relationship $N_{e,max} \propto (E_p)^{\alpha}$. The fit parameter is α = 0.9596 ± 0.0017, indicating a linear relationship between the two quantities. It is noted that no error bars are added to the data points as they are derived from analytical functions and are regarded to have equal weights in the fit.

same with an increasing lifetime. It is known that the model behind MARES has difficulties with treating small lifetimes and therefore explains the downwards behaviour at lower lifetimes. As the plasma lifetime of the in ice is $\tau \sim 10$ ns[83], this is not considered to be a problem. Hence from the above, it is clear that the power law index changes only slightly when varying the lifetime and hence it can be concluded that there is no correlation between E_p and τ, as expected.

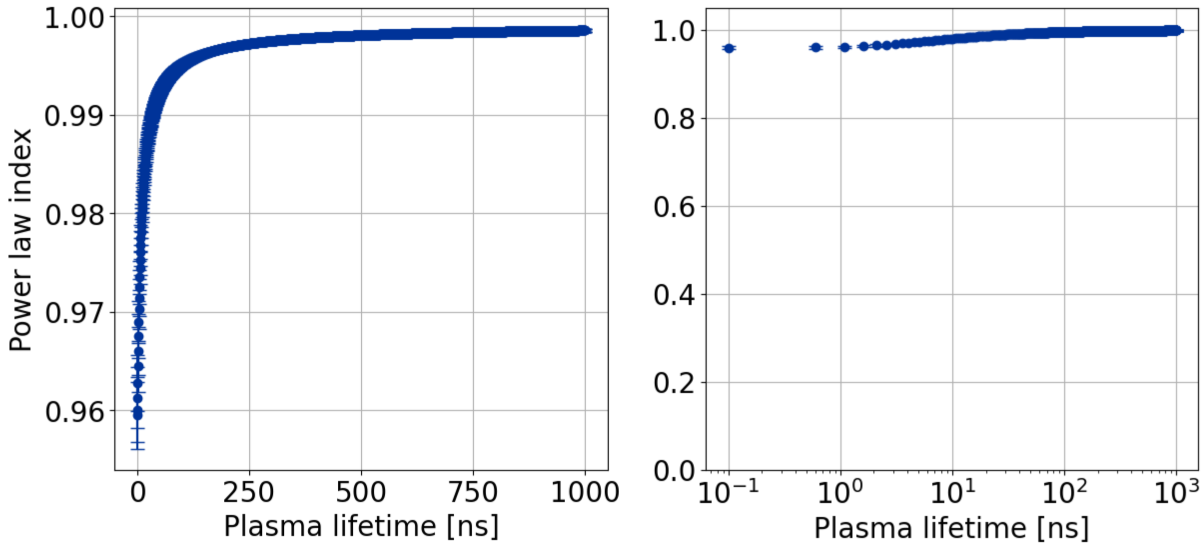

Figure 4.12: The power law index of the $N_{e,max} \propto (E_p)^\alpha$ relation as a function of the plasma lifetime. The left and right panel show the same data but using a different scale on the x-axis. The errorbars in the power law index values are taken from the fit in log-log space.

4.4.3 Primary energy versus peak voltage

In this section it is investigated how the peak voltage observed by the receiver changes as a function of the primary energy of the neutrino. The peak voltage of a waveform is defined as: $V_{\text{RX,peak}} = max(|V|)$, where V is the voltage profile observed by the receiver. In total 2000 simulations are performed each with a different E_p, but with the same fixed cascade direction $(90°, 90°)$ and lifetime $\tau = 10$ ns. The energy values for the 2000 simulations are equally spaced using a log-spacing in the interval $[10^7, 10^9]$ GeV. This specific spacing of the energy was chosen such that the $(V_{\text{RX,peak}}, E_p)$-data points are equally spaced in a log-log space. If their is a relation $V_{\text{RX,peak}} \propto (E_p)^\alpha$ it would transform to a linear relationship between the two quantities in a log-log scale. This would allows to perform a linear fit to find the power law index α

$$\log_{10}(V_{\text{RX,peak}}) = \alpha \log_{10}(E_p) + \beta\,, \tag{4.15}$$

where β is the theoretical peak voltage when $E_p = 0$. As this has no physical meaning, the parameter β is not considered. For each of these 2000 cascades, the waveform is simulated using MARES and subsequently the peak voltage is extracted. A linear fit between the two quantities in a log-log space is performed using Equation (4.15). The result of this fit is shown in Figure 4.13. The fit value for the power law index is found to be $\alpha = 0.96344 \pm 0.00028$ which indicates that the peak voltage scales linear with the primary energy to very good approximation. The uncertainty on α arises from assuming equal weights for every $(V_{\text{RX,peak}}, E_p)$-data point and is the error returned by the χ^2-fit. The linear relationship between the two quantities is a consequence of the simple fact that a larger primary energy leads to more electrons being ionized. Since the electric field observed from a single segment of the cascade scales with the number of electrons, see Equation (4.7), the electric field or voltage is expected to scale linearly with the primary energy.

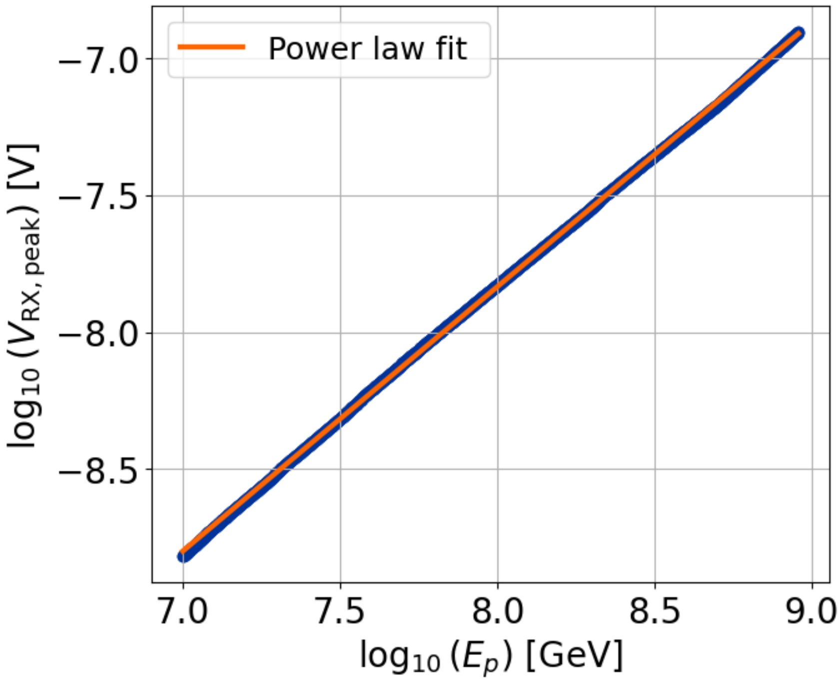

Figure 4.13: The peak voltage as a function of the primary energy of the neutrino. In orange a power law fitted through the the blue data points. The power law index is found to be $\alpha = 0.96344 \pm 0.00028$.

Chapter 5

Investigating radar echo signal properties

As became clear from the previous chapter, the shape of the waveforms, and more generally the properties of the radar echo signal, change depending on for example the plasma lifetime and the cascade direction. These first observations made in [12] formed an invitation to study the signal properties in more detail and are the topic of this chapter. For all the results presented in this section, the simulation parameters in Table 5.1 are kept fixed unless specified otherwise. On top of that, the bistatic radar setup in Figure 4.5 is chosen. As already mentioned, this detector setup allows for an easy interpretation of the zenith angle θ and azimuth angle ϕ parameterizing the direction of the cascade.

Table 5.1: The standard simulation parameter values.

Parameter	Value
$f(TX)$	50 MHz
TX & RX gain	0 db
TX power	1000 W
τ	10 ns
E_p	1 EeV
n_{ice}	1.78
Sampling rate f_s	$100 \times f(TX)$

5.1 Angular plots

After the results shown in Figure 4.6 it became clear that it would be useful to group the information of more than three cascade directions into one plot. This led to the creation of the so-called angular plots. An angular plot is created through the following methodology:

- Fix either the zenith angle or azimuth angle of the cascade.
- Vary the other angle from 0° to 360° with a stepsize of 1° and simulate with MARES the corresponding waveform for all 360 directions.
- Select the peak voltage of the waveform. As the voltage can be negative, first the absolute value is taken of the waveform after which the largest peak is selected. Hence, $V_{\mathrm{RX,peak}} = max(|V|)$.
- Plot the peak voltage as a function of the varying angle and normalise all peak voltages by dividing by the maximal peak voltage of all directions.

Depending on whether the azimuth or zenith angle varies, the angular plot is respectively called an azimuth or zenith plot throughout the rest of this work. Following the roadmap above by keeping the zenith angle fixed at $\theta = 90°$ and varying the azimuth angle yields the azimuth plot shown in Figure 5.1. The polar coordinate in this figure indicates the azimuth angle and the radial coordinate the normalised peak voltage.

Note that these cascade directions correspond with turning the cascade over a full circle in the xy-plane in the reference frame shown in Figure 4.5. As such, the receiver antenna is located in the $\phi = 180°$ direction and the transmitter is sitting right below the xy-plane as indicated in the figure. From the azimuth plot, it becomes clear that a distinct beaming pattern is present which means that some cascade directions lead to a radar echo signal that has a larger peak voltage. Unique signal modulations are observed and are believed to be a consequence of Cherenkov effects, Doppler effects, or perhaps both. Recall that in this work, the Cherenkov effect only refers to the geometrical aspect of the radiation as discussed in Section 3.1.1. The beaming pattern also shows a clear symmetry around the direction pointing to the receiver, $\phi = 180°$. This can be understood as relativistic effects only depend on the relative positions between the cascade direction, transmitter and receiver. On top of that, from the electric field expression in Equation 4.12, it becomes clear that angles mirrored around $\phi = 180°$ have the same R_T and R_R resulting in the same electric field and hence peak voltage. This is confirmed by plotting the individual waveforms for two angles mirrored around $\phi = 180°$ and is show in Figure 5.2.

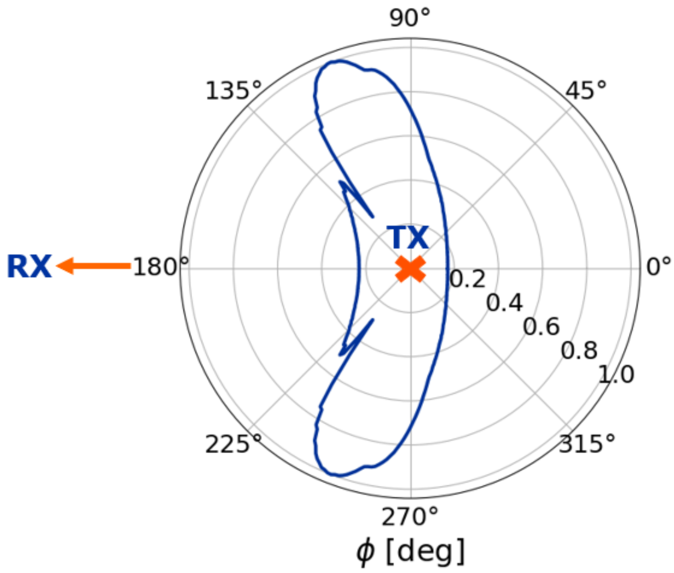

Figure 5.1: An azimuth plot for fixed zenith $\theta = 90°$ and varying ϕ. Recall that the peak voltages are normalised by the maximum of all of them. The arrow pointing towards the receiver indicates its position. The cross indicates the transmitter is sitting beneath. A clear beaming pattern is present.

The shape of the peak voltage profile in Figure 5.1 resembles the radiation pattern of a point particle that travels at relativistic speeds. Recall from Section 3.1.1 that this radiation pattern has a conical shape with an opening angle given by $\cos\theta_c = 1/(\beta n_{ice})$ when traveling at relativistic speeds through a medium. For a relativistic cascade in ice, this implies that the Cherenkov angle is $\theta_c = 55.82°$ where the refractive index of ice in Table 5.1 was used and $\beta \approx 1$. The opening angle of the cone-like shape in Figure 5.1 is the angle between a maximum and the position of the receiver at $\phi = 180°$. Since the maxima are located at $\phi = 111°$ and $\phi = 249°$ the emission peak angle is found the be $\theta_c = 69°$. This is almost 13° wider than the predicted Cherenkov angle. An important fact not considered in this derivation is that all the simulations done in this work consider three bodies: transmitter, receiver, and cascade. Hence, both the receiver and transmitter have their own Cherenkov cone and the actual result observed by the receiver is the complex interplay between both. It is therefore concluded that Cherenkov effects are likely still at play, but non-trivial.

In Figure 5.3 the zenith plot is shown for a fixed azimuth angle $\phi = 90°$. Once again, certain directions are yielding stronger peak voltages. In this specific zenith plot, a clear symmetry around $\theta = 180°$ is seen. This time the symmetry is a consequence of the degeneracy in the cascade directions for any zenith angle above 180°. Any geometry characterised by a cascade direction (θ_i, ϕ_i) is the same for a cascade direction of $(360° - \theta_i, \phi_i + 180°)$. Hence for the rest of this work, the zenith angle is only varied from 0° to 180°.

From both the azimuth and zenith plots, it is clear that the effect of the cascade direction on the signal is quite significant. In order to get a complete understanding of the observed features, it would be ideal to

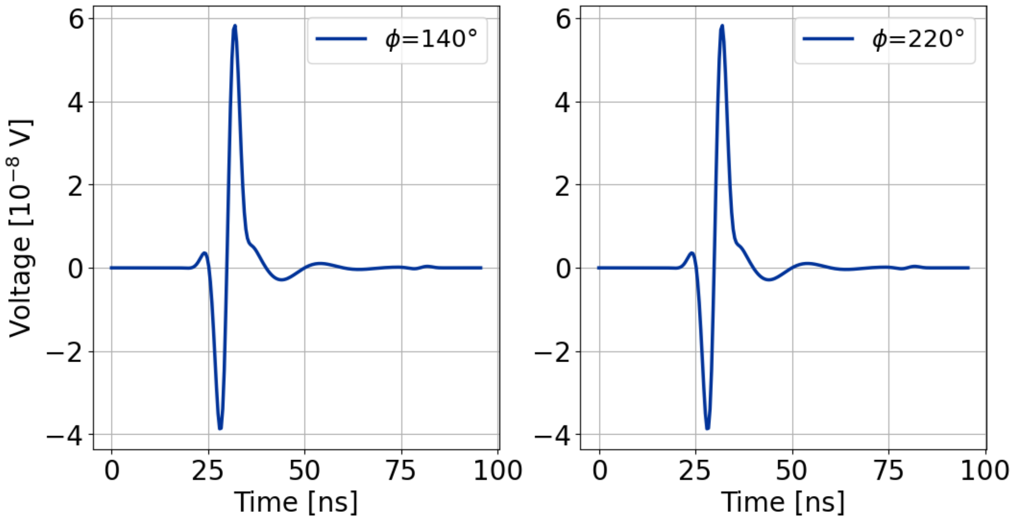

Figure 5.2: The waveforms of for two cascade directions with the same zenith angle θ = 90° and different azimuth angles. A clear symmetry is present on the level of the waveforms.

investigate the peak voltage over the entire phase space or all possible cascade directions. The angular plots alone are limited by the fact that they fix one of the two angles. As such, lots of angular plots would need to be made to get a complete overview of the phase space. An example of such an overview for the azimuth plots can be found in Appendix C. As this is quite inconvenient, a different way of representing the peak voltage is adopted in the next section.

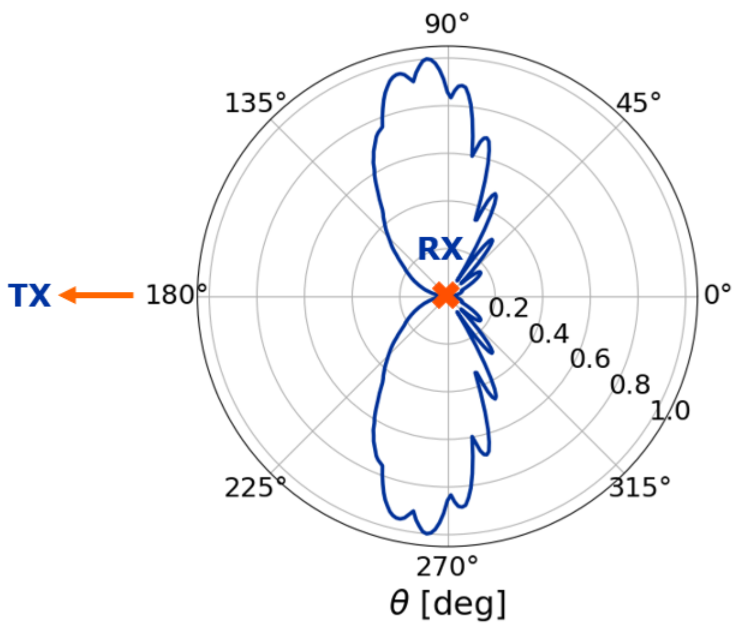

Figure 5.3: A zenith plot for a fixed azimuth angle ϕ = 90°. The arrow pointing towards the transmitter indicates its position. The cross indicates the receiver is sitting beneath.

5.2 2D peak voltage plot

In this section, the entire phase space of the cascade direction is probed at once. This is done by simulating the waveform for each combination of $\theta \in [0°, 180°]$ and $\phi \in [0°, 360°]$ where a stepsize of 1° was chosen for both angles. For each of these waveforms, the peak voltage is selected and plotted as a function of the cascade direction, of which the results are shown in Figure 5.4. This figure is called the 2D peak voltage plot and will be referred to many times in this work. In the figure, the colour map indicates the peak voltage value normalised with respect to the maximum peak voltage and a log scale is taken to increase the visibility of the numerous features. A value of $\log_{10}(V_{RX,peak}) = -3$ implies the peak voltage at the corresponding direction is a thousand times smaller than the maximum peak voltage. By probing the entire phase space in Figure 5.4, three distinct features are revealed:

1. Horizontal bands of alternating higher and lower peak voltage.
2. A high-intensity swirl going from left to right over the entire figure.
3. A low-intensity half ring.

For the rest of this work, the features are named accordingly. Note that with intensity is meant the value of the peak voltage and not the physical quantity itself. The goal for the rest of this work is to identify the physics behind these features, as they are non-trivial. It will become clear that multiple different effects are influencing the radar echo signal at once. Understanding the origin of these features is important as they will help reconstructing the physical parameters of the cascade and the primary neutrino properties. These features are discussed in more detail in designated sections, but first a look at the frequency domain is taken.

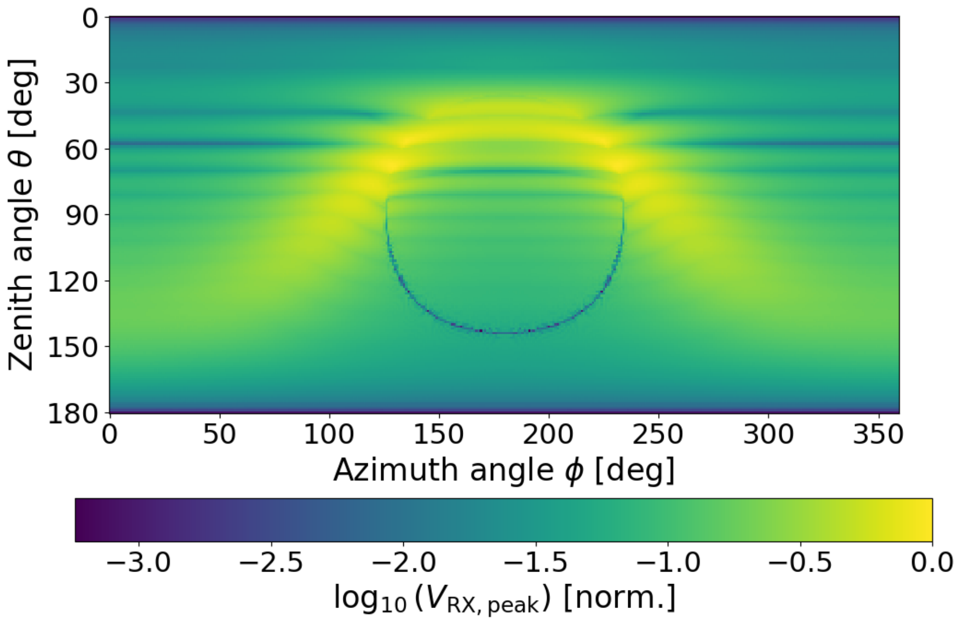

Figure 5.4: The peak voltage for every cascade direction (θ, ϕ) normalised by the maximum. Three distinct features are visible: horizontal bands, a high-intensity swirl and a low-intensity ring.

5.3 Frequency domain

It is strongly believed that both Doppler and Cherenkov effects are crucial in understanding the features in the 2D peak voltage plot. Hence, a frequency domain equivalent of the plot is made. For all the cascade directions, the Fourier Transform (FT) of the waveform is taken and the frequency with the highest peak is selected. The peak frequency is the most dominant in the signal and therefore the most important one. This peak frequency is subsequently plotted as a function of the cascade direction for which the result is shown in Figure 5.5. The colour map is created such that the blue and red colours correspond with respectively a blueshift and redshift. The white colour corresponds with a peak frequency equal to the transmit frequency, $f(TX) = 50$ MHz. From this frequency picture, it becomes clear that Doppler effects are strongly influencing the shape of the waveform and that the features from the 2D peak voltage plot have their counterpart in the frequency domain. In order to better understand why certain cascade directions correspond with either frequency shift, different regions are drawn in Figure 5.5. These regions indicate if the cascade moves towards or away from the transmitter and receiver and are defined by:

1. **A**: Towards RX, away from TX.
2. **B**: Away from RX, away from TX.
3. **C**: Towards RX, towards TX.
4. **D**: Away from RX, Towards TX.

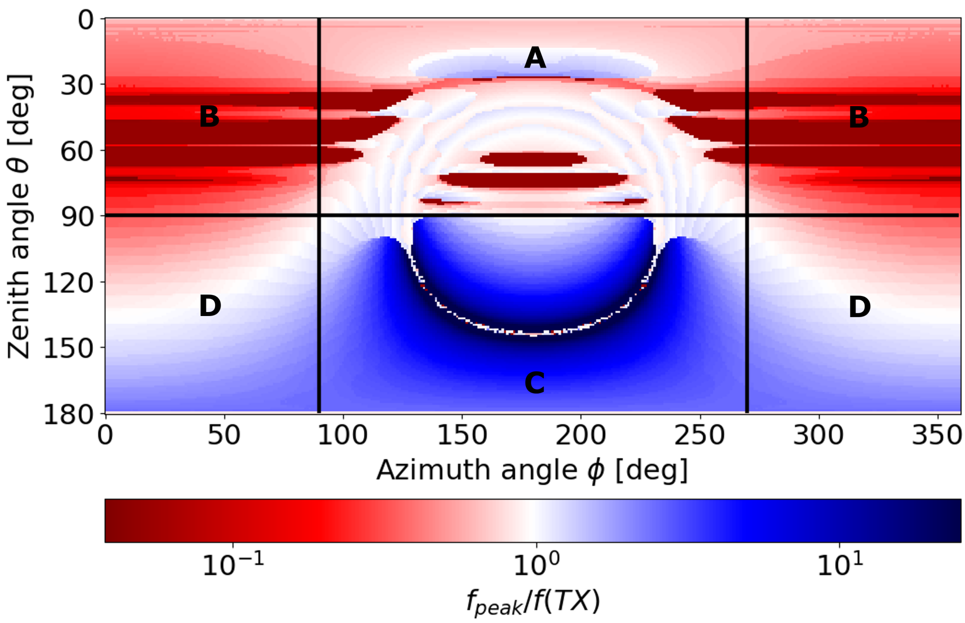

Figure 5.5: The peak frequency in the FT of the waveform as a function of the cascade direction. The different cascade direction regions are indicated by the black lines and the letters.

The strongest blueshifts appear in region C where the cascade moves towards both antennas. In this region, a wide ring of increasing peak frequency is observed at a similar location to the low-intensity ring in the 2D peak voltage plot. This indicates that the feature could correspond with the Cherenkov cone of the three-body system, referred to as the radar Cherenkov cone. Interestingly, at the location of the low-intensity ring the blueshift disappears and almost no shift is found apart for some directions. This observation is not physical but a consequence of the poor sampling of the waveform. At the radar Cherenkov cone, the blueshift could get extremely strong and lead to the peak frequency getting out of range in the FT. This is discussed in more detail in Section 5.4.

In region B, the cascade moves away from both antennas explaining the strong redshift. The dark red regions in the 2D peak frequency plot correspond with cascade directions for which the redshift is so strong that the peak frequency is sitting at a value of 0 MHz. In this regime, the waveforms do not show an oscillating pattern anymore.

In region D, cascade directions with a blueshift, redshift and no shift are all observed. This can be explained as it is the region where the cascade is moving away from the receiver but towards the transmitter.

Due to the three-body nature of the geometry, the observed Doppler effect is the result of the individual Doppler effects from the two antenna-cascade systems. The cascade-TX system will experience a blueshift, while the cascade-RX system will experience a redshift. Both Doppler effects are competing with each other and result in a net Doppler effect observed in Figure 5.5. Hence, it becomes clear that the white regions correspond with geometries where the two Doppler effects cancel out.

In region A, similar conclusions to region D can be made. Still, a more exotic structure is visible in region A. A large band of no frequency shift is observed that seems to mask most of the continuation of the high-frequency ring from region C. Interestingly enough, this region also gives some insight into which cascade-antenna system forms the dominant contribution to the net Doppler effect. In region A, the cascade is moving away from the transmitter but towards the receiver. This would imply that the individual contributions of the two cascade-antenna systems would respectively yield a redshift and blueshift. Besides right above the white band, almost no blueshift is observed implying that the cascade-TX subsystem contributes more dominantly to the net Doppler effect. This can also explain why there are horizontal bands in the 2D peak frequency plot. Changing ϕ but keeping θ fixed, does not change the relative orientation between the transmitter and cascade, hence yielding the same Doppler shift in the cascade-transmitter subsystem. Since this system's contribution is most dominant, a relative constant Doppler shift is observed.

The frequency domain gives some hints regarding the features in the 2D peak voltage plot. More precisely, regarding the origin of the low-intensity ring. Still, the physical nature of the high-intensity swirl and horizontal bands remains unclear. Interestingly enough, the high-intensity swirl coincides with the band of no frequency shift in the 2D peak frequency plot. This observation was an invitation to look at the phase information of the different segments making up the cascade and is the topic of Section 5.5. The horizontal bands in the 2D peak voltage plot resemble a diffraction pattern and will be the topic of Section 5.7

5.4 Low-intensity ring

From the results in the previous section, it was suggested that the low-intensity ring could correspond with the radar Cherenkov cone. In this section, this claim will be supported by changing the refractive index of the ice. First, a more detailed explanation is given on how the radar Cherenkov cone can be observed as a low-intensity instead of a high-intensity ring in the 2D peak voltage plot.

The Cherenkov cone is the optical equivalent of a sonic boom. This implies that a waveform is strongly compressed in a narrow time frame with a strong peak voltage. As such, the radar Cherenkov cone should be observed as a high-intensity ring. Instead, in the 2D peak voltage plot a low-intensity ring is observed. Fortunately, there is a rather straightforward reason why the Cherenkov cone can appear as a low-intensity ring. A continuous wave cannot be treated continuously by a computer. As such, all digital signals are sampled using a certain sampling frequency. This sampling frequency cannot be taken arbitrarily as it can lead to an effect called aliasing. This is also known as the Nyquist theorem [84]. In Appendix D some more details regarding this theorem and its consequences is given.

5.4.1 Aliasing at the low-intensity ring

From the Nyquist theorem, an explanation can be given for the observed low-intensity ring in the 2D peak voltage plot. When simulating the waveforms using MARES, the sampling rate can be set. When no Doppler effects are taken into account, the scattered signal observed by the receiver has a peak frequency at $f(TX) =$ 50 MHz. As became clear from the previous section, Doppler effects are ubiquitous causing the dominant frequency to shift. As such, it is important to choose a sampling frequency that satisfies the Nyquist condition in Equation (D.1) to correctly represent the signal. The sampling frequency in all simulations is kept fixed to a standard value shown in Table 5.1 of 5 GHz. This means that all signals with a frequency below 2.5 GHz are sampled correctly and no aliasing occurs. The waveforms for cascade directions on the ring shift to frequencies above the Nyquist frequency and will be simulated incorrectly due to aliasing. As such they fall out of range in the FT and the transmit frequency is observed instead, as seen in Figure 5.5. This is also observed when looking at the actual waveform for a direction on the low-intensity ring, for example, (143°, 169°). The waveforms for this direction are shown in Figure 5.6 where two different sampling rates are taken. In Figure 5.6a a 5 GHz sampling rate is used and a small peak voltage of $\sim 2\times10^{-10}$ V is observed. On top of that, the signal extends over a long period. Increasing the sampling rate tenfold, in Figure 5.6b, the waveform changes drastically both in shape and strength. The peak voltage rises with two orders of magnitude and the signal shape becomes more pulse- or chirp-like. This illustrates that the standard sampling rate in Figure 5.6a is not sufficiently high enough to correctly represent the signal.

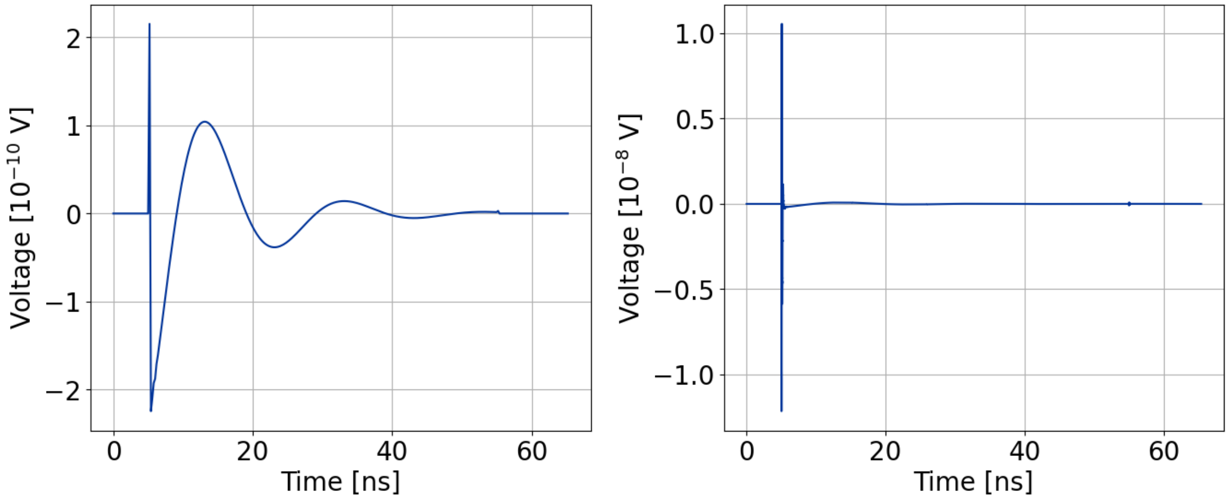

(a) (b)

Figure 5.6: The waveforms for a cascade propagating in the direction (143°, 169°) for (a) a sampling rate of 5 GHz and (b) a sampling rate of 50 GHz. Notice the different units on the y-axis for the two waveforms.

To verify that increasing the sampling rate results in higher peak voltages for the entire low-intensity ring, simulations are run with a 50 GHz sampling frequency for part of the phase space. The result is shown in Figure 5.7, from which it becomes clear that the ring still appears as a low-intensity ring, but the contrast between the maximum and the ring decreased from a factor 10^{-3} to $10^{-1.75}$. The sampling rate should be increased even more in order to have no aliasing in the waveforms of the low-intensity ring. Hence, from all of the above, it can be concluded that the low-intensity ring only appears to be of small intensity but in reality, corresponds with directions of very short and sharp waveforms with strong peak voltages. This result supports the claim that the ring corresponds with the radar Cherenkov cone. Increasing the sampling rate would only increase the simulation time with not much gain in physical accuracy and therefore the standard sampling rate in Table 5.1 is chosen for the remainder of this work.

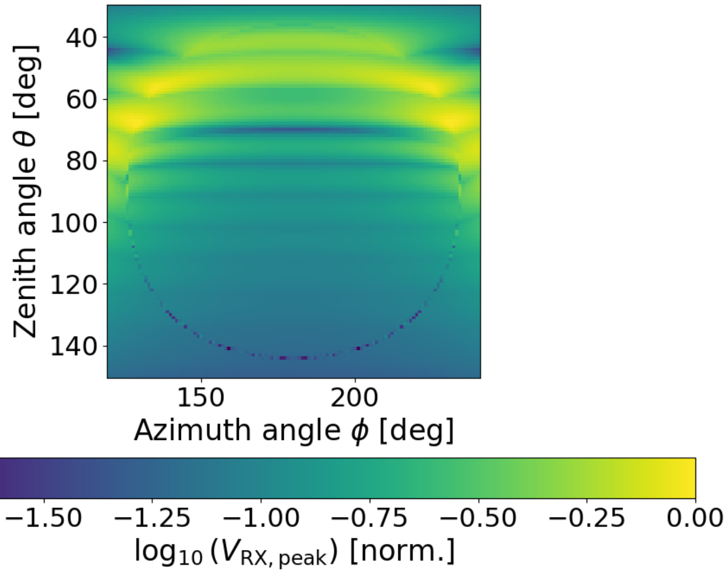

Figure 5.7: The peak voltage plot for a part of the entire phase space. The sampling rate is increased tenfold with respect to the result in the standard 2D peak voltage plot.

5.4.2 Changing the refractive index

The most compelling evidence that the low-intensity ring is in fact corresponding with the radar Cherenkov cone is found when changing the refractive index of the ice in MARES. From Equation (3.1), it becomes clear that the opening angle of the Cherenkov cone increase with an increasing refractive index and is zero when $n = 1$. Indeed, if the low-intensity ring originates completely from a Cherenkov effect, it should disappear when $n = 1$. This was verified using MARES. Once again simulations for the entire phase space of cascade direction were performed using the values for the simulation parameters in Table 5.1, apart from the refractive index that was changed to $n = 1$. The result is shown in Figure 5.8. The low-intensity ring has completely disappeared while the other two features remain. This does not only prove that the low-intensity ring corresponds with the radar Cherenkov cone, but that the other two features have a different origin.

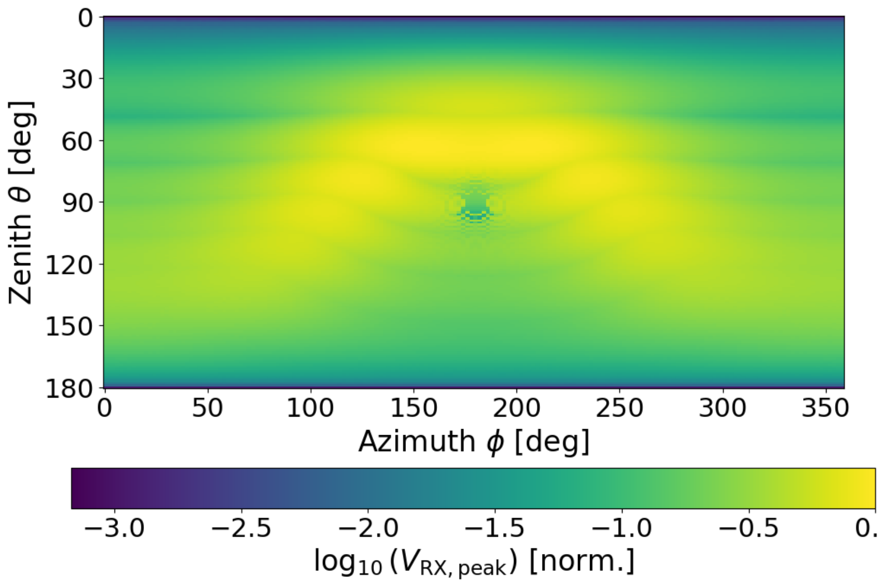

Figure 5.8: The 2D peak voltage plot for a refractive index set to $n = 1$.

5.4.3 Measurement of the radar Cherenkov cone

It is verified that the observed radar Cherenkov angle, corresponding with the low-intensity ring, in the 2D peak voltage plot in Figure 5.4 is equal to the predicted Cherenkov angle, $\theta_c = 55.82°$. In order to determine the angle, two lines are drawn in the 2D peak voltage plot. One horizontal line for a constant zenith angle $\theta = 90°$ and one vertical line for a constant azimuth angle $\phi = 180°$. The intersection between the two lines corresponds with the direction pointing towards the receiver. The radar Cherenkov angle is determined from the difference between the position of the receiver and an intersection point between the lines and the low-intensity ring. For all of the points, the radar Cherenkov angle is found to be $\theta_c \sim 54°$. This is close to the predicted angle, $\theta_c = 55.82°$, given by Equation (3.1). The small deviation can be a consequence of the 1° resolution used in the simulations of the cascade directions for both the azimuth and zenith angle. Increasing this resolution will lead to a more resolved low-intensity ring. On top of that, from Figure 5.7, it is clear that increasing the sampling rate also leads to a higher resolution for the low-intensity ring.

It should be noted that the value found in this section for the radar Cherenkov angle is not the same as found previously from the azimuth plot in Section 5.1. From the azimuth plot, it was concluded that the radar Cherenkov angle is 13° larger than the prediction. The radar Cherenkov angle was determined by determining the maximum value in the azimuth plot and calculating the difference between the corresponding angle and $\phi = 180°$, the direction of the receiver. As became clear from the above, at the Cherenkov cone, the waveforms are typically undersampled due to the large blueshift in the frequency. Hence, aliasing occurs and the signal is not represented correctly, actually leading to a smaller peak voltage. This effect also influences the shape of the beaming pattern in the azimuth plot in Figure 5.1. It is therefore not necessarily correct to determine the Cherenkov cone from the maximum in this figure and the sampling rate is increased to see which directions will change in peak voltage. The result is shown in Figure 5.9 from which it is deduced that close around the angles $\phi = 126°$ and $\phi = 234°$ the peak voltage has increased. This indicates that the Cherenkov angle should be determined from these directions and not the ones corresponding with the maximum in the results sampled at 5 GHz. Hence, the observed radar Cherenkov angle is $\sim 54°$ being much closer to the prediction than the value from Section 5.1. This is also consistent with the value found in the 2D peak voltage plot.

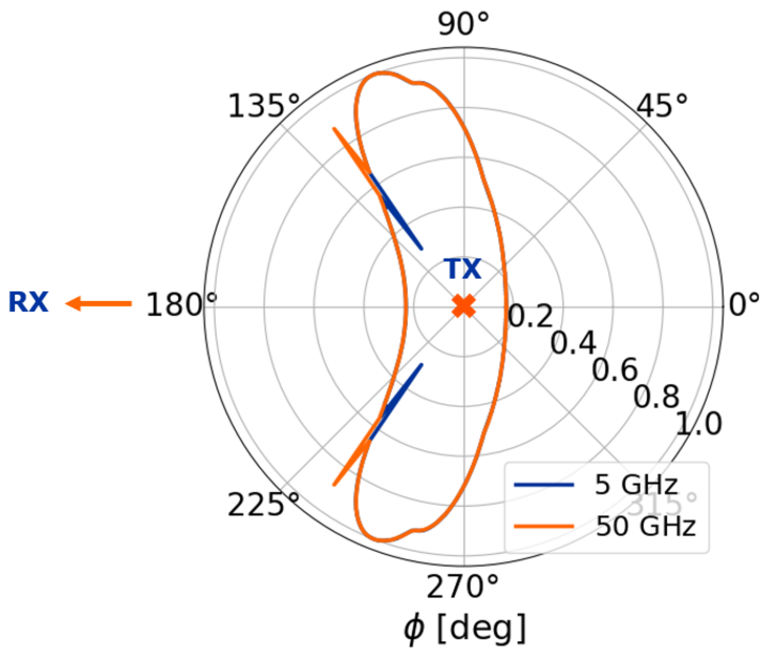

Figure 5.9: The azimuth plot for a fixed zenith angle $\theta = 90°$ for two different sampling rates. The blue curve uses the standard sampling rate from Table 5.1. For the orange curve, the sampling rate was increased by a factor of 10.

5.5 High-intensity swirl

From the 2D peak frequency plot in Figure 5.5 it was discovered that the high-intensity swirl in the 2D peak voltage plot coincides with peak frequencies at the transmit frequency. This indicated that the Doppler shifts between the cascade-TX and cascade-RX systems cancel each other. In order to be able to observe a high-intensity swirl in those cascade directions, a certain mechanism should exist that boosts the strength and peak voltage of the waveform. The electric field observed at the receiver is the superposition of the electric field emitted by the different segments of the ionization trail. If the segments are emitting coherently, the signal at the receiver becomes strong as the observed power would scale with M^2 where M is the number of segments. Coherent emission from these segments could form a natural explanation for the swirl and is investigated in this section.

MARES cannot only simulate the waveforms of the scatter but also track the phase information in the ionization trail throughout its entire existence. An example of this evolution is shown in Figure 5.10 for a cascade propagation in the $(90°, 90°)$ direction. The colour map shows the phase profile observed by the receiver as a function of the time and ionization trail position. The x-axis plots the time kept by the receiver. On the y-axis the ionization trail position observed by the transmitter is plotted and is expressed in units of time since the cascade travels at the speed of light in vacuum: $L = ct'$. The segmentation of the cascade happens with respect to the transmitter, as explained in Appendix A, and is the reason why the length of the cascade is plotted from that point of view. The colour map shows the $\cos(\varphi)$ where φ is the phase of the electric field as defined in Section 4.2. In the left panel, the electron density profile is plotted to illustrate the amount of electrons in each corresponding segment. Some remarks can be made from this figure. The observed lifetime of a single segment experiences time dilation and is not equal to the standard value $\tau = 10$ ns, set in the simulation. This can be deduced from the segment at $ct' = 0$ m. The segment is created at $t = 5$ ns and recombines again at $t = 55$ ns yielding a total observed lifetime $\tau = 50$ ns. This is once again a manifestation of the relativistic effects at play.

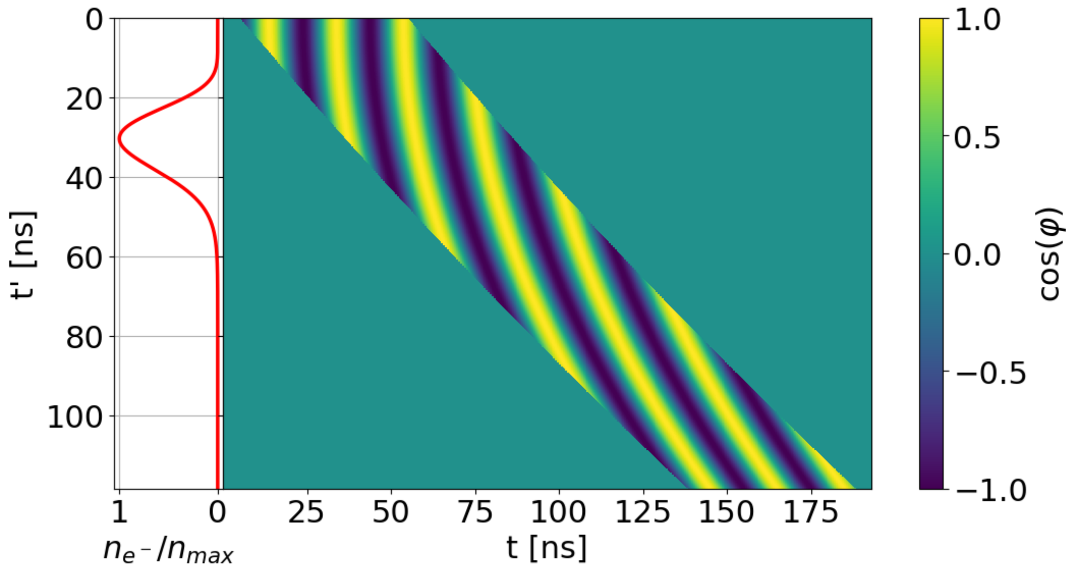

Figure 5.10: *Right panel*: The phase profile observed by the receiver for a cascade travelling in the $(90°, 90°)$ direction. *Left panel:* The longitudinal electron density profile.

By taking vertical slices in Figure 5.10, the phase profile over the entire length of the cascade at a fixed instance in time can be investigated. Repeating this at multiple different times t shows that the phase profile is dynamic and changes quite strongly during the entire event. For the example in Figure 5.10, at the early stages of the ionization trail development, most segments have similar phases. This leads to constructive interference with a strong coherent signal as a consequence. Later on in the development, for example at $t = 100$ ns, the phase values of the different segments are oscillating more. Hence, destructive interference will occur leading to a decoherent weak signal. One important fact not taken into account in the discussion so far is the number of electrons alive in each segment at the chosen time. If more electrons are alive in the ionization trail at one instance of time in comparison to another moment with a comparable phase profile, the former will lead to a stronger signal than the latter because more scatters are present. It is therefore important to include the electron density profile when talking about the phase profile of the trail at a fixed time.

The objective of this section is to find an explanation for the high-intensity swirl. The phase profiles of the cascade directions of the swirl are investigated in the pursuit of that goal. The 2D peak voltage plot is a snapshot of each waveform at the time the peak voltage is reached. The phase profile of the ionization trail is investigated at that same time to investigate if there is a correlation between the two quantities. Multiple different steps are needed to construct the phase profile for a certain cascade direction at the time of the peak voltage. The reduction is explained below for the specific cascade direction $(90°, 90°)$, but can be applied completely analogous to any other direction.

The 2D phase profile is simulated using MARES yielding the result shown in Figure 5.10. The waveform for that same direction is simulated as well and the time at which the peak voltage is reached is derived from it. This time is used to take a vertical slice out of the 2D phase profile and yields the phase information at the moment of the peak voltage. Besides the phase profile, the electron density profile should also be known at the time of the peak voltage. Using MARES, the electron density profile is simulated and yields the result shown in Figure 4.2. Recall that the density profile returned by MARES gives the total amount of electrons in each segment at the moment it is created. Hence, at the time of the peak voltage not necessarily all of these segments are alive yet and for the ones that are, the electron density can have decreased due to the finite lifetime of the electrons. On top of that, the electron density profile is two-dimensional while the phase profile is only given for the longitudinal dimension of the cascade. For the phase profile, it is assumed that all the elements along the radial dimension are coherent. This is a relatively good approximation since the radial dimension of the cascade is typically two orders of magnitude smaller than the longitudinal dimension. As such, the electron density profile must be summed radially to obtain the one-dimensional profile along the longitudinal dimension of the ionization trail. The result of this procedure is shown in Figure 5.11 and is in fact the same as shown in the left panel in Figure 5.10. From this figure, it becomes clear that the bulk of the ionization electrons is concentrated between 5 m and 15 m away from the vertex. The one-dimensional

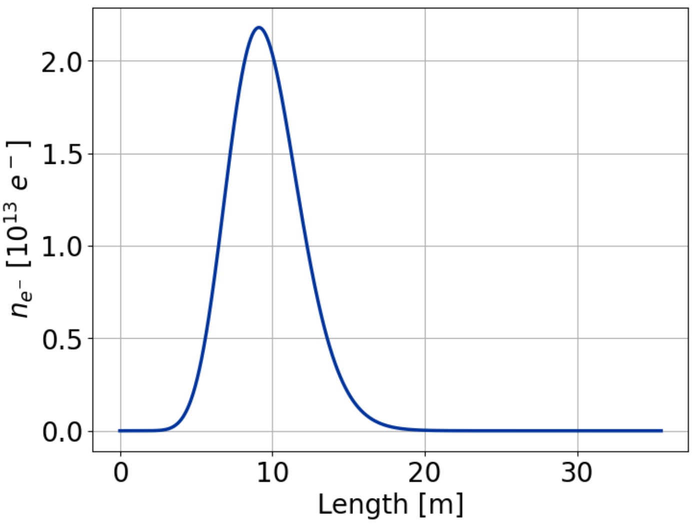

Figure 5.11: The one-dimensional electron density profile representing the amount of electrons in each cascade segment at the moment of creation t_0.

electron density profile is subsequently weighted by a time-dependent factor that takes into account the finite lifetime of the electrons in each segment and the fact that not all segments are created at the same time. This weighting procedure is given by

$$N_i(t, t_0) = N_{0,i}\, e^{-\frac{t-t_0}{\tau}}\, \Theta(t - t_0)\ , \tag{5.1}$$

where $N_{0,i}$ is the value from the one-dimensional electron density profile, t the time at the peak voltage, $\Theta(t)$ the Heaviside function and t_0 is the time when the segment is created. The creation time t_0 for each segment can be found by looking at the lower edge of the band in the 2D phase profile plot in Figure 5.10. Finally, all the necessary steps have been completed to produce the result shown in Figure 5.12. In this figure, both the one-dimensional electron density profile and the phase profile are shown at the time of the peak voltage. By combining the information from both graphs, a conclusion can be made about the phase coherence in the ionization trail for this specific cascade direction. As already mentioned, the segments containing more electrons have a more dominant influence on the observed waveform by the receiver as they simply contain more scattering particles. Hence, it is clear that the phase information between 5 m and 9 m is contributing and the dominant contribution arises from the region around 8 m. Since the phase value only changes slightly over this length range, it can be concluded that a rather strong phase coherence is observed for the direction $(90°, 90°)$. Looking at the 2D peak frequency plot, this direction is sitting at the edge of the high-intensity swirl. This gives a first indication that the origin behind the high-intensity swirl could potentially arise from phase coherence inside the ionization trail leading to an amplification of the signal.

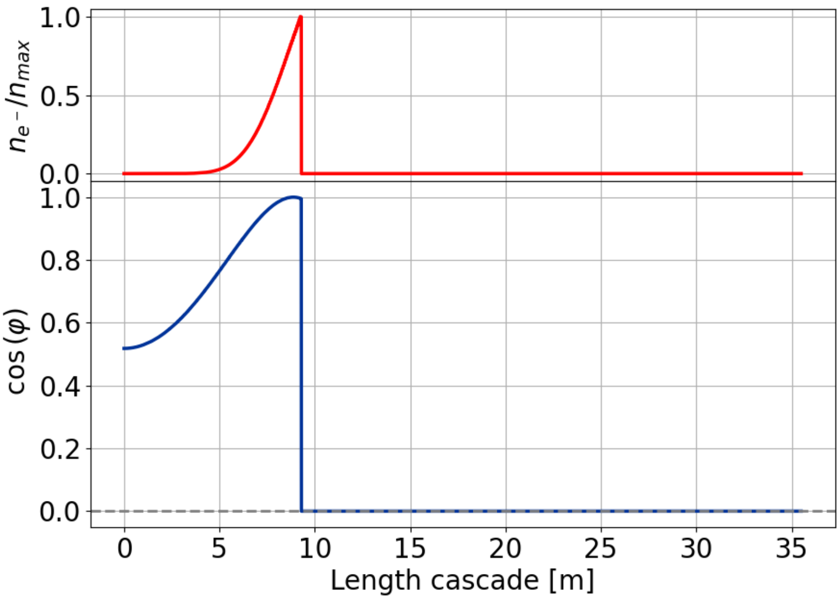

Figure 5.12: *Top panel*: The one-dimensional electron density profile at the time of the peak voltage. The profile is normalised by dividing by the maximum number of electrons in a segment n_{max}. *Bottom panel*: The phase profile of the ionization trail at the time of the peak voltage. The cascade direction in this figure is $(90°, 90°)$.

The phase profile of the ionization trail is investigated using the procedure above for different cascade directions on the swirl. The results for four different cascade directions are shown in Figure 5.13. From these figures, it is concluded that the time when the peak voltage is reached changes depending on the cascade direction. For the cascade direction $(40°, 180°)$, the peak voltage is reached at a later stage since the start of the electron profile shows a discontinuity indicating that the earliest produced ionization electrons have already recombined. The other cascade directions show an opposite behaviour in their electron density profiles, indicating that the peak voltage is reached at an earlier stage in the development of the ionization trail. The direction $(125°, 70°)$ is the least developed at the peak voltage since its electron density profile is strongly peaked at the maximum, indicating that the trail is still developing towards its maximum. The other two remaining directions show a clear curvature at their maximum indicating that the maximum has been reached, for direction $(68°, 125°)$, or is about to be reached, for direction $(90°, 105°)$. As already mentioned, two requirements need to be satisfied to have a what is called a strong phase coherence. First, around the ionization trail maximum, the segments containing most of the scattering electrons are alive resulting in more reflection of the radio signal from the transmitter and as such, a larger observed voltage. Second, if there is strong

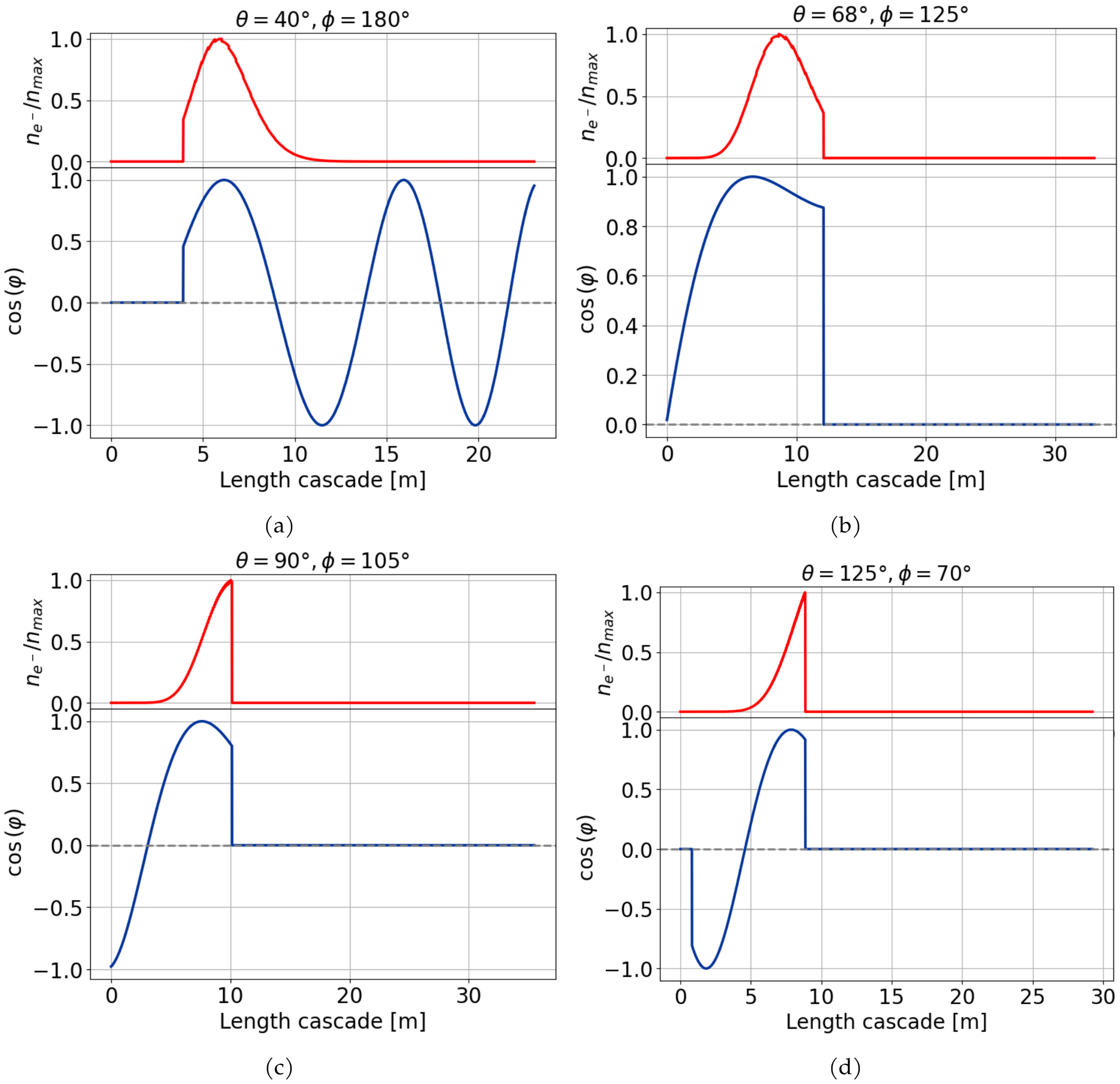

Figure 5.13: Figures illustrating the different behaviour of the phase profile and electron density at the time of the peak voltage for four cascade directions located on the high-intensity swirl.

phase coherence between the different segments of the ionization trail, constructive interference arises and leads to a high observed voltage. Hence, the time when the peak voltage is reached occurs when the two requirements are optimized with respect to each other. For the direction (40°, 180°), these requirements are satisfied at a later observation time than the other three directions because of a relativistic effect. As the ionization trail is typically moving at the speed of light in vacuum and the scattered signal only at the local speed of light in ice, radio waves emitted from the cascade front can reach the receiver before waves from the tail of the cascade even though the latter were emitted at an earlier time. This leads to a situation where the chronological development of the trail is reversed from the point of view of the receiver resulting in a delayed observation of the peak voltage.

Looking at the phase profiles for the four different directions in Figure 5.13 reveals that they can be rather different. For the direction (40°, 180°), the phase profile oscillates quite strongly over the length of the cascade indicating that there is decoherence between the different segments. If the ionization trail would have a uniform electron density over its entire length, it would be concluded that this direction should lead to a faint signal and a low phase coherence. As the electron density profile is far from being uniform, it is only

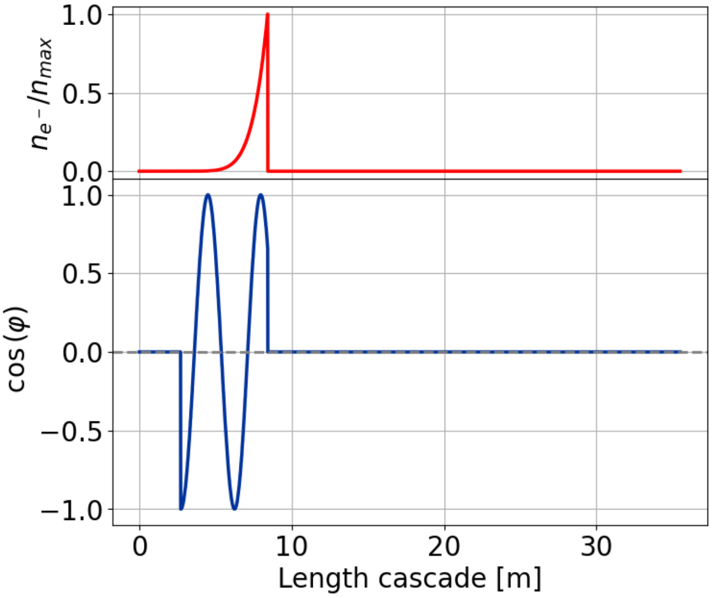

Figure 5.14: *Top panel*: The one-dimensional electron density profile at the time of the peak voltage. *Bottom panel*: The phase profile of the ionization trail at the time of the peak voltage. The cascade direction in this figure is $(90°, 25°)$.

important that the segments with the most electrons in them have similar phases. Looking at the phase values in the region of most electrons, between 5 m and 7.5 m, reveals that the phase signal only changes slowly. As such, there is still a rather significant phase coherence between the dominant segments in the ionization trail. Similar reasoning can be used to interpret the phase profiles for the other three directions and conclude that these also show a rather strong phase coherence. As the cascade direction $(68°, 125°)$ shows the flattest phase profile and has a mature ionization trail development, it corresponds with the highest phase coherence at the time of the peak voltage.

It is also verified how the phase profile looks for a cascade direction not located on the high-intensity swirl. In Figure 5.14 the phase profile and electron density are shown for the direction $(90°, 25°)$. From this figure it becomes clear that the phase profile is rapidly oscillating, and the cascade is not strongly developed at the time of the peak voltage. This shows that small phase coherence is observed for a cascade direction outside of the high-intensity swirl. It is noted that also for the cascade direction $(40°, 180°)$ on the swirl, an oscillating profile was observed. Still, comparing both cascade directions, it becomes clear the the profile for the $(90°, 25°)$ direction is more rapidly oscillating and the cascade is less developed. As such, the phase coherence for this direction is smaller.

From the discussion in this section, it becomes clear that there is a correlation between the phase coherence inside the ionization trail and the peak voltage: a larger phase coherence corresponds with a stronger peak voltage. This can be understood as a strong phase coherence between the segments leads to an enhancement of the radar signal and a larger peak voltage as a consequence. Following this statement explains why the cascade direction $(68°, 125°)$ has the largest peak voltage out of the five selected directions and gives a natural explanation for the origin of the high-intensity swirl.

5.6 Parametrization of the phase coherence

From the above qualitative discussion about the phase coherence inside the ionization trail, it became clear that it is a favourable explanation for the origin of the high-intensity swirl. In this section, a parametrization is developed representing the amount of phase coherence in the ionization trail at the time of the peak voltage. This allows for making a more quantitative comparison between the peak voltage and the phase coherence to deliver more conclusive evidence for the origin of the high-intensity swirl and the general morphology of the 2D peak voltage plot. In total, three different definitions of the phase coherence C will be discussed of which only the latter will turn out the be a useful one.

5.6.1 Definition 1

The first definition of phase coherence is based on the derivative of the phase profile. When the phase profile for a certain cascade direction is perfectly flat, all the segments inside the ionization trail have the same phase leading to perfect constructive interference and a large phase coherence. On the other hand, when the phase profile is oscillating, strong destructive interference arises and the result is a small phase coherence. The derivative of a curve indicates how fast it changes over an infinitesimal displacement. As such, the derivative of the phase profile naturally contains information about the phase coherence of the ionization trail. Weighting the absolute value of the derivative of the phase with the electron density profile thus forms a measure for the phase coherence. This weighting procedure ensures that the contribution of the segments with more electrons in them is larger, as previously discussed. From the weighted derivative profile, a quantitative value can be calculated that represents the amount of phase coherence in the cascade C. This value is defined by the integral of the weighted derivative profile. If the area beneath the curve is large, it means that the original phase profile was rapidly oscillating and thus little phase coherence is present. For a small area beneath the curve, the exact opposite is true. Hence, by defining C as

$$C = \left(\int \left| \frac{d \cos \varphi}{dl} \right| \cdot \frac{n_{e^-}}{n_{max}} dl \right)^{-1} \tag{5.2}$$

a large value corresponds with strong phase coherence. The absolute value of the derivative was taken to ensure that a rapid oscillating phase profile, having both positive and negative derivatives, does not lead to a total area of zero beneath the curve. This would lead to a large phase coherence value while the signal is decoherent. In Figure 5.15, a summary is given of the electron density profile, the phase and the weighted derivative of the phase for a cascade moving in the $(90°, 90°)$ direction. The phase coherence value for this cascade direction is $C = 1740$. From the definition in Equation (5.2) it is found that $C = +\infty$ corresponds with having an original phase profile that is flat and perfect constructive interference between the trail segments. The C-value found above thus indicates rather strong phase coherence. The secondary peak in the weighted derivative profile in Figure 5.15 seems unnatural at first sight. By zooming in on the region between 8 m and 10 m in the phase profile, it became clear that the curve started to decrease again before the abrupt end of the ionization trail was reached. This results in a small derivative that gets increased drastically by the weighting procedure as the electron density reaches maximum at the corresponding length interval.

The goal of the parametrization of the phase coherence is to have a quantity to compare with the peak voltage. A visual representation of this comparison is done through the use of angular plots. C is calculated for cascade directions with a fixed zenith angle $\theta = 90°$ and a varying azimuth angle $\phi \in [0°, 360°]$ with a $1°$ step size. This allows for constructing the azimuth plot in Figure 5.16 where the peak voltage is shown in orange and the phase coherence in blue. Just as in Section 5.1, the peak voltage is normalised by dividing by the maximum peak voltage of all 360 directions. The same normalisation procedure is applied to C in order to be able to plot the two quantities in the same figure. If the two quantities are correlated, it is expected that C has a similar shape as the peak voltage. From Figure 5.16, it seems that this is not the case. This observation can imply two things. Either there is no correlation between C and the peak voltage or the definition of C is incorrect. Since from Section 5.5 it was found that there is a clear link between the two quantities, the latter case is believed and some additional investigation is conducted on the correctness of the definition. The first possible source of instability in this definition arises from the fact that $C \to +\infty$ when the phase profile becomes flat. Hence, if there is a single direction where this divergence starts to happen, it will have a C-value substantially larger than all other directions. If all the other directions are divided by this large C-value, the normalised values become small leading to a very narrowed profile around the maximum as observed in Figure 5.16. Still, this does not explain why the maximum of C does not coincide with the maximum of the peak voltage.

The reason behind this discrepancy is rather subtle. To explain this, two artificial phase profiles are constructed that are both flat but are different in length. A different length means that the time when the peak voltage is reached happens at different moments in the development of the cascade and yields different electron density profiles. The toy phase profiles and their electron densities are shown in Figure 5.17. Applying

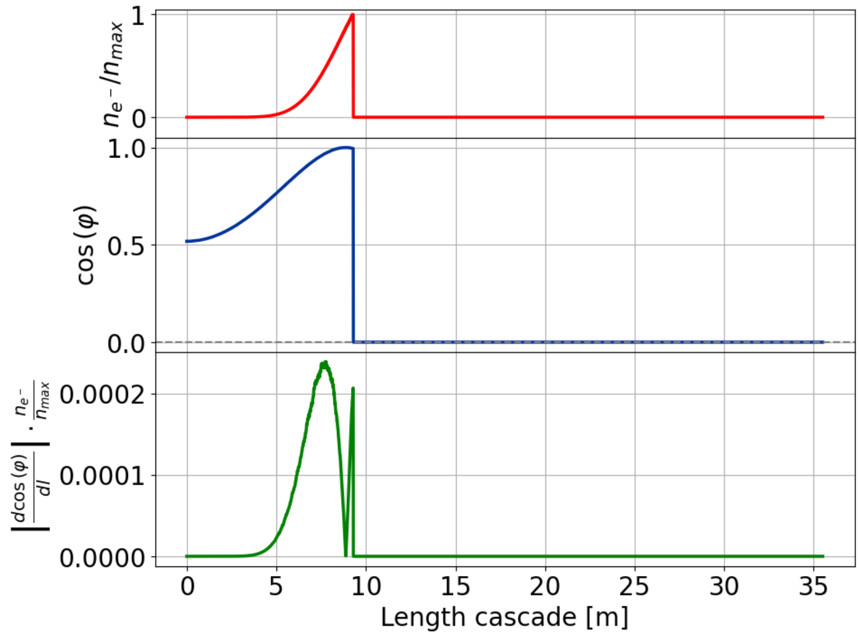

Figure 5.15: *Top panel*: The one-dimensional electron density profile at the time of the peak voltage. *Middle panel*: The phase profile of the ionization trail at the time of the peak voltage. *Bottom panel*: The derivative of the phase profile weighted by the electron density. The cascade direction is $(90°, 90°)$.

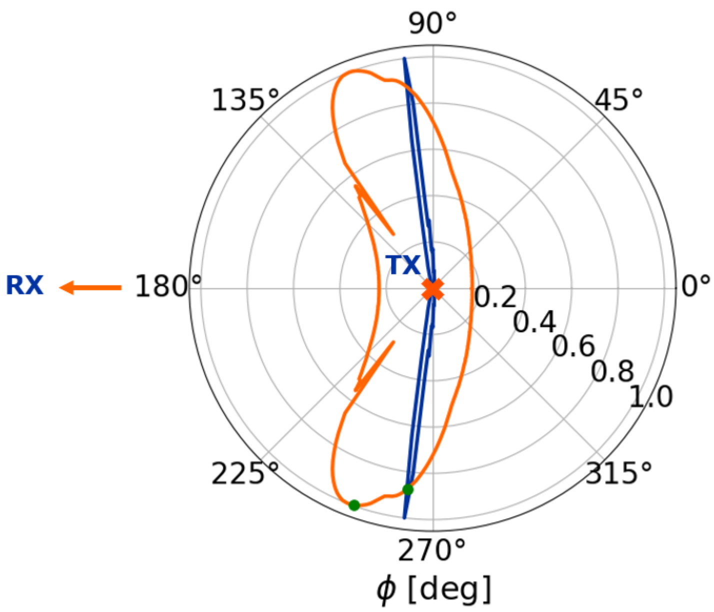

Figure 5.16: An angular plot showing the peak voltage and phase coherence as a function of the azimuth angle for a fixed zenith angle $\theta = 90$. In blue the phase coherence C defined in Equation (5.2) and in orange the peak voltage. The two green dots, $\phi = 263°$ and $\phi = 250°$, indicate directions corresponding to a situation where the definition fails.

the definition for C in Equation (5.2), the derivative of both profiles must be calculated. It is clear this will be a constant function equal to zero over the entire length of the living ionization trail for both profiles. Hence, $C = +\infty$ for both situations and there is no way of making a distinction between the two situations from the value of C. This is not well-defined as a more developed cascade with perfect constructive interference should lead to a larger value of the phase coherence. Due to the zero derivative of the profile, sensitivity to the development of the cascade is lost. Since in either situation, there is perfect constructive interference between the segments, the right panel in Figure 5.17 is expected to have a larger peak voltage as more segments are alive in comparison to the left panel.

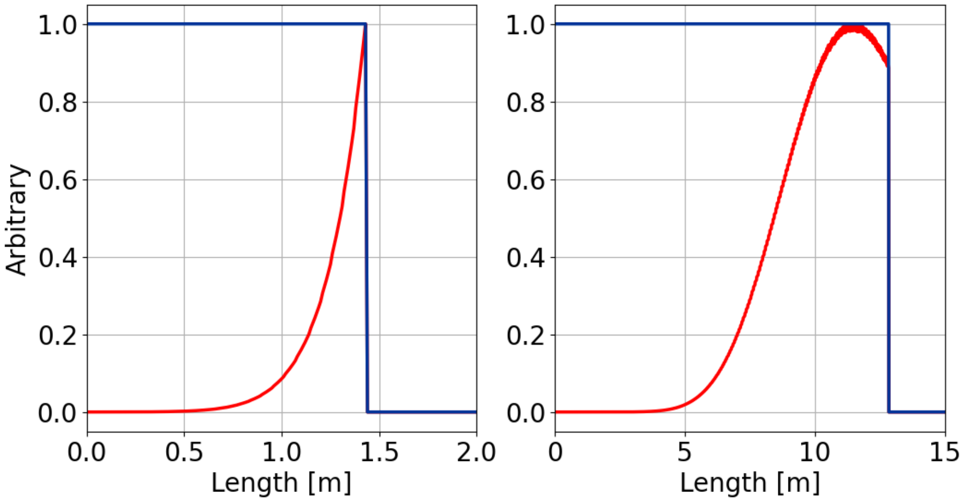

Figure 5.17: Two artificially created flat phase profiles (blue) and their electron density profile (red) for a different peak voltage time.

There is a second situation in which this definition can fail. Instead of having two situations with a flat phase profile, one of them slightly decreases monotonically over the entire length of the living ionization trail. This situation is sketched in Figure 5.18. The flat profile's peak voltage time is earlier than the monotonically decreasing one. The flat profile will have $C = +\infty$ independent of its length. The monotonically decreasing profile will have a rather large C as the phase only varies slowly. Still, the peak voltage of the situation with the monotonically decreasing phase profile may be larger than the flat phase profile. The cascade is much more developed and in the dominant region in the electron density profile, almost perfect constructive interference is present. The combination of the two can lead to a stronger signal and a larger C-value than a short cascade with perfect constructive interference. An actual real example of this situation is found for cascade directions

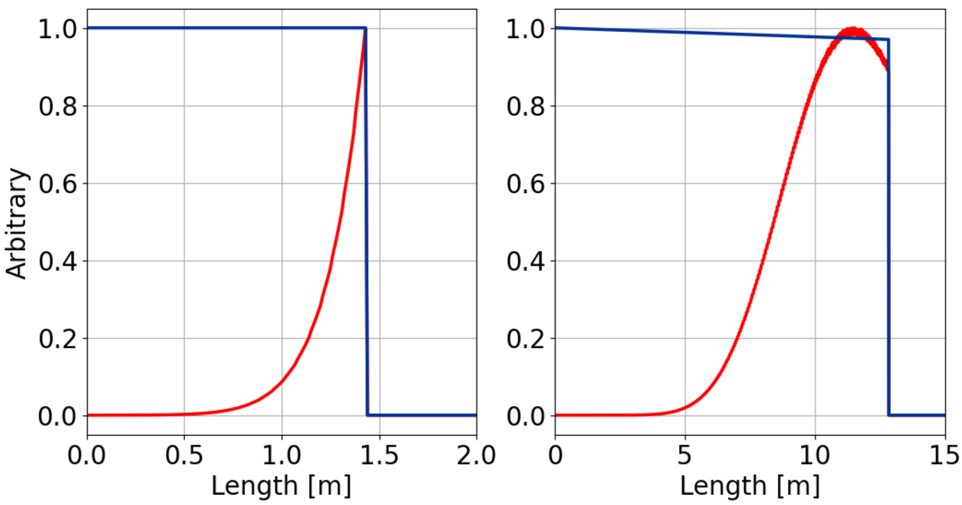

Figure 5.18: Two artificially created phase profiles (blue) and their electron density profile (red). The right panel shows a slight decrease in the phase profile, but due to its stronger development, can have a similar if not a larger C than the flat profile on the left.

(90°, 263°) and (90°, 249°) indicated by the green dots in Figure 5.16. The ϕ = 263° has the largest C value but not peak voltage. The direction with ϕ = 249° has the largest peak voltage. Looking at the phase and electron density profiles for both directions, shown in Figure 5.19, reveals that the ϕ = 263° has an almost flat phase but a less developed cascade than the ϕ = 249° direction. The phase profile of the latter is only slowly varying in the dominant region around the maximum of the electron density. Hence, a similar situation has presented itself as shown in the toy model in Figure 5.18. It can therefore be concluded that having $C = +\infty$ for flat phase profiles makes the definition unstable as it can be insensitive for the developed of the ionization trail.

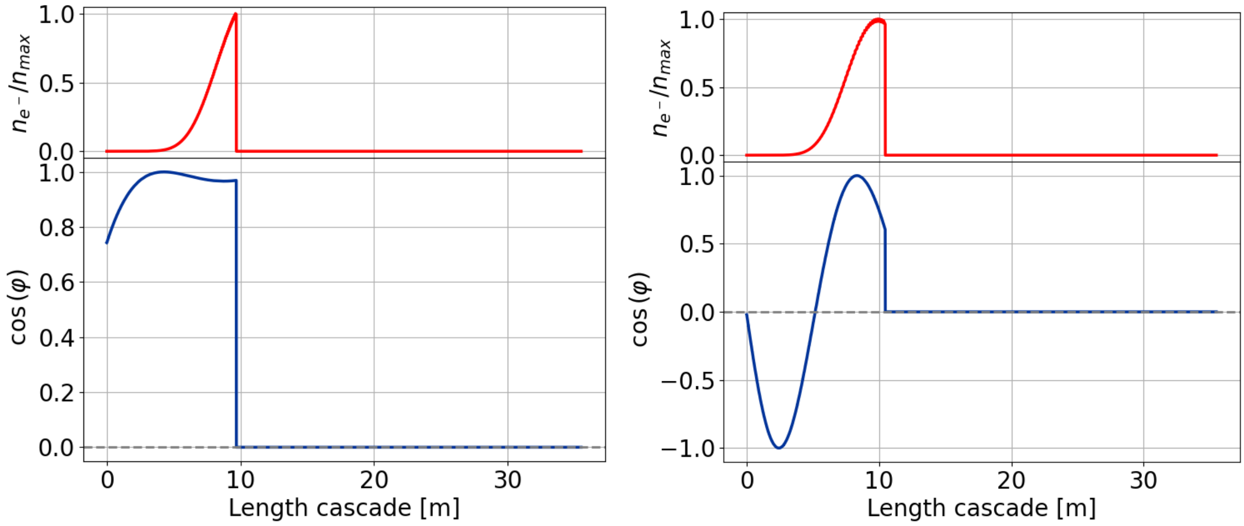

(a) (b)

Figure 5.19: The electron density and phase profile for the cascade direction (a) (90°, 249°) and (b) (90°, 263°). These are two directions where the definition for the phase coherence in Equation (5.2) fails.

5.6.2 Definition 2

The second definition does not use the derivative of the phase profile anymore. Instead, a probability density function (pdf) of the phase profile is made. This pdf is constructed by determining the total area beneath the curve and subsequently dividing every point of the phase profile by this area. Once the pdf is constructed, it is once again weighted with the normalised electron density profile for the same reasons as previously explained. Finally, the result is integrated and the phase coherence is given by

$$C = \int \mathrm{pdf}(\cos(\varphi)) \cdot \frac{n_{e^-}}{n_{max}} dl \ . \tag{5.3}$$

This definition tries to represent the amount of phase coherence by looking at how much the signal oscillates in the dominant region of the cascade. If a strong oscillation is still present after weighting, the integral of the curve will be smaller hence leading to a small value for C. On the other hand, if the phase profile is flat, the integral will be larger as the electron density profile is multiplied with a constant value. Having a constant phase profile indicates perfect constructive interference, independent of the constant value of $\cos(\varphi)$. Imagine having two equally long and constant phase profiles with $\cos(\varphi) = 1$ and $\cos(\varphi) = 0.5$. Since the profiles are equally long, meaning they reach the peak voltage at the same time, their electron density profiles are identical. If these two phase profiles are simply multiplied with the weight n_{e^-}/n_{max}, the resulting C will be different for the two constant phases. The profile with $\cos(\varphi) = 1$ will have a C double that of $\cos(\varphi) = 0.5$. This is not allowed as a constant phase means perfect constructive interference, independent of the value. Therefore a normalisation procedure must be used to to avoid the above situation. Taking the pdf of the phase profile before weighting should ensure this.

Once again, the angular plot for a fixed zenith of $\theta = 90°$ is constructed comparing the peak voltage for 360 cascade directions with their phase coherence values defined by Equation (5.3). The result is shown in Figure 5.20. Definition 2 is better than Definition 1 as more structure is visible in the phase coherence due to avoiding the infinities. For $\phi \in [90°, 126°]$ and $\phi \in [234°, 270°]$ the peak voltage profile and phase coherence show similar patterns and both have their maximum at the angles $\phi = 111°$ and $\phi = 249°$. Outside of this region, the two profiles show a different behaviour. The phase profile in the hemisphere pointing away from the receiver is typically a bit larger than the peak voltage compared to their maxima. On top of that, the region $\phi \in [126°, 234°]$ shows the opposite behaviour. The reason for this discrepancy can be twofold. Besides phase coherence, other effects are at play modulating the shape of the waveform or the definition of phase coherence is not stable for all directions yielding too small or too large values. A combination of the two could also be the reason. It is found that Definition 2 also fails at delivering a correct value for the

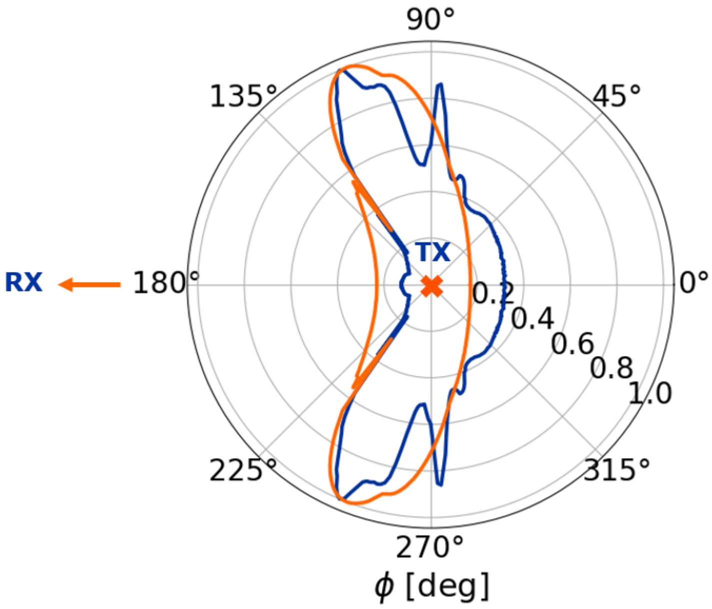

Figure 5.20: An angular plot showing the peak voltage and phase coherence as a function of the azimuth angle for a fixed zenith angle $\theta = 90$. In blue the C-value as defined in Equation (5.3) and in orange the peak voltage.

phase coherence in a very specific situation. This is once again explained using two theoretical phase profiles shown in Figure 5.21. For simplicity, both are taken to be flat with the same phase value $\cos(\varphi) = 1$ but the peak voltage time is reached at different moments. Hence the profiles have a different length. The pdf of both profiles is shown in the left panel of Figure 5.22 where the blue curve is the pdf of the short profile and the orange curve is the pdf of the longer profile. The right panel in Figure 5.22 shows the weighted pdf for the two situations. As both phase profiles are flat, the longer one of the two should have the largest C as its ionization trail is more developed. Looking at these graphs alone, it is not immediately clear which one of the two has a larger area beneath the curve. Performing the integral, it is found that $C_{short} = 0.13$ while $C_{long} = 0.11$ and thus poses a contradiction with the above statement. It is noted that applying the pdf definition to the two flat phase profiles in Figure 5.17 gives $C_{short} = 0.13$ and $C_{long} = 0.33$. Hence, not always does the definition fail at giving a C-value that makes sense. Still, if there is only one situation in which it fails, the definition should be changed.

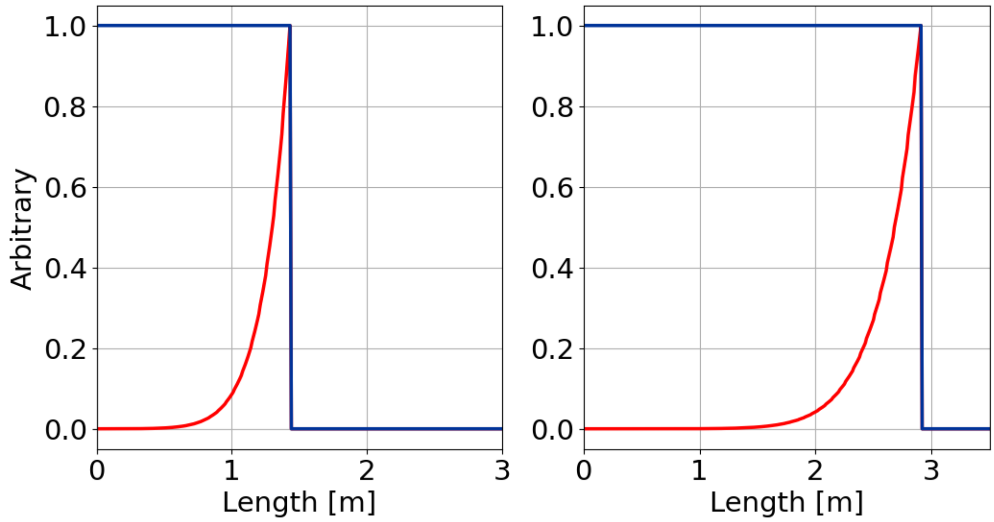

Figure 5.21: Two artificially created flat phase profiles (blue) and their electron density profile (red) for a different peak voltage time.

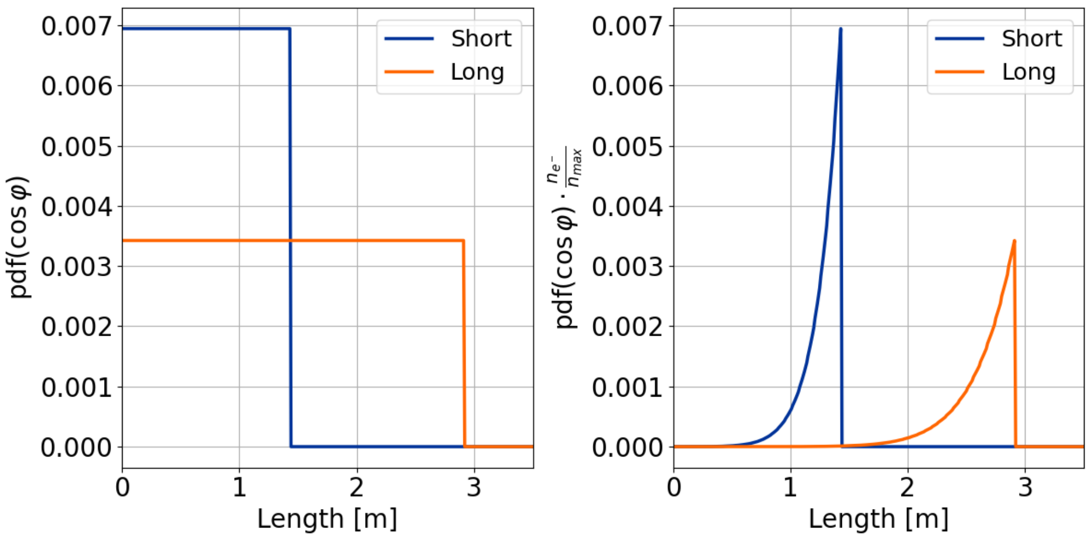

Figure 5.22: *Left panel*: The pdf for the two theoretical phase profiles in Figure 5.21. The pdf of the shortest profile is drawn in blue while the longest is in orange. *Right panel*: The weighted pdf of both profiles with the same colour code applied as in the left panel.

5.6.3 Definition 3

The last definition for phase coherence is related to Definition 2 and will turn out to be a stable one. Instead of making a pdf of the phase profile $\cos(\varphi)$, the phase itself is weighted with the normalised electron density profile. Recall that the pdf procedure in Definition 2 ensures that every flat phase profile of the same length has the same C-value independent of its constant value. In this new definition, the weighted phase profile is normalised by dividing it by the maximum. Just as in all the previous definitions, the result of the above procedure is integrated over the entire length of the ionization trail to yield a quantitative value for the phase coherence

$$C = \int \left(\cos(\varphi) \cdot \frac{n_{e^-}}{n_{max}}\right)_{norm} dl \; . \tag{5.4}$$

Just as Definition 2, the idea behind this definition is to check whether or not the phase profile is oscillating in the region where the segments in the ionization trail contain the most electrons. The only difference with Definition 2 is the way a normalisation is performed.

Once again, the angular plot for a fixed zenith angle $\theta = 90°$ is constructed comparing the peak voltage and phase coherence for 360 different cascade directions. The result is shown in Figure 5.23 from which it becomes immediately clear that both quantities show similar patterns over the entire azimuth range from 0° to 360°. Even in the regions where Definition 2 failed to reproduce the same pattern as the peak voltage, this definition succeeds. Finding this parametrization for the phase coherence and the fact that it is similar to the peak voltage shows that most of the general morphology in the 2D peak voltage plot in Figure 5.4 can be accounted for by looking at the phase information in the ionization trail.

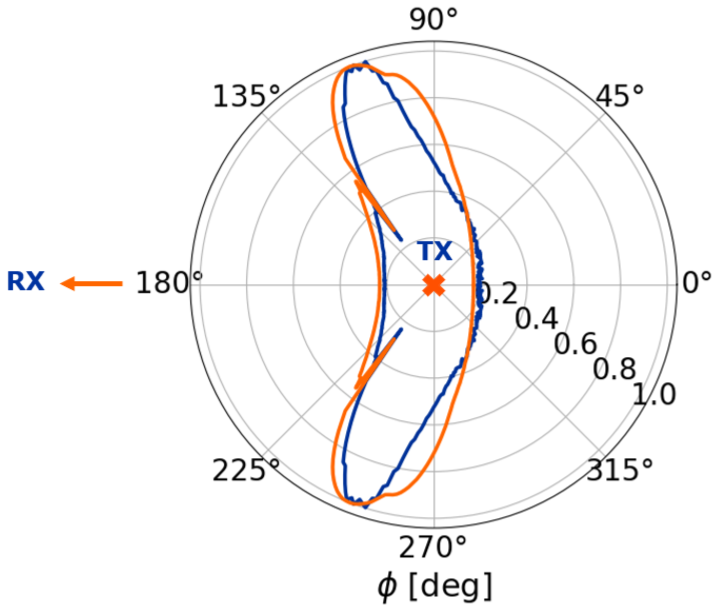

Figure 5.23: An angular plot showing the peak voltage and phase coherence as a function of the azimuth angle for a fixed zenith angle $\theta = 90$. In blue the C-value as defined in Equation (5.4) and in orange the peak voltage.

Needless to say, the definition seems promising but should also be checked for its stability. A first check consists of constructing the azimuth plot for a different fixed zenith angle. This allows for verifying that no lucky geometry was chosen for the definition. The result for fixed zenith $\theta = 30°$ is shown in Figure 5.24 and reveals that the definition remains accurate. It could even be argued that it gets better for these cascade directions. Up until now the standard simulation parameters in Table 5.1 were kept fixed for all simulations in this section. From the results in Section 4.4 it can be argued that the effect of the primary energy E_p will be small as it was shown that both the electron density profile and peak voltage scale linearly with E_p. This implies that both quantities will change in the same manner when choosing a different E_p. The effect of the lifetime is also investigated by performing actual simulations. A smaller lifetime $\tau = 0.5$ ns is chosen and an angular plot for fixed zenith angle $\theta = 90°$ is constructed by simulating the waveform, 2D phase profile and 2D electron density for all 360 directions. From these data files the angular plot can be produced following the procedures above. The results are shown in Figure 5.25a from which it can be deduced that the definition is stable when decreasing the lifetime. It is also verified if the definition holds when a larger lifetime than the standard value is chosen. The angular plot for a lifetime $\tau = 100$ ns at a fixed zenith angle $\theta = 30°$ is constructed and the result is shown in Figure 5.25b. The phase coherence still follows the same pattern as the peak voltage plot though it is less close to it than in Figure 5.24 where a standard lifetime of $\tau = 10$ ns was used. Due to the longer lifetime of 100 ns the waveforms will get much broader in time as already observed in Figure 4.4. This results in the fact that the peak voltage is smeared out over a longer period of time, making it harder to select. This could form a possible explanation for the discrepancy observed in Figure 5.25b. Since the general shape of the phase coherence still nicely follows that of the peak voltage and the real lifetime of the electrons is believed to be $O(1\text{–}50)$ ns [83], it is concluded that the definition is stable against changing the plasma lifetime. The stability of the definition could also be checked against the chosen transmit frequency. For all the previous results $f(TX)$ was kept at its standard value of 50 MHz. Unfortunately due to a lack of time, this check could not be included in this work but will be done in the near future.

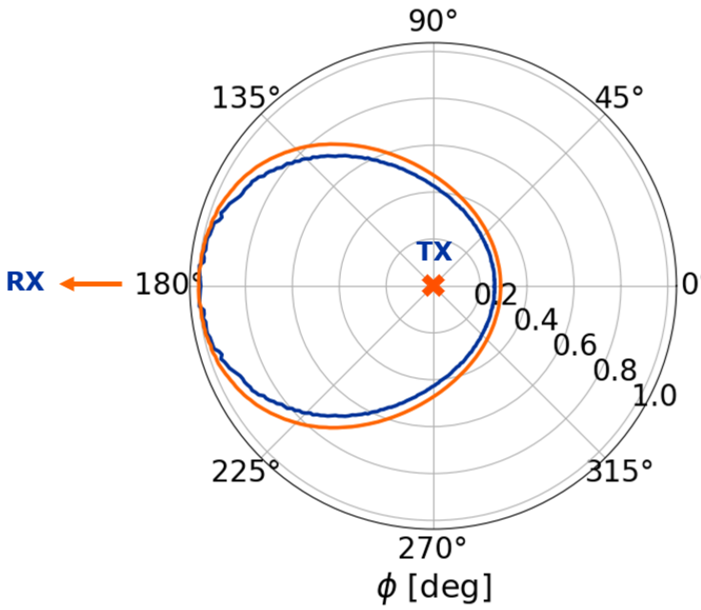

Figure 5.24: An angular plot showing the peak voltage and phase coherence as a function of the azimuth angle for a fixed zenith angle $\theta = 30$. In blue the C-value as defined in Equation (5.4) and in orange the peak voltage.

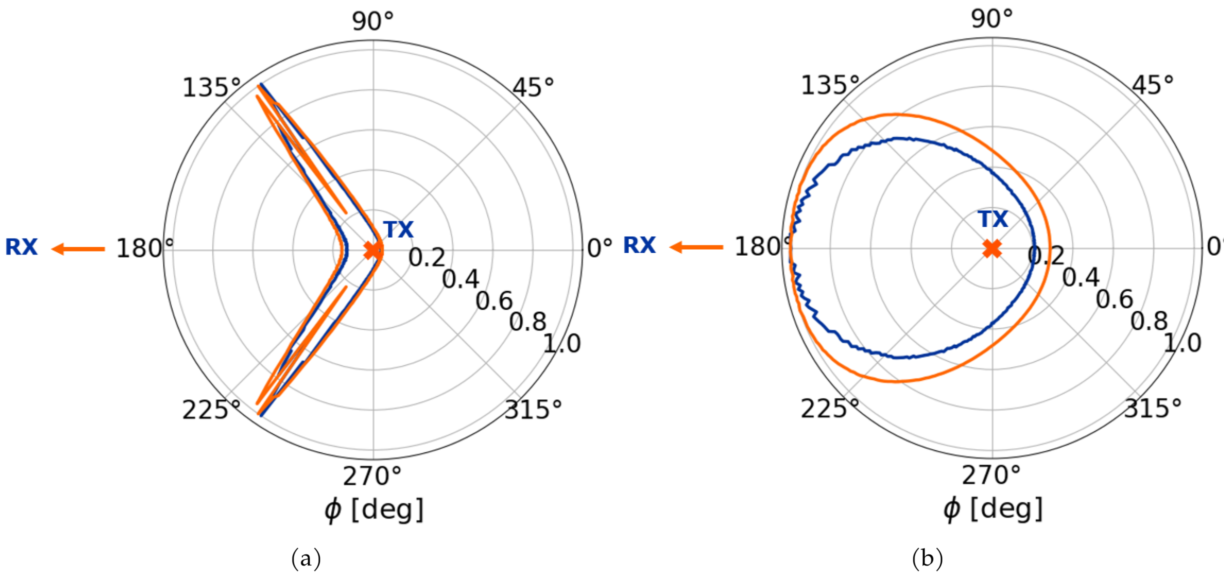

Figure 5.25: Angular plots of the peak voltage and phase coherence for two different plasma lieftimes. In blue the C-value as defined in Equation (5.4) and in orange V_{peak}. (a) The lifetime is set to $\tau = 0.5$ ns and the zenith angle is fixed at $\theta = 90°$. (b) The lifetime is set to $\tau = 100$ ns and the zenith angle is fixed at $\theta = 30°$.

A final verification of the definition consists of producing a zenith plot instead of an azimuth plot. All the standard values for the simulation parameters in Table 5.1 are set. For a fixed azimuth of $\phi = 25°$ and

$\theta \in [0°, 180°]$ with a stepsize of 1° a total of 180 cascade directions are selected. Not the full 360° is chosen because of the degeneracy in the zenith angle explained in Section 5.1 and to reduce the computation time. For all cascade directions, the waveforms, 2D phase profile and 2D electron density are simulated. The peak voltages are selected from the waveforms and the phase coherence at the corresponding time is calculated using Equation (5.4). The results are plotted in the same zenith plot shown in Figure 5.26. This figure reveals

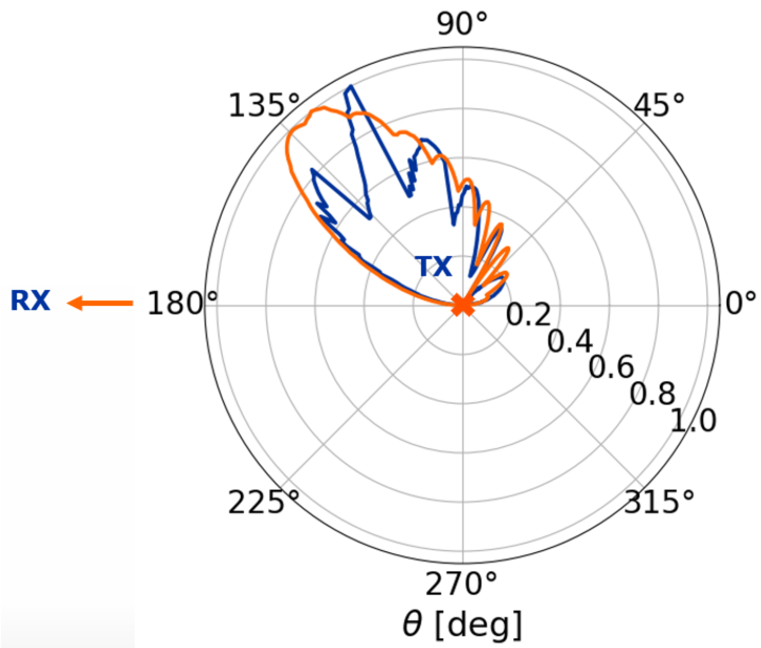

Figure 5.26: A zenith plot showing the peak voltage and phase coherence as a function of the zenith angle for a fixed azimuth angle $\phi = 25$. In blue the C-value as defined in Equation (5.4) and in orange the peak voltage.

that the definition gets worse when producing a zenith plot. The exact reason why is not clear but could be a consequence of multiple factors. First, varying the zenith corresponds with moving vertically in the 2D peak voltage plot in Figure 5.4. Moving horizontally corresponds with varying the azimuth angle. It is clear from the 2D peak voltage plot that the former experiences more change over a shorter part of the phase space. A zenith plot comes across all three observed features: low-intensity ring, high-intensity swirl and horizontal bands. An azimuth plot always stays within a single horizontal band. Other mechanisms can influence the peak voltage and as such create a stronger discrepancy between both quantities. A second effect can arise from the way MARES segments the ionization trail. As explained in Appendix A, the trail is segmented from the point of view of the transmitter. From the used detector setup in Figure 4.5, it becomes clear that the size of the ionization trail seen by the transmitter does not change when keeping the zenith angle fixed. Hence, in an azimuth plot, for all 360 cascade directions, the electron density profile is the same. For each direction in a zenith plot, the electron density must be simulated again as the projected size of the ionization trail changes when changing the zenith angle. The different 2D electrons density plots and how they are reduced to a 1D plot as described above, could result in having more numerical errors in a zenith plot than an azimuth plot. More detailed investigations regarding this discrepancy will be conducted in the near future.

It is concluded that the definition for C in Equation 5.4 is the most stable out of all three. This definition is robust against changing simulation variables and selecting different parts of the phase space of the cascade directions. It can recreate the same patterns as the peak voltage in the angular plots which indicates that phase coherence is one of the driving effects in the 2D peak voltage plot. Being able to parameterise the phase coherence of the ionization trail could be used to optimize the MARES code and make the simulation software faster.

5.7 Horizontal bands

In this section, a physical explanation is given for the observed horizontal bands in the 2D peak voltage plot in Figure 5.4. The structure of these bands resembles that of a diffraction pattern and it is investigated if that is their origin. The TX-cascade-RX system can be seen as a classical setup for a diffraction experiment. The transmitter sends out radio waves that come across an obstacle, the ionization trail, diffracting the incoming plane waves that are subsequently observed by the receiver. In classical optics, this obstacle is often a single slit or opening in a screen rather than a materialistic object. It turns out that diffraction from a single slit is completely analogous to the diffraction from a rod through what is called Babinet's principle [6]. The single-slit experiment is discussed in detail in Appendix E. It should be noted that diffraction is also linked to phase coherence.

5.7.1 Diffraction from an ionization trail

In a single slit experiment the location of the dark spots are given by [85]:

$$\sin\vartheta = m\frac{\lambda}{D}\,, \tag{5.5}$$

where λ is the wavelength of the EM wave, D the width of the slit and $m = \pm 1, \pm 2$, etc. The distance between two local minima corresponds with the width of the diffraction band. It is noted that in a ϑ-space the width of the bands will monotonically increase instead of remaining constant as in a $\sin\vartheta$-space. The details of this can be found in Appendix E.

From Babinet's principle, the same conclusions can be made regarding diffraction from an object. It is first verified using a back-of-the-envelope calculation that the detector setup used in all simulations shown in Figure 4.5 obeys the Fraunhoffer diffraction condition: $R > D^2/\lambda$, where R is the distance between the source and the slit [85]. The typical size of the ionization trail for the standard simulation parameters set in Table 5.1 is $D \sim \mathcal{O}(10\text{ m})$ and the wavelength of the transmitted radio waves is $\lambda \sim \mathcal{O}(1\text{ m})$. Hence, it is found that the distance between the antennas and the ionization trail should be $R \sim \mathcal{O}(100\text{ m})$ in order to be in the far-field. This minimal distance R is satisfied for the chosen detector setup in Figure 4.5. This allows for treating the TX-cascade-RX system considered in this work as a single-slit experiment. The transmit antenna is considered to be the source of the parallel rays in Figure E.1, the ionization trail the slit and the receiver is a point on the screen behind the slit. Based on the schematic overview in Figure E.1, it is deduced that a central bright band is observed when the rays from the transmitter are hitting the ionization trail head-on. From the standard detector setup in Figure 4.5 this corresponds with the cascade having a zenith angle $\theta = 90°$. The azimuth angle can be any value since the size of the ionization trail observed by the transmitter only depends on the zenith angle in this specific detector setup. Hence, this explains why the bands in the 2D peak voltage plot run horizontally. When the zenith angle is changed to a different value, a different spot in the diffraction pattern is observed by the receiver. This can be understood by looking at the panels b-d in Figure E.1. In these figures, it was assumed that the source is sitting on the left of the slit and the observer on the right. Depending on the angle, a dark or bright spot is observed. If the direction of the arrows is reversed, the source would light up the slit from an angle and a dark or bright spot would be observed by the receiver on the other side of the slit depending on this angle. This situation can be recreated by keeping the source stationary and turning the orientation of the slit, or in the TX-cascade system, the cascade. Hence, from the moment the cascade is moved with a certain angle ϑ with respect to the central maximum at $\theta = 90°$, consecutive bright and dark spots will be observed.

5.7.2 The effect of the transmit frequency and refractive index

As became clear from the previous section, the width of the diffraction bands depends on two variables: the wavelength incident on the ionization trail and the length of the trail. If the horizontal bands in the 2D peak voltage plot are a consequence of diffraction, changing the transmit frequency should alter their width. Choosing a smaller $f(TX)$ would correspond with increasing the wavelength λ and subsequently larger bands as deduced from Equation (5.5). Setting a larger $f(TX)$ would result in the opposite effect. This is investigated by producing two peak frequency plots analogue to the standard one in Figure 5.4 for

$f(TX) = 10$ MHz and $f(TX) = 250$ MHz. The results are respectively shown in Figure 5.27 and 5.28. From both figures, it becomes immediately clear that the 2D peak voltage plots change rather significantly with respect to the standard 2D peak voltage plot in Figure 5.4. First, the focus is directed to the behaviour of the horizontal bands. As expected, setting a lower transmit frequency results in much broader bands. When setting $f(TX) = 250$ MHz narrow diffraction bands are observed around $\theta = 60°$. In other regions, the bands have disappeared. This is believed to be a result of the finite resolution in the zenith angle of 1°. The width of the diffraction bands has presumably become smaller than this resolution, resulting in their disappearance. The observed response of the horizontal bands to changing the transmit frequency is the first indication that diffraction is a possible origin for this feature.

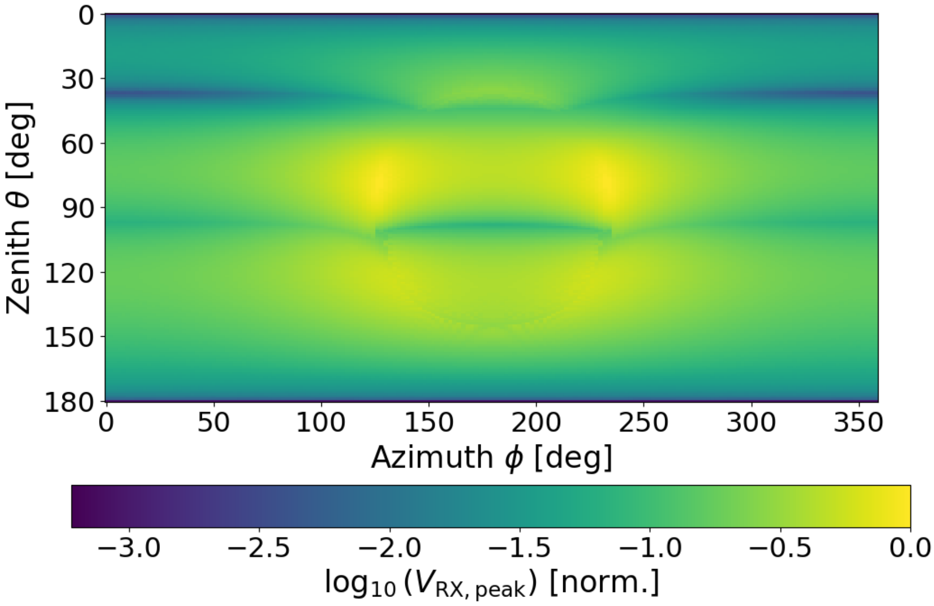

Figure 5.27: A 2D peak voltage plot for $f(TX) = 10$ MHz.

A second indication was already shown before but not yet discussed when looking at the origin of the low-intensity ring. In Figure 5.8, the 2D peak voltage plot was produced for a refractive index $n = 1$ proving the Cherenkov origin of the low-intensity ring. In that same figure, the horizontal bands have become wider with respect to the standard 2D peak voltage plot even though the transmit frequency was kept fixed. In any medium, the relation between the speed of light, the wavelength and the frequency of an EM wave is given by

$$\frac{c}{n} = \lambda \nu \,, \tag{5.6}$$

where n is the refractive index and c is the speed of light in vacuum. Choosing a different refractive index changes the left-hand side of this equation. This implies that the right-hand side must change as well. Hence, λ and ν have to change or at least one of the two quantities. As it turns out, the frequency of an EM wave remains the same when the refractive index is changed. This can be proven from the boundary conditions for EM waves at an interface. The calculation is omitted in this work but can be found in [86]. Hence, the wavelength must change to obey Equation (5.6) and subsequently results in a different width for the diffraction bands. In Figure 5.8, the horizontal bands appear wider than in the standard 2D peak voltage plot. If their origin is diffraction, this behaviour is understood from the above. Changing $n_{ice} = 1.78$ to $n = 1$, results in the fact that c/n increases and λ has to increase as well. From Equation (5.5), it becomes clear that the diffraction bands will become wider as a result.

Before continuing the discussion about the horizontal bands, the focus is redirected to the 2D peak voltage plots for a different $f(TX)$. In Figure 5.27, $f(TX) = 10$ MHz which corresponds with a wavelength $\lambda \approx 17$ m. This wavelength gets close to the total length of the ionization trail and has therefore difficulties with probing the structure of the trail. In other words, a too-low resolution is used to look at the ionization

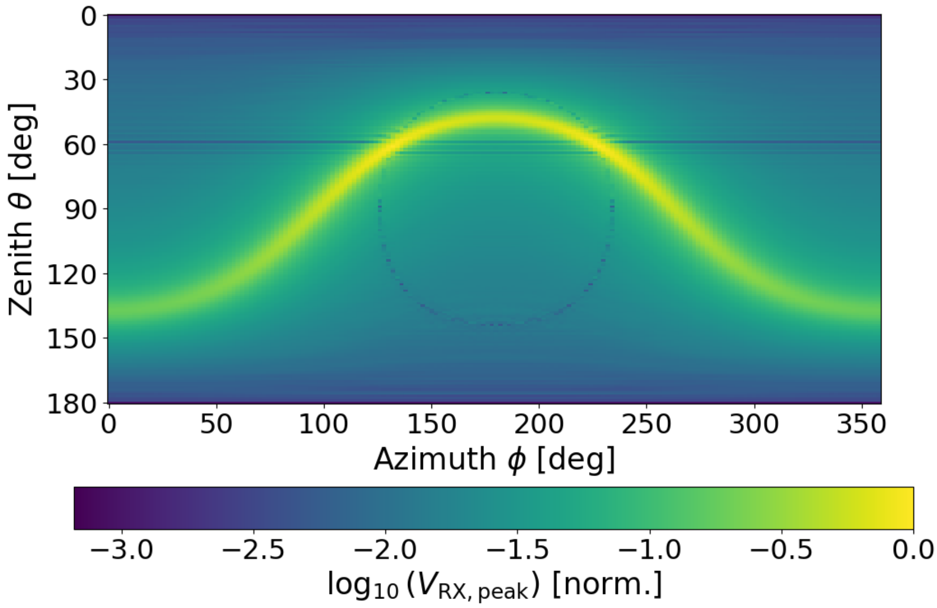

Figure 5.28: A 2D peak voltage plot for $f(TX)$ = 250 MHz.

trail and as a consequence, it starts to resemble more and more a point-like object. This explains why the more detailed structures and features in Figure 5.27 have disappeared. Using a smaller transmit frequency to investigate the scatter is like using an unfocused camera to take a picture. The complete opposite is perceived in Figure 5.28. In this figure, the transmit frequency is five times larger than in the standard 2D peak voltage plot. As such, all the details and features become sharper. The high-intensity swirl in Figure 5.28 is for example much more resolved and contained within a smaller part of the phase space. The top half of the low-intensity ring becomes visible because of this. In the standard 2D peak voltage plot, it was masked by the more smeared-out high-intensity ring.

5.7.3 Doppler effect

In the previous section, evidence was presented for the origin of the horizontal bands from the way they respond to a varying transmit frequency and refractive index and how this is consistent with a diffraction pattern. One interesting observation in the standard 2D peak voltage plot is the fact that the band width decreases from the top, at $\theta = 0°$, towards the bottom and seemingly disappears at $\theta \approx 120°$. Moving along a horizontal band from $\phi = 0°$ to $\phi = 360°$ shows the band bending when it comes across the high-intensity swirl. It is believed that a possible explanation for these features lies in the Doppler effect shifting the peak frequency of the signal.

As shown in Appendix E, looking at the diffraction pattern in a ϑ-space results in a natural widening of the diffraction bands when moving away from the central maximum. The relation between the zenith angle θ and diffraction angle ϑ is simply: $\vartheta = 90° - \theta$. Hence, it is expected to see the horizontal diffraction bands in the 2D peak voltage plot become wider in the limits $\theta \to 0°$ and $\theta \to 180°$ centred at $\theta = 90°$. For the upper half of the 2D peak voltage plot, this is observed. It is verified if the observed width corresponds with the predicted one from Equation (5.5). Using the same order-of-magnitude estimation of the wavelength of the radio waves and the size of the ionization trail from Section 5.7.1, it is found that $\lambda/D \approx 0.1$. This implies that the width of the diffraction band between the first and second local minimum is expected to be $\Delta\vartheta_{2,1} = 5.80°$. The observed width of the band is much larger and found to be $\Delta\vartheta_{2,1} \approx 11°$. A possible explanation for the additional widening of the horizontal diffraction bands can be found in the Doppler shifting of the radio waves. Looking again at the 2D peak frequency plot in Figure 5.5, reveals that the peak frequency in the observed waveforms shifts depending on the cascade direction. In the region for $\theta < 90°$, predominantly a redshift is observed. This redshift causes the wavelength λ to increase leading to wider diffraction bands.

This Doppler effect can create an additional widening not taken into account in the previous comparison between the observed and predicted width of the bands as the wavelength corresponding to the transmit frequency was chosen. As it turns out from Figure 5.5, the peak frequency at the first and second minima in the diffraction pattern, not in the neighbourhood of the swirl, is $f \approx 17.4$ MHz. This corresponds with a wavelength $\lambda = 9.7$ m resulting in $\Delta\vartheta_{2.1} \approx 19°$. The redshift is too large to fully explain the observed widening.

The diffraction bands at zenith angles $\theta > 90°$ are expected to be symmetrical with the $\theta < 90°$ region. This is not the case when looking at the 2D peak voltage plot. A possible explanation can once again be found from the Doppler effect. In the region $\theta > 90°$, mostly a blueshift of the peak frequency is observed. Due to the increase of the frequency, and thus a subsequent decrease of the wavelength, a decrease in the width of the diffraction bands is expected. This decrease dominates over the natural increase in ϑ-space and could become so strong that the width of the bands falls below the resolution in the zenith angle of 1°. A second possible explanation could be the presence of other features, like the tails of the high-intensity swirl. The phase coherence creating the swirl could be dominating over diffraction in this region and cause the diffraction bands to fade when getting closer to it.

From the 2D peak frequency plot, it was found that the swirl corresponds with no Doppler shift and thus a peak frequency at $f(TX)$. In the region $\theta < 90°$ it is clear that moving horizontally along a diffraction band increases the peak frequency of the signal and as such decreases the wavelength. Hence, the diffraction band is expected to narrow along the horizontal band when entering the high-intensity swirl causing it to bend downwards and towards the central point at $\theta = 90°$. The same reasoning can be applied in the region $\theta > 90°$ but instead, the bands keep bending downwards instead of towards $\theta = 90°$. It is not immediately clear why this occurs. It could be a consequence of multiple effects changing the diffraction pattern. The bending happens in a region of the phase space where strong phase coherence arises. On top of that, it is close to the low-intensity ring where Cherenkov effects become important and also strong changes in the frequency occur.

It becomes clear that the horizontal bands in the 2D peak voltage plot do behave like a diffraction pattern and form a natural explanation for their existence. These bands show interesting features that could be partially explained by the frequency space and the observed Doppler shifts. Still, some questions remain as predictions and observations are not always consistent. Therefore, a more detailed study will be performed in the near future using for example a different detector setup. This will hopefully shed more light on the remaining open questions regarding these horizontal bands.

5.8 Lifetime effects

In this section, the influence of the lifetime of the electrons is investigated. As already became clear from Section 4.3, choosing the lifetime can have significant consequences on the outcome of the waveform. Hence, the effect of this parameter on the 2D peak voltage plot is considered. The same procedure is used to construct a 2D peak voltage plot, by keeping all the simulation parameters in Table 5.1 fixed apart from the lifetime. In Figure 5.29, the lifetime is set to $\tau = 0.5$ ns. Decreasing the lifetime causes the high-intensity swirl to disappear. A small lifetime makes the ionization trail resemble more like a point-particle as the electrons recombine quickly after their creation. Hence, there is little time to create an extended ionization trail. In order to have large phase coherence, typically a significant amount of segments with lots of electrons in them need to be alive at the same time. Decreasing the lifetime makes it difficult to satisfy this condition. Therefore, the cascade directions on the high-intensity swirl do not experience a strong amplification anymore in their peak voltage and the feature disappears. Interestingly enough, the ring is split up into a low- and high-intensity part in Figure 5.29.This can be understood by looking at the 2D phase plot for two specific cascade directions on the ring. The direction $(67°, 130°)$ is taken as a point on the upper half and $(140°, 160°)$ on the lower half. The result for the former is shown in Figure 5.30. This figure shows that two effects are at play. First, the shape of the 2D phase profile resembles a lot like the expected relation between t and t' at the geometrical Cherenkov angle in Figure 3.4. This is expected as it was previously proven that the ring corresponds with a Cherenkov effect. This implies that all the emission from the segments arrives in a concentrated time period at the receiver. This leads to a natural enhancement of the observed peak voltage.

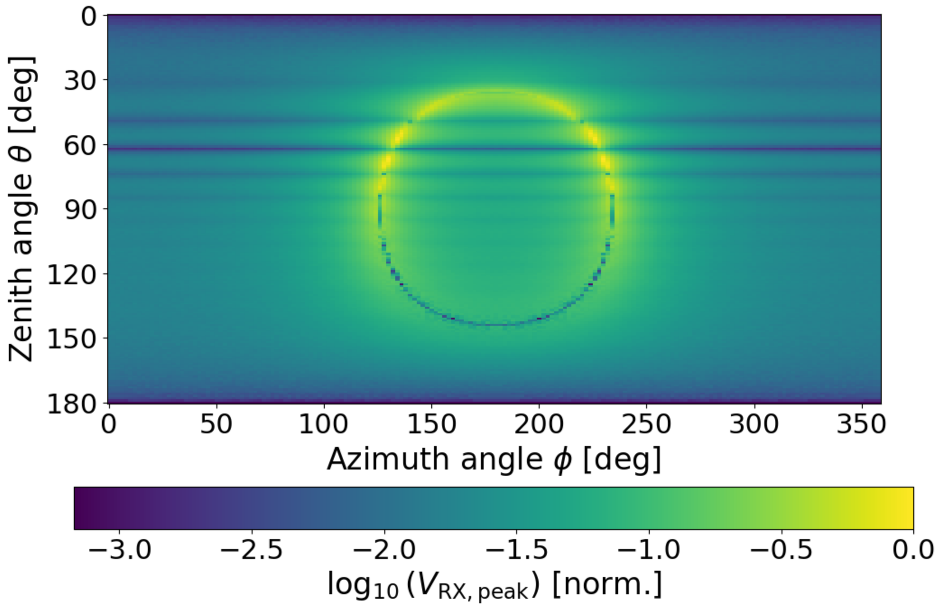

Figure 5.29: A 2D peak voltage plot for $\tau = 0.5$ ns.

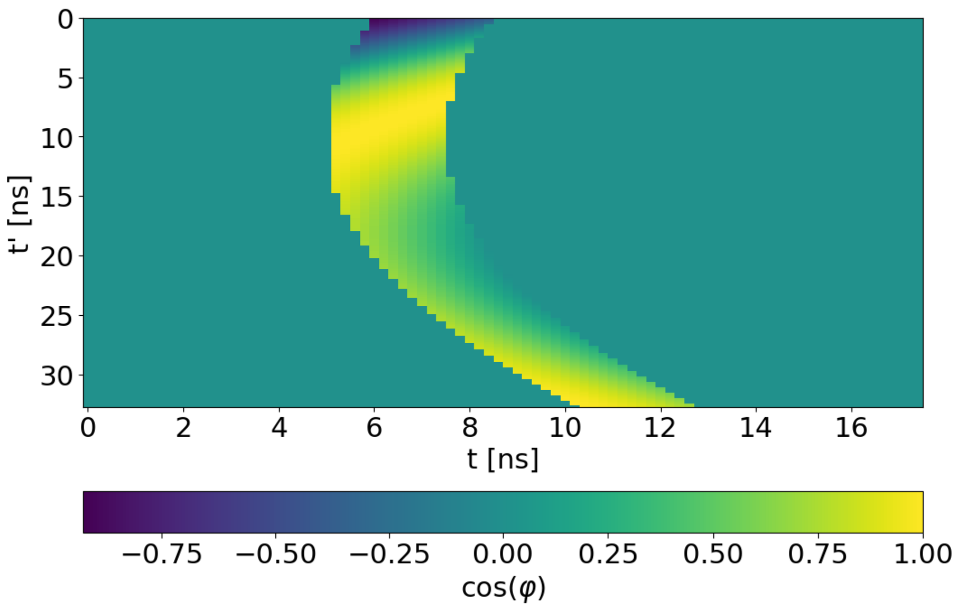

Figure 5.30: The phase profile observed by the receiver for a cascade traveling in the $(130°, 67°)$ direction.

Second, due to the Cherenkov effect, the point-like ionization trail seems to have an extended length as the consecutive signals from different points in space arrive at the same time. If the phases of these segments are the same, constructive interference arises leading to an additional boost of the signal. This is exactly observed in Figure 5.30 as the phase value is slowly varying.

The 2D phase profile for the point on the lower half of the ring is shown in Figure 5.31. As the point lies on the geometrical Cherenkov cone, the shape of the non-zero phase part in this figure is once again the same as the relation between t and t' shown in Figure 3.4. From this figure, it becomes clear why the lower point does not show a large peak voltage. There is a strong oscillation observed in the phase leading to destructive interference and a subsequent small peak voltage as a result. From Figure 5.30 and 5.31 it is concluded that two effects are competing with each other on the ring: phase coherence and Cherenkov effects.

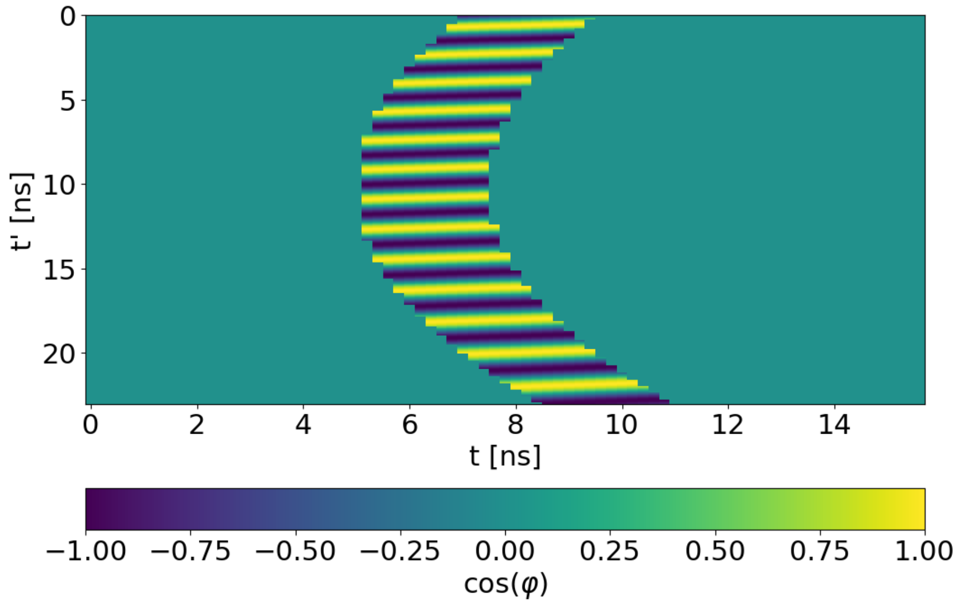

Figure 5.31: The phase profile observed by the receiver for a cascade traveling in the (160°, 140°) direction.

The horizontal diffraction bands in Figure 5.29 are unharmed by decreasing the lifetime. Diffraction is also a form of phase coherence, therefore, making this observation is rather remarkable. From first intuition, it is expected that these diffraction bands become fainter for the same reason the high-intensity swirl disappears. A possible explanation could be that time dilatation affects the observed τ. From Figure 5.30 and Figure 5.31, it is clear that the observed plasma lifetime of each segment is $\tau > 0.5$ ns. As such, the receiver still observes a more extended cascade than was first expected, and the horizontal diffraction bands remain. Still, due to the smaller lifetime, the number of electrons in each segment is smaller than for the standard $\tau = 10$ ns, leading to the disappearance of the high-intensity swirl. As such, it seems that by decreasing the lifetime, the Cherenkov effect becomes more dominant over the phase coherence. It is noted that more investigation will be performed in the near future regarding lifetime effects.

It is furthermore investigated how the 2D peak voltage plot changes when the lifetime is increased. In Figure 5.32, the results is shown for $\tau = 100$ ns. The larger lifetime causes the high-intensity swirl to become more prominent. This can be understood as increasing the lifetime causes the ionization trail to consist of more electrons at the time of the peak voltage and results in even more constructive interference than in the $\tau = 10$ ns case.

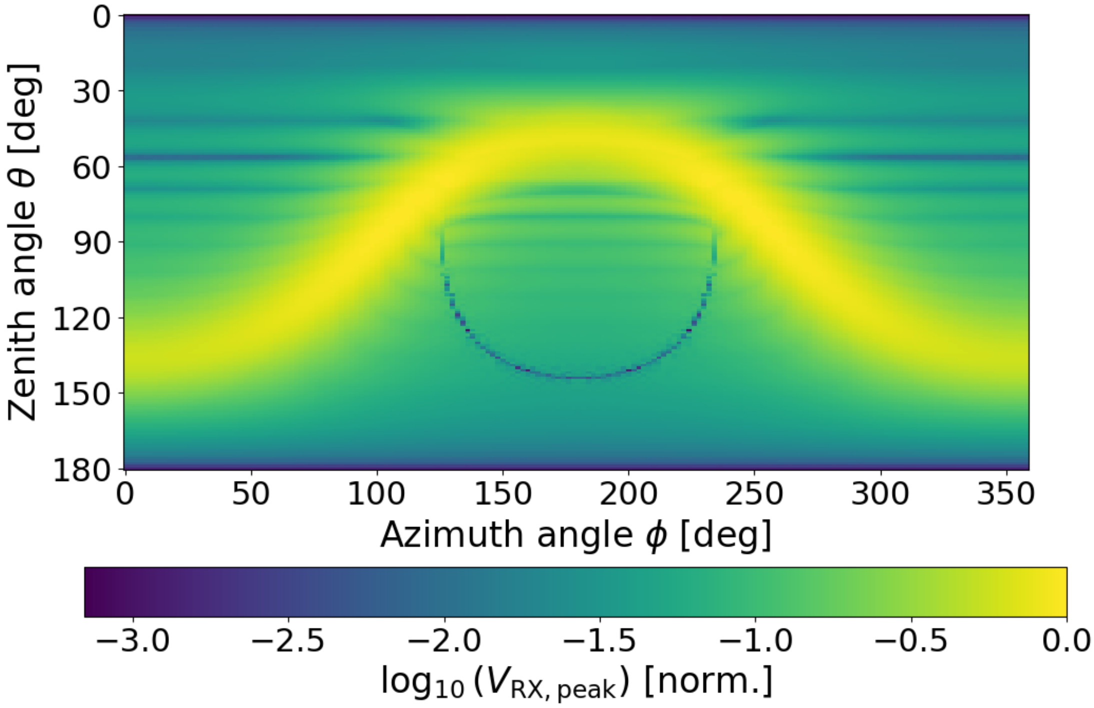

Figure 5.32: A 2D peak voltage plot for τ = 100 ns.

Chapter 6

Summary & outlook

High-energy neutrinos are a good candidate the solve the origin problem of ultra-high energy cosmic rays (UHECRs). UHECRs can interact at their source or on their way towards Earth with interstellar gas and background radiation fields resulting in the production of neutral and charged pions. When the charged pions decay, they will produce high-energy neutrinos that can be detected on Earth. Since neutrinos are chargeless they are not deflected by magnetic fields and due to their weakly interaction nature, they remain unharmed when passing through vast clouds of interstellar gas. Hence, when UHECRs interact near their source and produce neutrinos, the latter will reach Earth and if detected, point straight back towards the source of UHECRs.

Due to their weakly interacting nature, neutrinos are hard to detect on Earth. On top of that, the observed flux of high-energy neutrinos drops quickly resulting in the need for large-scale detector volumes to obtain an observable flux. Experiments searching for high-energy neutrinos never observe the neutrinos directly but always through the production of secondary particles when they interact in the detector volume. When a high-energy neutrino interacts in a medium, it leads to the production of highly energetic secondary particles and a subsequent particle cascade. There are multiple techniques for detecting this particle cascade. In this thesis, we considered a novel detection technique based on radar. When the particle cascade traverses a medium, it will leave behind a trail of ionization electrons. If this trail is dense enough, it can be detected using radar. Ice forms an ideal medium for this detection technique as it is dense enough to create compact ionization trails and has a large attenuation length for radio waves. Hence, large detector volumes can be probed with little instrumentation. As only recently in 2018, for the first time a radar echo signal from a particle cascade was observed in the lab, the detection technique is still in its infancy. As such lots of studies need to be performed regarding signal properties and reconstruction. In this thesis, a study of the radar echo signal properties in ice was performed using the existing simulation software MARES.

We started our study by performing some checks regarding the necessary simulation dimension that needs to be set in MARES to correctly simulate the ionization trail left in the wake of the neutrino-induced particle cascade. On top of that, we investigated the relation between the primary energy of the neutrino E_p and the maximum number of electrons alive inside the trail. We observed the expected linear relationship between the two quantities. We investigated the relation between the E_p and the peak voltage of the waveform as well and observed once again a linear relationship between the two quantities. This can be expected as a larger E_p leads to an overall increase in the number of electrons inside the ionization trail and a stronger radar reflection.

We continued our investigation by looking at the individual waveform for three different cascade directions for a specifically chosen bistatic radar setup. This detector geometry had the benefit of creating an easy link between the angles (θ, ϕ) describing the cascade direction and the position of the transmitter and receiver antenna. The transmitter antenna was positioned at $(0, 0, -100)$ m and the receiver at $(-250, 0, 0)$ m. As such the zenith angle θ corresponded in some sense with the relative orientation of the cascade with respect to the transmitter while the azimuth angle ϕ determined the orientation with respect to the receiver. By choosing three cascade directions pointing towards, away or perpendicular to the receiver, it became clear from the individual waveforms that relativistic Doppler effects are at play.

This result triggered our interest in the effect of the cascade direction on the radar echo signal and led to the creation of the angular plots. An angular plot shows the dependency of the peak voltage of a waveform as a function of one of the angles parametrizing the cascade direction. When we simulated the waveform of these cascade directions, some simulation parameters were kept fixed. The lifetime of the ionization electrons was chosen to be $\tau = 10$ ns, the primary energy of the neutrino $E_p = 1$ EeV, $n_{ice} = 1.78$, the transmit frequency $f(TX) = 50$ MHz, antenna gain 0 db and antenna power $P = 1000$ W. These are the standard simulation parameters for all simulations in this thesis unless specified otherwise. In these angular plots, both symmetries and beaming patterns were observed. We estimated the Cherenkov cone from these figures and it became clear that sampling plays an important role in correctly identifying this cone.

The observations from the angular plots were an invitation to probe the entire phase space of the cascade directions. As such, we varied $\theta \in [0°, 180°]$ and $\phi \in [0°, 360°]$ and combined all of these directions into one single plot. This resulted in the construction of the 2D peak voltage plot. In this plot three distinct features were visible: low-intensity ring, high-intensity swirl and horizontal bands. The main goal of my thesis consisted of figuring out the physics behind these features. In the pursuit of this goal, we constructed a frequency equivalent of the 2D peak voltage plot by making a Fourier transform (FT) of the waveform of all cascade directions and selecting the dominant or peak frequency from the FT. This peak frequency was plotted as a function of the cascade direction from which it became clear that Doppler effects are strongly influencing the signal. This 2D peak frequency plot gave a hint about the origin of the low-intensity ring as in the neighbourhood of this feature, very strong blueshifts were observed. This behaviour is expected near the Cherenkov angle.

Still, we investigated the origin of the low-intensity ring in more detail and believed its origin came from the geometrical Cherenkov effect. This was confirmed by changing the refractive index of the ice in the simulations. When setting $n = 1$ the ring disappeared, delivering a consistent result with theory. On top of that, we found that the value for the Cherenkov angle from the 2D peak voltage plot was $\theta_c \sim 54°$ which is relatively close to the predicted value of $\theta_c = 55.82°$. These observations provide strong evidence for the Cherenkov nature of the low-intensity ring, indicating that it is a purely geometrical effect that arises in a relativistic situation. The results we found from varying the sampling rates supported this conclusion also.

We concluded that the high-intensity swirl is the result of strong constructive interference between the different segments inside the ionization trail. For the cascade directions on the high-intensity swirl we found that at the time of the peak voltage, the ionization trail had developed towards its maximum. Hence, the segments with the most electrons in them were alive. Due to these dominant segments having similar phase values at the receiver antenna, constructive interference between them arises. We aspired to find a quantitative definition of the phase coherence as it would allow for making a comparison with the peak voltage. We proposed three different definitions of which only one turned out to be stable and well defined. On top of that, we found that the definition showed the same overall shape profile as the peak voltage in the angular plots. This yielded evidence for the physical nature of the overall morphology of the 2D peak voltage plot and the origin of the high-intensity swirl.

The horizontal bands resembled a standard diffraction pattern from a single slit. As such, we outlined the analogy between the TX-cascade-RX system and that of a single-slit experiment using Babinet's principle. We investigated how these horizontal bands responded to changing the transmit frequency and refractive index and found that they behave like a diffraction pattern. They become wider or thinner with a respectively increasing or decreasing transmit wavelength as is expected from a single-slit diffraction pattern. As changing the refractive index of a medium results in a change in the wavelength of the EM wave, the bands became wider when $n = 1$. However, the horizontal bands in the 2D peak voltage plot showed some interesting behaviour when deviating from the central maximum at $\theta = 90$ °. First, the bands became wider in the region $\theta < 90°$. We proposed a possible explanation from the fact that in the 2D peak voltage plot, the distance from the central maximum is plotted in a ϑ-space instead of the more commonly used $\sin(\vartheta)$-space where $\vartheta = \theta - 90°$ is the diffraction angle. In a ϑ-space a natural widening of the bands is expected when moving away from the central maximum. Still, we found that the observed widening was too large to be solely explained by this. We believe that a second effect at play is the Doppler shift of the transmit frequency and thus wavelength. We argued that this could result in an additional widening of the bands. As it turned out, the redshift of the transmit frequency was too large to explain this effect. In the region, $\theta > 90°$ the bands disappear completely. A strong blueshift is observed in this region and could lead to the bands becoming smaller than the resolution of 1° used for the zenith angle. As such they become invisible. The horizontal bands bent when entering the high-intensity swirl. The change of the transmit frequency inside such a band due to Doppler shifts could form a possible explanation in the region $\theta < 90°$ but cannot explain the observed bending in the region $\theta > 90°$. We expected from the 2D peak frequency plot that the bands bend towards the central maximum at $\theta = 90°$ but instead, they show the opposite behaviour in the region $\theta > 90°$. We therefore concluded that the horizontal bands are a diffraction pattern from the way they respond to changing several simulation parameters but the origin of certain of their features remains unclear and requires further investigation.

Lastly, we investigated the effect of the plasma lifetime on the 2D peak voltage plot. When we decreased the lifetime to $\tau = 0.5$ ns, the high-intensity swirl disappeared. This could be explained by the fact that a smaller lifetime results in a smaller amount of electrons alive at a single instance in time. As such, the ionization trail looks like a point-like object in which the phase coherence has drastically decreased due to the loss of an extended trail. We also observed that the ring splits up into a high-intensity upper half and a low-intensity lower half. This could be explained by the fact that on the ring two different physical effects are competing with each other: phase coherence and Cherenkov effects. When we increased the lifetime to $\tau = 100$ ns, the high-intensity swirl became even more prominent. As the lifetime has increased, more electrons are alive resulting in a natural increase of the phase coherence and thus peak voltage.

The investigation of the radar signal properties of neutrino-induced particle cascades in this work already gives some insight into the most important physical effects that need to be considered. Still, more can be done as the simulations depend on a rather large amount of parameters. We, therefore, propose to investigate the effects of polarization and gain on the results presented in this thesis. It would be interesting to start working with a more realistic detector setup instead of the bistatic one we adopted. After completing this detailed study of the signal properties, it is only natural to start using these results in the pursuit of reconstructing the physical properties of the primary neutrino. The 2D peak frequency plot could perhaps help in the reconstruction of the arrival direction. We also found that the peak voltage scales linearly with the primary energy and thus could help in reconstructing the neutrino's energy.

Appendix A

Detailed outline of the MARES model

Before diving into the explanation of the model, some additional background information is given. The derivation of the electric field observed by the receiver antenna from all segments making up the ionization trail can be hard to follow if one is not familiar with radio antennas. Hence, the next section is written to support the derivation and make it more easy to follow. The outline of the MARES model in this appendix is written to give more details on the derivation than already given in the main text.

Background information

First, some widely used quantities and relations in antenna theory are discussed. Second, the mathematics of a damped-driven oscillation is outlined as this will become important later on in the derivation of the MARES model.

Important quantities and definitions: A good textbook regarding antenna theory can be found at [77] and is used as the main source in this section together with [87]. First, some qualitative definitions are given:

1. **Directivity** is the ratio of the power emitted by the antenna in a certain direction and the power emitted by an isotropically emitting antenna in that same direction. It is denoted by $D(\theta, \phi)$, where θ and ϕ are respectively the zenith and azimuth angles corresponding with standard spherical coordinates.

2. **Antenna efficiency** takes into account the losses in the antenna due to conductivity and dielectrics but also the mismatch between the antenna and the transmission line connecting it to the power source. It is denoted by e_0.

3. **Gain** is practically the same as the directivity but also considers the losses in the antenna. It is denoted as $G(\theta, \phi) = e_0 D(\theta, \phi)$.

4. **Effective area** is an important quantity in antenna theory. It can be understood using the interesting qualitative description adopted from [87]. Imagine a receiver antenna observing incident EM waves from a distant source. This antenna tries to capture the *EM wind* using a sail. Two factors determine how much of this EM wind can be captured by the sail: the size of the sail and the direction of the wind w.r.t. the sail. The bigger the sail is, the more efficient the receiver is at capturing the wind. Depending from which direction the wind blows, more or less wind gets caught into the sail. The effective area $A(\theta, \phi)$ of an antenna exactly expresses how much of this EM wind the antenna can capture originating from a certain direction. Hence, it is clear that the power at the receiver is given by [77]

$$P_R = A(\theta, \phi) W_i \tag{A.1}$$

   where W_i is the power density of the incident wave at the receiver.

5. **Radar cross-section** is a quantity defined for the specific situation in which the transmitted power is incident upon a target that is not the receiver antenna [77]. The radar cross-section σ_{RCS} as defined in [77]: "the area intercepting that amount of power which, when scattered isotropically, produces at

the receiver a density which is equal to that scattered by the actual target". Needless to say, in radar detection this is an important quantity.

It can be proven that there is a general relation between the maximum $A(\theta, \phi)$ and $D(\theta, \phi)$ of the transmitter and receiver antenna [77]:

$$\frac{D_{tm}}{A_{tm}} = \frac{D_{rm}}{A_{rm}} , \tag{A.2}$$

where the index m denotes the direction of the maximum and t and r respectively the transmitter and receiver. If the transmitter is an isotropic emitter, then the $D(\theta, \phi) = D_{tm} = 1$ and Equation (A.2) can be rewritten as

$$A_{tm} = \frac{A_{rm}}{D_{rm}} . \tag{A.3}$$

As this is a general relation, any type of receiver antenna can be used to calculate the effective area of an isotropic antenna. Typically the Hertzian dipole [87] can be used for this and the maximum effective area is found to be

$$A_{tm} = \frac{\lambda^2}{4\pi} , \tag{A.4}$$

where λ is the wavelength of the transmitted EM waves. By combining Equation (A.3) and (A.4) the maximum effective area for any antenna is found to be [77]

$$A_m = e_0 \left(\frac{\lambda^2}{4\pi}\right) D_m , \tag{A.5}$$

where immediately antenna losses are taken into account too. Finally, Equation A.5 can be generalised to any direction [77],

$$A(\theta, \phi) = e_0 D(\theta, \phi) \left(\frac{\lambda^2}{4\pi}\right) = G(\theta, \phi) \left(\frac{\lambda^2}{4\pi}\right) . \tag{A.6}$$

Another important quantity is the **radiated power** P_{rad} of an antenna. This value can be derived from integrating and averaging the instantaneous Poynting vector over a spherical surface [77, 87]:

$$p(t) = \oiint_S \left(\vec{E} \times \vec{H}^*\right) \cdot d\vec{S} , \tag{A.7}$$

where $\vec{E}$ is the electric component and $\vec{H}$ the magnetic component of the EM wave. In general for a Transversal Electromagnetic Wave (TEM) the electric and magnetic fields are perpendicular to one another and to the direction of propagation $\hat{k}$ such that it can be found that $|\vec{H}| = |\vec{E}|/Z$, where Z is the impedance of the medium [87]. Making the TEM assumption is in most cases justified when propagation freely without any boundaries. As such the TEM assumption is made from which it is found that

$$\begin{aligned} p(t) &= \oiint_S |\vec{E}||\vec{H}| \sin\theta \, \hat{k} \cdot \hat{n} \, dS \\ &= \oiint_S \frac{|\vec{E}|^2}{Z} dS , \end{aligned} \tag{A.8}$$

where $\hat{n}$ is the normal to the spherical surface S, $\hat{k} \parallel \hat{n}$ due to the isotropic emission and $\sin\theta = 1$ since $\vec{E} \perp \vec{H}$. Usually, the averaged radiated power is used by averaging $p(t)$ over one period of oscillation T,

$$\begin{aligned} P_{rad} &= \frac{1}{T} \int_0^T \oiint_S \frac{|\vec{E}|^2}{Z} dS \\ &= \frac{1}{T} \oiint_S \frac{1}{Z} \int_0^T |\vec{E}|^2 dS \\ &= \oiint_S \frac{E^2}{2Z} dS, \end{aligned} \tag{A.9}$$

where it was assumed that $\vec{E} = E \sin(\omega t - \vec{k} \cdot \vec{r})$ and the fact that the average over one period of oscillation of any $\sin^2$-function equals 1/2. From the above equation, it is clear that the radiated power density for any antenna is equal to

$$W_{rad} = \frac{E^2}{2Z} \ . \tag{A.10}$$

An isotropic antenna emits equally in all directions such that by definition

$$W_{rad} = \frac{P_{rad}}{4\pi R^2} \ , \tag{A.11}$$

where R is the distance to the source. If the equivalent wants to be found of the above equation for any antenna with a general gain pattern, from the definitions above it is found that

$$W_{rad} = \frac{P_{rad}}{4\pi R^2} G(\theta, \phi) \ . \tag{A.12}$$

By substituting Equation (A.10) into (A.12) an expression for the amplitude of the radiated electric field at a distance R from the source is found

$$|E_{rad}| = \sqrt{\frac{2ZP_{rad}G(\theta, \phi)}{4\pi R^2}} \ . \tag{A.13}$$

Damped-driven oscillation: A damped-driven oscillation is a more complex variant of the classical harmonic oscillator. Apart from having a restoring force bringing the object back to its equilibrium state, both a frictional and driving force are present as well. Hence, using Newton's second law the 1-dimensional equation of motion (e.o.m) becomes [88]

$$m\ddot{x} + b\dot{x} + kx = F(t) \ , \tag{A.14}$$

where m is the mass of the object, b the friction constant, k Hooke's constant and $F(t)$ the driving force. Before solving this differential equation it is rewritten such that the highest-order term has no constant in front of it,

$$\ddot{x} + \omega_c \dot{x} + \omega_0^2 x = f(t) \ , \tag{A.15}$$

where the collision frequency $\omega_c = b/m$, the natural frequency $\omega_0 = \sqrt{k/m}$ and $f(t) = F(t)/m$. Solving this differential equation is done through standard procedures for solving differential equations. As finding this solution is merely standard mathematics, the long derivation is omitted but can be found in [88], and only the result is stated. When the driving force is assumed to be given by $f(t) = f_0 \cos(\omega t)$ the solution to the e.o.m. is

$$x(t) = A \cos(\omega t - \delta) \tag{A.16}$$

where $A = \frac{f_0}{|\omega_0^2 - \omega^2 + i\omega_c|}$, $\delta = \arctan\left(\frac{\omega_c \omega}{\omega_0^2 - \omega^2}\right)$ [88]. In Figure A.1, the driving force and resulting solution to the e.o.m. are shown.

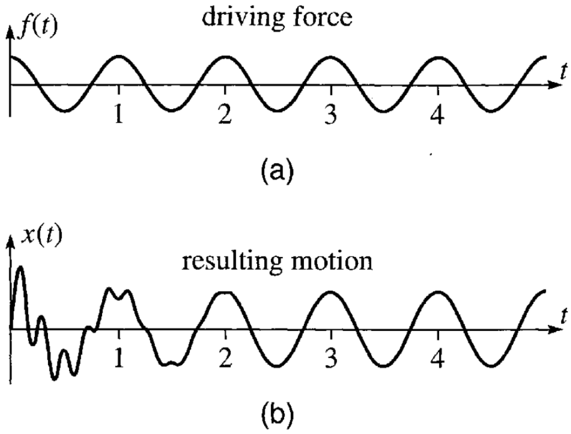

Figure A.1: The damped-driven oscillation of a test object with mass m subjected to a sinusoidal driving force. Panel (a) shows the driving force as a function of time. Panel (b) is the solution to the e.o.m. for the test object. Figure from [88].

Derivation

Finding the amplitude of a macroscopic segment $|E_{R,i}|$ can be done starting from the expressions in the previous section. From the definition of the radar cross-section, it is clear that the power captured by a single scatterer is given by

$$P_c = \sigma_{RCS} W_c \,, \tag{A.17}$$

where W_c is the captured power density. The power density captured by a segment is the same as emitted by the transmitter antenna. Hence, if the transmitter is non-isotropic then from Equation (A.12) it is found that

$$P_c = \sigma_{RCS} \frac{P_t}{4\pi R_T^2} G_T(\theta, \phi) \,, \tag{A.18}$$

where R_T is the distance between the transmitter and segment. The segment will scatter the captured power isotropically such that by using Equation (A.18)

$$W_s = \frac{P_c}{4\pi R_R^2} = \sigma_{RCS} \frac{P_T}{(4\pi R_T R_R)^2} G_T(\theta, \phi) \,, \tag{A.19}$$

where W_s is the scattered power density by the segment and R_R is the distance between the segment and the receiver. The power at the receiver can be found by using Equation (A.1), (A.6) and (A.19)

$$P_R = A_R W_s = P_T \frac{G_T(\theta, \phi) G_R(\theta, \phi) \lambda^2}{(4\pi)^3 (R_T R_R)^2} \sigma_{RCS} \,. \tag{A.20}$$

The above equation is also known as the **radar range equation** as it relates the transmitted power and the received power through a radar echo from a macroscopic object [77]. The radar range equation can be transformed into an expression for the received electric field amplitude using Equations (A.1) and (A.10)

$$\begin{aligned} \frac{E_R^2}{2Z_{ice}} A_R &= P_T \frac{G_T(\theta, \phi) G_R(\theta, \phi) \lambda^2}{(4\pi)^3 (R_T R_R)^2} \sigma_{RCS} \\ \Longleftrightarrow |E_R| &= \frac{\sqrt{2 Z_{ice} P_T G_T(\theta, \phi)} \sqrt{\sigma_{RCS}}}{4\pi R_T R_R} \,. \end{aligned} \tag{A.21}$$

The next step in the calculation is to determine the radar cross-section of the segment. This can be done by realizing that a segment consists of N_i electrons that are scattering the electric field from the transmitter.

An electron inside the ionization trail is subjected to the electric field of the transmitter whilst experiencing a frictional force due to sitting in ice. As such, the motion of the electron is modelled by a damped-driven oscillation, described in more detail in the previous section.

As the typical radio frequencies range between MHz and GHz, it is correct to assume that $\omega_c \gg \omega$ in the formulas of the damped-driven oscillation. On top of that, the natural frequency of the electron in this specific situation is zero. Hence, the e.o.m. of the electron, see Equation (A.16), becomes

$$x(t) = A\cos(\omega t - \delta) . \tag{A.22}$$

As the driving force originates from the electric field of the transmitter it is clear that $f_0 = (q|E_e|)/m$ and the amplitude A of the oscillation becomes

$$A = |x_e| = \frac{q|E_e|}{m}\frac{1}{|\omega^2 - i\omega\omega_c|} . \tag{A.23}$$

By defining the collisional ratio to be $W = 1/(|\omega^2 - i\omega\omega_c|)$, the solution to the e.o.m. of the electron is given by

$$x_e(t) = \frac{q|E_e|}{m}W\cos(\omega t - \delta) . \tag{A.24}$$

From the Liénard–Wiechert potentials, the general expression for the electric field of an accelerating charged particle can be found [38]

$$\vec{E}_{e,R} = \frac{q}{4\pi\epsilon_0}\frac{R_R}{(\vec{R}_R \cdot \vec{u})^3}[\vec{R}_R \times (\vec{u} \times \ddot{\vec{x}}_e)] , \tag{A.25}$$

Using the solution to the e.o.m. of the electron, the expression for the electric field is condensed into a more usable form:

$$\begin{aligned}
\vec{E}_{e,R} &= \frac{q}{4\pi\epsilon_0}\frac{R_R}{(\vec{R}_R \cdot \vec{u})^3}[\vec{R}_R \times (\vec{u} \times \ddot{\vec{x}}_e)] \\
&= \frac{q}{4\pi\epsilon_0}\frac{R_R}{c^3R_R^3}[\vec{R}_R \times (c\hat{R}_R \times \ddot{\vec{x}}_e)] \\
&= \frac{q}{4\pi\epsilon_0}\frac{1}{c^2R_R}[\hat{R}_R \times (\hat{R}_R \times \ddot{\vec{x}}_e)] \\
&= \underbrace{\frac{q^2}{4\pi\epsilon_0}\frac{1}{c^2m}}_{=r_e}\frac{\omega^2|E_e|W}{R_R}\sin\theta\hat{p}\ (\text{where } \hat{p} = \hat{R}_R \times (\hat{R}_R \times \ddot{\vec{x}}_e)) \\
&= \frac{|E_e|\omega^2W}{R_R}\left(\underbrace{\frac{3}{2}\sin^2\theta}_{=G_{Hz}}\underbrace{\frac{8\pi}{3}r_e^2}_{=\sigma_{Th}}\frac{1}{4\pi}\right)^{1/2}\hat{p} \\
&= \frac{|E_e|\omega^2W}{R_R}\left(\frac{\sigma_{Th}G_{Hz}}{4\pi}\right)^{1/2}\hat{p} .
\end{aligned} \tag{A.26}$$

Finally, by substituting the above equation into the radar range equation (A.21) and keeping in mind Equation (A.13), the radar cross-section of an electron is found to be

$$\sigma_{RCS,e} = (\omega^2W)^2\sigma_{Th}G_{Hz} . \tag{A.27}$$

From the coherence condition assumed in MARES between electrons within one segment it is found that the electric field at the receiver due to a single segment is

$$|\vec{E}_{R,i}| = |N_i\vec{E}_{e,R}| , \tag{A.28}$$

from which the radar cross-section of a segment can now be derived by substituting the above expression for the received electric field into Equation (A.21) and using the derived expression for $\sigma_{RCS,e}$ in Equation A.27

$$\sigma_{RCS,i} = N_i^2 \sigma_{RCS,e} \ . \tag{A.29}$$

The last remaining unknown is the amount of electrons in a segment N_i. Since the ionization trail is created by the particle cascade, parametrizing the latter allows for finding the electron distribution. The cascade is modelled using a parametrization for its longitudinal and radial profile separately. MARES uses the Greisen profile [78] for the longitudinal dimension of the cascade given by:

$$N(X, E_p) = \frac{0.31}{\sqrt{\ln\left(E_p/E_{crit}\right)}} e^{\frac{X}{X_0}(1-1.5\ln(s))} \ . \tag{A.30}$$

The radial profile is given by the Nishimura and Kamata parametrization [81]:

$$w(r, s) = \frac{\Gamma(4.5-s)}{\Gamma(s)\Gamma(4.5-2s)} \left(\frac{r}{r_0}\right)^{s-1} \left(\frac{r}{r_0}+1\right)^{s-1} \ , \tag{A.31}$$

In order to find the number of ionizing electrons, a mean ionizing energy is assumed together with a constant average energy loss for the cascade particles. This results in creating $N_{ion,e}dX$ ionization electrons per unit length X per cascade particle from which the electron density is found to be

$$n_{e,plasma}(X, r) \simeq \frac{N_{ion,e}dX}{dV} \int_r^{r+dr} N(X, E_p) w(r', s) dr' \ . \tag{A.32}$$

Before continuing to the phase information of the radar echo signal, it is important to make two additional corrections to the amplitude.

Finite lifetime of the plasma: The electrons inside the ionization trail have a finite lifetime and will recombine again with the ice molecules. In order to take this effect into account, the number of electrons in a segment of the cascade becomes time-dependent and is modified to

$$N_i(t, t_0) = N_{i,0} \cdot e^{-\frac{t-t_0}{\tau}} \Theta(t-t_0) \ , \tag{A.33}$$

where t is the time, t_0 is the time when the segment inside the ionization trail is created, τ the lifetime of the electrons and $\Theta(t)$ the Heaviside step function. The plasma lifetime is a function of the medium temperature and purity and is of the order $\tau \sim O(1-50)$ ns [12, 83]. The results of the electron density in Figure 4.2 is the $N_{i,0}$ in Equation (A.33) as the typical volume of a single segment in MARES is set to 1 cm^3.

Attenuation of the EM wave : Up until now, attenuation of the EM wave was not considered. Some of the EM wave's power will be lost when travelling from the transmitter to the ionization trail and subsequently from the trail to the receiver because the propagation is not in a vacuum but ice. These losses can be characterised by defining an attenuation length L_{att} and simply modifying the final amplitude $|E_{R,i}| = |E_{R,i}^{no\ att}| e^{-(R_T+R_R)/L_{att}}$. The attenuation length in ice is set in MARES to $L_{att} = 1.45$ km and is based on actual in-situ measurements of the average attenuation length of the Antarctic ice [82]. As RET is located in Greenland, this value can change when actual measurements are obtained for the Greenlandic ice. Note that the large attenuation length allows the radar detection technique to probe large volumes with little instrumentation in comparison to for example optical detection techniques used by IceCube. On top of that, a more subtle form of attenuation must be considered as well. Imagine the transmitted EM wave hitting the first segment inside the ionization trail. This segment scatters some of the original power of the EM wave away as discussed in the calculations above. Hence, the power reaching a second segment is slightly smaller than the first segment. This loss is taken into account in MARES by introducing a transparency factor $\mathcal{T}$ for each segment. Two different methods can be used to track the loss of power for consecutive segments and are fully explained in [12]. Only the results are stated in this work. The first microscopic approach starts from a single electron and the definition of work. In the end, the lost power density $P/V = \mathcal{P}_{loss} = I\beta$, where I is the irradiance of the incoming wave and $\beta = \frac{\omega_c}{c}(\omega\omega_p W)^2$, where ω_p is the plasma frequency. The second method uses a macroscopic approach and starts from the dispersion relation for the EM wave. The actual loss is found to be

$$P(l) = P_0 e^{\int_0^l -\beta(l')dl'} = P_0 \mathcal{T}, \tag{A.34}$$

where l is the length travelled through the ionization trail and $\beta = \frac{\omega_c}{c}(\omega\omega_p W)^2$ has the same definition as in the microscopic approach. From the above, it is once again found that the lost power density for a volume V of thickness l and area A is [12]

$$\begin{aligned} \mathcal{P}_{loss} &= \frac{\Delta P}{V} = \frac{1}{V} P_0 (1 - \mathcal{T}) \\ &= \frac{IA}{Al}(1 - e^{-\beta l}) \approx \frac{I}{l}\beta l = I\beta \, . \end{aligned} \tag{A.35}$$

As the transparency factor changes from segment to segment as well as the number of electrons, the attenuation correction and lifetime correction are included in the radar cross-section of the segment. As such Equation (A.29) becomes,

$$\begin{aligned} \sigma_{RCS,i}(t, t_0) &= N_{i,0}^2 e^{-\frac{2(t-t_0)}{\tau}} \Theta(t - t_0)\, \mathcal{T}\, \sigma_{RCS,e} \\ &= N_{i,0}^2 e^{-\frac{2(t-t_0)}{\tau}} \Theta(t - t_0)\, \mathcal{T}\, (\omega^2 W)^2 \sigma_{Th} G_{Hz} \, . \end{aligned} \tag{A.36}$$

Finally, the complete expression for the amplitude of the electric field at the receiver from a single segment is found by using the radar range equation (A.21), the corrected radar cross-section (A.36) and the first attenuation correction not yet included

$$|E_{R,i}| = \frac{\sqrt{2 Z_{ice} P_T G_T}}{4\pi R_T R_R} \sqrt{\sigma_{RCS,i}(t, t_0)}\; e^{-(R_T + R_R)/L_{att}} \, . \tag{A.37}$$

Finally, the electric field from the entire ionization trail at the receiver can be found by taking into account the phase information of the individual cascade segments, already discussed in the main text,

$$|E_{R,plasma}(R, t)| = \left| \sum_{i=1}^{M} E_{R,i}(R_i, t)\; e^{i(kR_i - \omega t + \psi)} \right| , \tag{A.38}$$

where $|E_{R,i}(R_i, t)|$ is given by equation (A.37).

Geometry and segmentation: To end the section about the MARES model, a final note must be given on the different reference frames considered and how the ionization trail is segmented. A total of three different reference frames are used and combined to calculate the radar echo from a particle cascade in MARES, shown in Figure A.2a. The first frame is called the bistatic scattering frame $\{\vec{e}_x, \vec{e}_y, \vec{e}_z\}$ and is defined by the transmitter and receiver locations [12]. In this reference frame, the transmitter antenna (TX) is located at the origin and the $\vec{e}_{rx} = \vec{e}_x$ vector points towards the receiver (RX). This frame is particularly useful for the calculation of the $\vec{E}_{R,plasma}(R, t)$ field as it was indirectly assumed throughout the entire calculation. The second reference frame is called the cascade frame $\{\vec{e}_L, \vec{e}_R, \vec{e}_n\}$ and has its origin at the cascade vertex $\vec{V}_{CS}$. This frame is used for the segmentation of the ionization trail. The trail gets sliced along the line of sight of the transmitter as illustrated in Figure A.2a. The third reference frame is called the plane of incidence frame $\{\vec{e}_U, \vec{e}_V, \vec{e}_W\}$ and is similar to the cascade frame. It is used to calculate the transparency factor $\mathcal{T}$.

The ionization trail gets sliced into parallel pieces along the line of sight of the transmitter in the cascade frame. Each of these slices is subsequently segmented into semi-circular rings with radial dimension Δr = 1 mm and longitudinal dimension ΔL = 1 cm as shown in Figure A.2b. These dimensions ensure the particle density within one segment is close to being constant and the segment is small enough to assume phase coherence. To speed up the numerical calculations in MARES, all semi-circular ring segments along a ray path are grouped into the position of the innermost ring and assumed to be coherent. This approximation introduces an error in the simulations, but as can be seen from Figure 4.2 most particles are close to the central cascade axis. Hence, this procedure only introduces a small error.

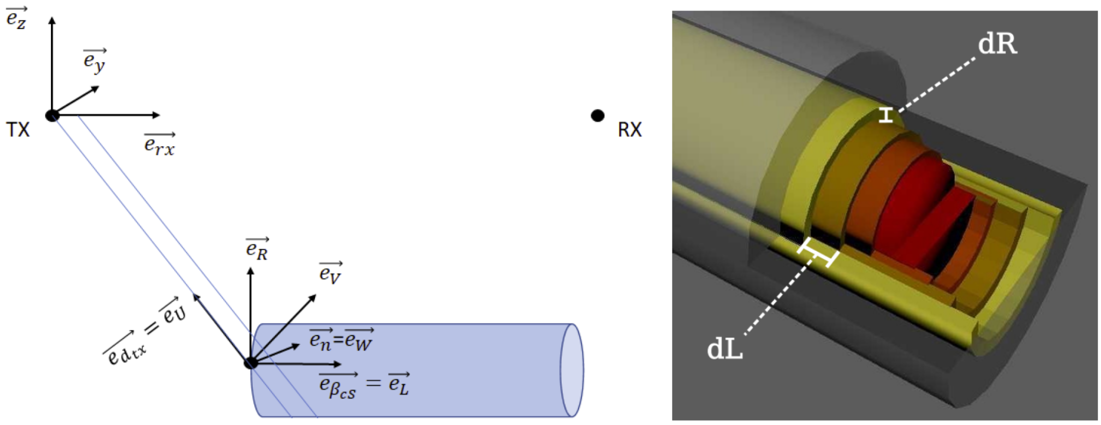

(a) (b)

Figure A.2: (a) Schematic overview of the three reference frames used in MARES. The transmitter (TX) and receiver (RX) are indicated by a black dot and the ionization trail by the cylinder. (b) An illustration of the segmentation in MARES using semi-circular rings. Figures from [12].

Appendix B

Relativistic Doppler effect

The relativistic Doppler effect is similar to the Doppler effect observed for sound waves. The difference between light and sound is that the former does not need a medium to propagate in. Hence, the formulas for the relativistic Doppler effect are different from the ordinary Doppler effect [85]. Deriving this Doppler shift can be done using the illustration shown in Figure B.1 and follows closely [85]. This derivation is done for light propagating in a vacuum. When a medium is considered, Cherenkov effects can come into play on top of the Doppler shift.

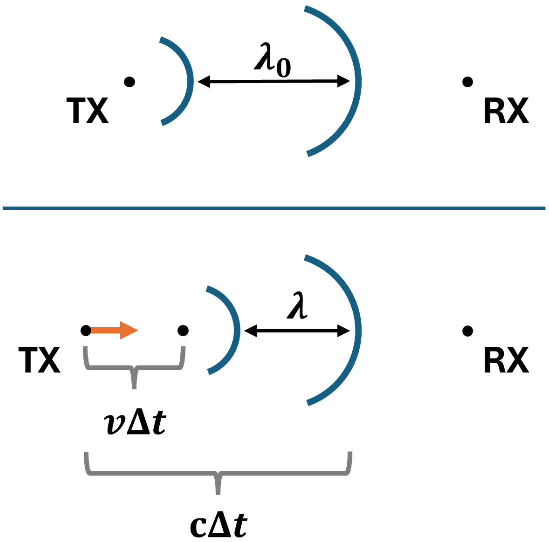

Figure B.1: *Top panel:* The source (TX) and observed (RX) are both at rest. *Bottom panel:* The source is moving towards the stationary observer at a speed v.

In the top panel of Figure B.1 a source of light (TX) is shown as having emitted two wave crests that are travelling towards an observed (RX). In this panel, both are at rest and the wavelength of the light emitted by the source is λ_0. This reference frame is called the lab frame. In the bottom panel of Figure B.1, the same setup is considered, but the light source is moving towards the receiver at a speed v. v is positively defined when the source moves towards the observer. This reference frame is called the observer frame. As illustrated in the figure, this implies that the source emits the second crest when it has moved a distance $v\Delta t$, where Δt is the time passed between the emission of the two crests. In the observer frame, the wavelength, being the distance between the crests, can be derived from geometrical arguments and becomes

$$\lambda = c\Delta t - v\Delta t \ . \tag{B.1}$$

The time Δt is the observed time interval in the observer frame. This interval experiences time dilation and from special relativity, it holds that [38]

$$\Delta t = \frac{\Delta t_0}{\sqrt{1 - v^2/c^2}} \,, \tag{B.2}$$

where Δt_0 is the time experienced in the source's rest frame, which corresponds with the lab frame. Hence Δt_0 is related to the wavelength in the lab frame as

$$\Delta t_0 = \frac{\lambda_0}{c} \,, \tag{B.3}$$

where the dispersion relation was used to transform from a frequency to a wavelength. Plugging in Equation (B.2) using Equation (B.3) into Equation (B.1) yields the expression for the observed wavelength,

$$\begin{aligned} \lambda &= (c - v)\frac{\Delta t_0}{\sqrt{c^2 - v^2}}\lambda_0 \\ &= \lambda_0\sqrt{\frac{c - v}{c + v}} \,. \end{aligned} \tag{B.4}$$

Using the classical dispersion relation this expression can be transformed into a frequency,

$$f = \frac{c}{\lambda} = f_0\sqrt{\frac{c + v}{c - v}} \,. \tag{B.5}$$

From these two equations, it becomes clear that $\lambda < \lambda_0$ or $f > f_0$ when the source is moving towards the observer. This is called a blueshift.

If the source is moving away from the observer it is clear that it suffices to replace $v \to -v$ in all the equations above to yield the expression for the observed wavelength,

$$\lambda = \lambda_0\sqrt{\frac{c + v}{c - v}} \tag{B.6}$$

and observed frequency,

$$f = f_0\sqrt{\frac{c - v}{c + v}} \,. \tag{B.7}$$

From these two expressions, it becomes clear that $\lambda > \lambda_0$ and $f < f_0$ when the source is moving away from the observer, resulting in what is called a redshift.

Appendix C

Angular plots

In Chapter 5, the azimuth plot was created to investigate the influence of the cascade direction on the peak voltage. As the zenith angle is kept fixed in the azimuth plot, it only probes a subspace of the entire phase space. In this appendix azimuth plots are produced for different zenith angles for completeness. As already mentioned in Chapter 5, a different approach is used to represent the peak voltage values for the entire phase space.

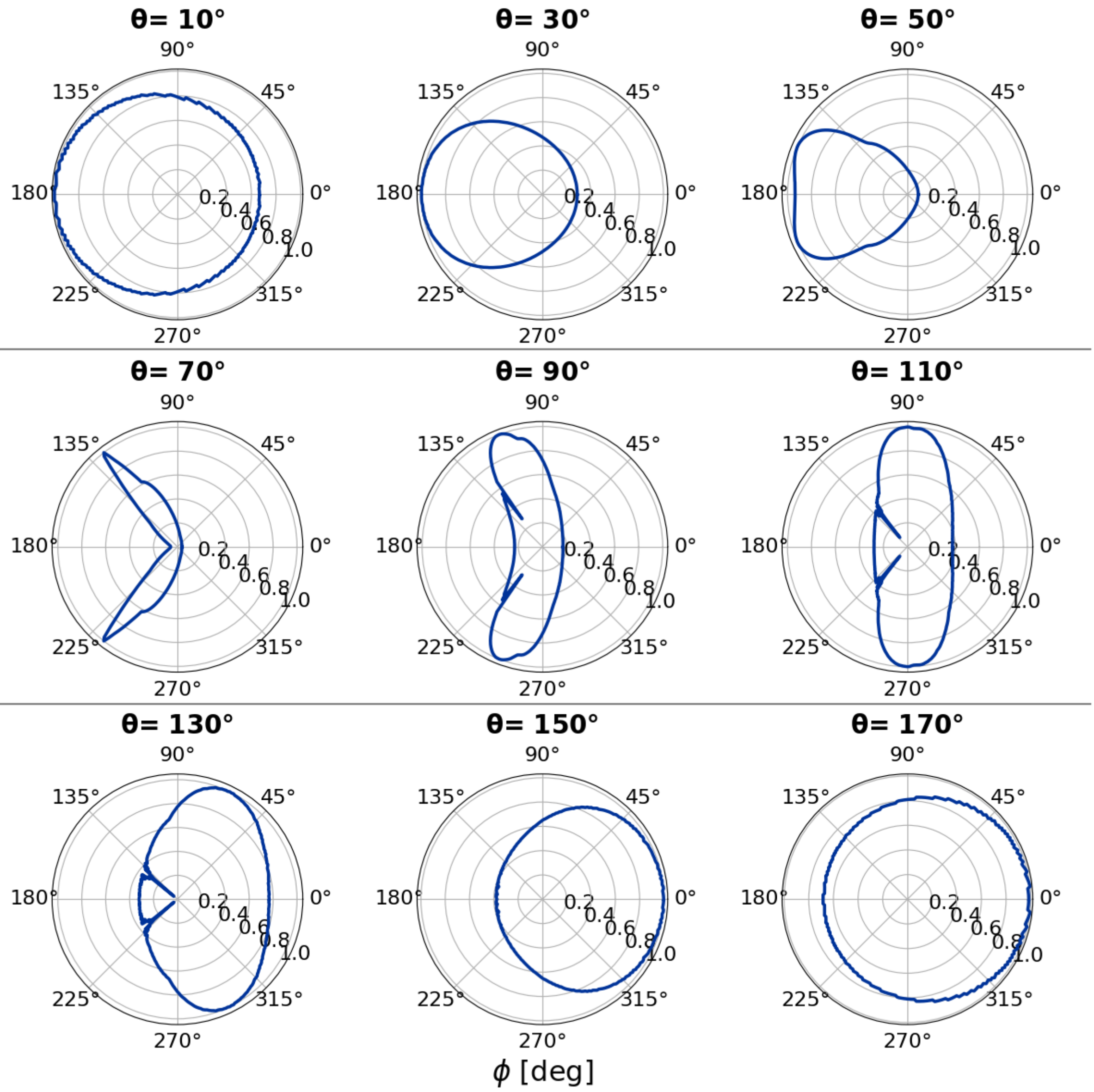

Figure C.1: An overview of azimuth plots for different zenith angles.

Appendix D

Nyquist theorem and aliasing

Assume a sine-wave function is sampled by N equally spaced points with sampling frequency f_s. When the signal is undersampled, meaning there are less than two points in one wavelength, a phenomenon called *aliasing* can occur [84]. Take, for example, a sine-wave with frequency 5 Hz that is sampled by a dataset with sample frequency $f_s = 25$ Hz as shown in Figure D.1a. This figure shows that the data is oversampled, meaning there are a sufficient amount of data points in one wavelength to correctly represent the sine wave. When a sampling frequency $f_s = 7$ Hz is chosen, the sine-wave is undersampled as shown in Figure D.1b. Consequently, this dataset is unable to reconstruct the original 5 Hz signal due to a loss of information. Instead, it represents a signal with a lower frequency as illustrated in Figure D.1b. Nyquist stated that there

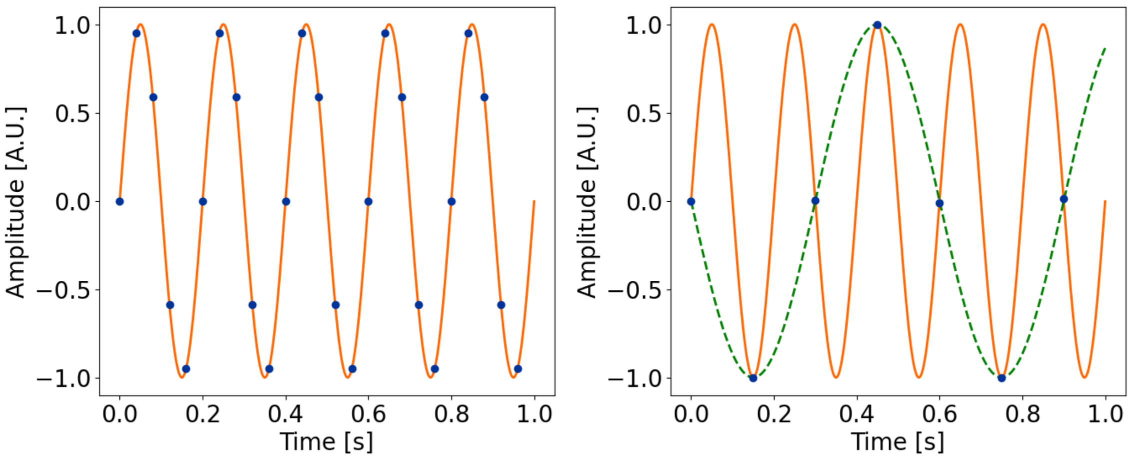

(a) (b)

Figure D.1: (a) A sine wave with frequency 5 Hz sampled with a dataset (blue dots) with sample frequency 25 Hz. (b) The green dashed line is a signal with frequency 5/3 Hz. This sine wave does not correspond to the original signal with a 5 Hz frequency, due to the phenomenon called aliasing. The signal takes on a wrong form due to the insufficient sampling frequency.

is no loss of information if the sampling frequency satisfies [84],

$$f_s \geq 2f_c \,, \tag{D.1}$$

where f_c is the highest frequency contained in the data. In the case of the previously given example, $f_c = 5$ Hz, the Nyquist theorem states that the $f_s \geq 10$ Hz. Since in Figure D.1b an insufficient sampling frequency $f_s = 7$ Hz was used to reconstruct the data, aliasing could occur due to a loss of information.

Appendix E

Single-slit experiment

When monochromatic light passes through a single slit with width D, a diffraction pattern arises on a screen behind it [85]. In this derivation, it is assumed that the distance between the source of the EM waves and the slit as well as the distance between the slit and the screen is large enough such that plane waves can be assumed and a ray description of light is used. This is also known as Fraunhofer diffraction [85] and simplifies the calculations. The condition assumed in Fraunhofer diffraction is that everything happens in the far field, implying that the distance R between the slit and the source is [85]

$$R > \frac{D^2}{\lambda}\,, \tag{E.1}$$

where λ is the wavelength of the monochromatic wave.

In Figure E.1 an illustration is shown explaining how a diffraction pattern is created at the screen behind the slit. The angle θ in this figure is defined as the angle between the rays and the line perpendicular to the screen. This angle will from now on be denoted in the text with ϑ to prevent confusion with the zenith angle. In panel (a), the parallel rays are passing straight through the slit and have the same path length.

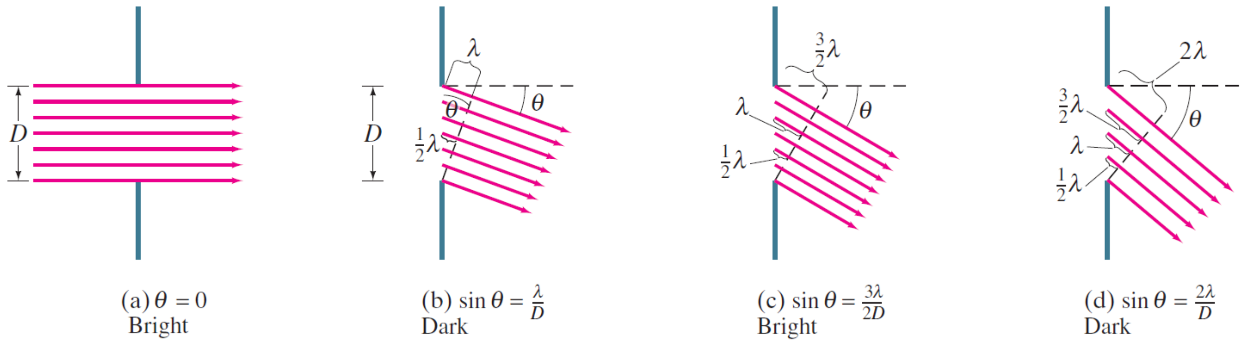

Figure E.1: Diffraction pattern formed by monochromatic light passing through a slit with width D from different angles. Figure from [85].

Because of that, all rays arrive in phase at the screen leading to a bright spot at an angle $\vartheta = 0°$. In panel (b), the rays are travelling at an angle ϑ such that the difference in path length between the top and bottom ray is exactly one wavelength λ. This implies that the middle ray in panel (b) needs to travel a distance $\lambda/2$ extra to reach the screen. Because of this extra travelled distance, the middle ray and bottom ray, which had originally the same phase at the slit, are out of phase when they reach the screen. In this scenario, the phase offset between the two rays leads to complete destructive interference. More of these pairs of rays can be identified in panel (b). For each ray a certain distance above the bottom ray, a ray at the same distance above the central ray exists that destructively interferes with it. Hence, when reaching the screen, all rays are destructively interfering leading to a dark spot. The location of this dark spot can be easily derived by looking at panel (b): $\sin\vartheta = \lambda/D$. An analogue argument can be used for any angle ϑ where the difference between the bottom and top ray is $m\lambda$ where m is an integer. This leads to the general formula for all locations of the dark spots on the screen [85]:

$$\sin\vartheta = m\frac{\lambda}{D} , \tag{E.2}$$

where $m = \pm 1, \pm 2$, etc. The distance between two local minima corresponds with the width of the diffraction band. It is clear that in $\sin(\vartheta)$-space, this width remains constant and is equal to λ/D. When measuring the distance in ϑ-space, the width of the bands will monotonically increase. This can be understood by considering the theoretical situation where $\lambda/D = 0.3$. The first three minima will be located at $\vartheta_1 = \sin^{-1}(0.3) = 17.46°$, $\vartheta_2 = \sin^{-1}(2 \cdot 0.3) = 36.87°$ and $\vartheta_3 = \sin^{-1}(3 \cdot 0.5) = 64.16°$. From these values, it is deduced that the width of the band between the first and second minimum and the second and third minimum is respectively given by $\Delta\vartheta_{2,1} = 19.41°$ and $\Delta\vartheta_{3,2} = 27.29°$.

Bibliography

[1] Mark Thomson. *Modern particle physics*. New York: Cambridge University Press, 2013. ISBN: 978-1-107-03426-6. DOI: 10.1017/CBO9781139525367.

[2] F. Reines and C. L. Cowan. “Detection of the Free Neutrino”. In: *Phys. Rev.* 92 (3 Nov. 1953), pp. 830–831. DOI: 10.1103/PhysRev.92.830.

[3] G Rajasekaran. *The Story of the Neutrino*. 2016. arXiv: 1606.08715 [physics.pop-ph].

[4] Matthias Vereecken. *Aspects of astrophysical particle production and beyond the Standard Model phenomenology*. 2019. arXiv: 1911.12244 [hep-ph].

[5] Giorgio Riccobene. “Novel Detection Techniques for High Energy neutrinos”. In: Dec. 2010, p. 054. DOI: 10.22323/1.103.0054.

[6] John David Jackson. *Classical electrodynamics*. 3rd ed. New York, NY: Wiley, 1999. ISBN: 9780471309321.

[7] M.G. Aartsen et al. “The IceCube Neutrino Observatory: instrumentation and online systems”. In: *Journal of Instrumentation* 12.03 (Mar. 2017), P03012–P03012. ISSN: 1748-0221. DOI: 10.1088/1748-0221/12/03/p03012.

[8] J. A. Aguilar et al. “Design and Sensitivity of the Radio Neutrino Observatory in Greenland (RNO-G)”. In: *JINST* 16.03 (2021). [Erratum: JINST 18, E03001 (2023)], P03025. DOI: 10.1088/1748-0221/16/03/P03025. arXiv: 2010.12279 [astro-ph.IM].

[9] S. Prohira et al. “Observation of Radar Echoes from High-Energy Particle Cascades”. In: *Phys. Rev. Lett.* 124 (9 Mar. 2020), p. 091101. DOI: 10.1103/PhysRevLett.124.091101.

[10] Krijn de Vries et al. “The Radar Echo Telescope for Neutrinos (RET-N)”. In: *Proceedings of 37th International Cosmic Ray Conference — PoS(ICRC2021)*. Vol. 395. 2021, p. 1195. DOI: 10.22323/1.395.1195.

[11] *RET official website*. URL: https://www.radarechotelescope.org/.

[12] E. Huesca Santiago et al. *MARES: A macroscopic approach to the radar echo scatter from high-energy particle cascades*. 2023. arXiv: 2310.06731 [astro-ph.HE].

[13] Vanessa Cirkel-Bartelt. “History of Astroparticle Physics and its Components”. In: *Living Reviews in Relativity* 11 (May 2008). DOI: 10.12942/lrr-2008-2.

[14] Claus Grupen. *Astroparticle Physics*. Springer, Jan. 2020. ISBN: 978-3-030-27341-5. DOI: 10.1007/978-3-030-27339-2.

[15] Claus Grupen. “Historical Introduction to Astroparticle Physics”. In: *Neutrinos, Dark Matter and Co.: From the Discovery of Cosmic Radiation to the Latest Results in Astroparticle Physics*. Wiesbaden: Springer Fachmedien Wiesbaden, 2021, pp. 1–10. ISBN: 978-3-658-32547-3. DOI: 10.1007/978-3-658-32547-3_1.

[16] Pierre Auger, Roland Maze, and Therese Grivet-Mayer. “Extensive cosmic showers in the atmosphere containing ultra-penetrating particles”. In: *Compt. Rend. Acad. Sci.(Ser. II)* 206 (1938), p. 1721.

[17] A. A. Penzias and R. W. Wilson. “A Measurement of Excess Antenna Temperature at 4080 Mc/s.” In: *Astrophysical Journal* 142 (July 1965), pp. 419–421. DOI: 10.1086/148307.

[18] Edward W. Kolb and Michael S. Turner. *The Early Universe*. Vol. 69. 1990. ISBN: 978-0-201-62674-2. DOI: 10.1201/9780429492860.

[19] R. A. Alpher, H. Bethe, and G. Gamow. “The Origin of Chemical Elements”. In: *Phys. Rev.* 73 (7 Apr. 1948), pp. 803–804. DOI: 10.1103/PhysRev.73.803.

[20] K. Hirata et al. "Observation of a neutrino burst from the supernova SN1987A". In: *Phys. Rev. Lett.* 58 (14 Apr. 1987), pp. 1490–1493. DOI: 10.1103/PhysRevLett.58.1490.

[21] Hans-Thomas Janka. "Neutrino Emission from Supernovae". In: *Handbook of Supernovae*. Springer International Publishing, 2017, pp. 1575–1604. DOI: 10.1007/978-3-319-21846-5_4.

[22] R. A. Perley et al. "THE EXPANDED VERY LARGE ARRAY: A NEW TELESCOPE FOR NEW SCIENCE". In: *The Astrophysical Journal* 739.1 (Aug. 2011), p. L1. ISSN: 2041-8213. DOI: 10.1088/2041-8205/739/1/l1.

[23] *Planck*. URL: https://www.esa.int/Enabling_Support/Operations/Planck.

[24] Jonathan P. Gardner et al. "The James Webb Space Telescope". In: *Space Science Reviews* 123.4 (Apr. 2006), pp. 485–606. ISSN: 1572-9672. DOI: 10.1007/s11214-006-8315-7.

[25] *The Hubble Space Telescope*. URL: https://science.nasa.gov/mission/hubble/.

[26] D. Christopher Martin et al. "The Galaxy Evolution Explorer: A Space Ultraviolet Survey Mission". In: *Astrophysical Journal, Letters* 619.1 (Jan. 2005), pp. L1–L6. DOI: 10.1086/426387. arXiv: astro-ph/0411302 [astro-ph].

[27] Martin C. Weisskopf et al. "Chandra X-ray Observatory (CXO): overview". In: *X-Ray Optics, Instruments, and Missions III*. Ed. by Joachim E. Truemper and Bernd Aschenbach. SPIE, July 2000. DOI: 10.1117/12.391545.

[28] David J. Thompson and Colleen A. Wilson-Hodge. "Fermi Gamma-Ray Space Telescope". In: *Handbook of X-ray and Gamma-ray Astrophysics*. Springer Nature Singapore, Nov. 2022, pp. 1–31. ISBN: 9789811645440. DOI: 10.1007/978-981-16-4544-0_58-1.

[29] Silvia Bravo. *Neutrinos and gamma rays, a partnership to explore the extreme universe*. Oct. 2016. URL: https://icecube.wisc.edu/news/research/2016/10/neutrinos-and-gamma-rays-partnership-to-explore-extreme-universe/.

[30] Pierre Auger Collaboration. "The Pierre Auger Cosmic Ray Observatory". In: *Nuclear Instruments and Methods in Physics Research A* 798 (Oct. 2015), pp. 172–213. DOI: 10.1016/j.nima.2015.06.058.

[31] Hiroyuki Sagawa. *Highlights from the Telescope Array Experiments*. 2023. arXiv: 2209.03591 [astro-ph.HE].

[32] Lars Mohrmann. "Characterizing cosmic neutrino sources". PhD thesis. Humboldt-Universität zu Berlin, Mathematisch-Naturwissenschaftliche Fakultät, 2015. DOI: http://dx.doi.org/10.18452/17377.

[33] M. Kachelriess. *Lecture notes on high energy cosmic rays*. 2008. arXiv: 0801.4376 [astro-ph].

[34] Elisabete M. de Gouveia Dal Pino et al. *Magnetic Reconnection, Cosmic Ray Acceleration, and Gamma-Ray emission around Black Holes and Relativistic Jets*. 2019. arXiv: 1903.08982 [astro-ph.HE].

[35] Stijn Buitink. *Lecture notes: High energy astrophysics.* Jan. 2021.

[36] J. Matthews. "A Heitler model of extensive air showers". In: *Astropart. Phys.* 22 (2005), pp. 387–397. DOI: 10.1016/j.astropartphys.2004.09.003.

[37] D. Bose et al. "Galactic and extragalactic sources of very high energy gamma rays". In: *The European Physical Journal Special Topics* 231.1 (Jan. 2022), pp. 27–66. ISSN: 1951-6401. DOI: 10.1140/epjs/s11734-022-00434-8.

[38] David J Griffiths. *Introduction to electrodynamics; 4th ed.* Re-published by Cambridge University Press in 2017. Boston, MA: Pearson, 2013. DOI: 1108420419.

[39] S.M. Bilenky. "Neutrino. History of a unique particle". In: *The European Physical Journal H* 38.3 (Dec. 2012), pp. 345–404. ISSN: 2102-6467. DOI: 10.1140/epjh/e2012-20068-9.

[40] Fred L. Wilson. "Fermi's Theory of Beta Decay". In: *Am. J. Phys.* 36.12 (1968), pp. 1150–1160. DOI: 10.1119/1.1974382.

[41] Oliviero Cremonesi. *Neutrino masses and Neutrinoless Double Beta Decay: Status and expectations*. 2010. arXiv: 1002.1437 [hep-ex].

[42] Poves Alfredo Giuliani Andrea. *Neutrinoless Double-Beta Decay*. 2012. DOI: 10.1155/2012/857016.

[43] Markus Steidl. *Experiments for the absolute neutrino mass measurement*. 2009. arXiv: 0906.0454 [nucl-ex].

[44] M Aker et al. "KATRIN: status and prospects for the neutrino mass and beyond". In: *Journal of Physics G: Nuclear and Particle Physics* 49.10 (Sept. 2022), p. 100501. ISSN: 1361-6471. DOI: 10.1088/1361-6471/ac834e.

[45] Rafael Alves Batista et al. "Open Questions in Cosmic-Ray Research at Ultrahigh Energies". In: *Frontiers in Astronomy and Space Sciences* 6 (June 2019). ISSN: 2296-987X. DOI: 10.3389/fspas.2019.00023.

[46] K. Mannheim and R. Schlickeiser. "Interactions of cosmic ray nuclei". In: *Astronomy and Astrophysics* 286 (June 1994), pp. 983–996. DOI: 10.48550/arXiv.astro-ph/9402042. arXiv: astro-ph/9402042 [astro-ph].

[47] Markus Ahlers and Francis Halzen. "Pinpointing extragalactic neutrino sources in light of recent IceCube observations". In: *Physical Review D* 90.4 (Aug. 2014). ISSN: 1550-2368. DOI: 10.1103/physrevd.90.043005.

[48] U.F. Katz and Ch. Spiering. "High-energy neutrino astrophysics: Status and perspectives". In: *Progress in Particle and Nuclear Physics* 67.3 (July 2012), pp. 651–704. ISSN: 0146-6410. DOI: 10.1016/j.ppnp.2011.12.001.

[49] Kenneth Greisen. "End to the Cosmic-Ray Spectrum?" In: *Phys. Rev. Lett.* 16 (17 Apr. 1966), pp. 748–750. DOI: 10.1103/PhysRevLett.16.748.

[50] G. T. Zatsepin and V. A. Kuzmin. "Upper limit of the spectrum of cosmic rays". In: *JETP Lett.* 4 (1966), pp. 78–80.

[51] A A Watson. "High-energy cosmic rays and the Greisen–Zatsepin–Kuz'min effect". In: *Reports on Progress in Physics* 77.3 (Feb. 2014), p. 036901. ISSN: 1361-6633. DOI: 10.1088/0034-4885/77/3/036901.

[52] Floyd W. Stecker. *Cosmological Neutrinos*. 2022. arXiv: 2203.17223 [astro-ph.CO].

[53] J. V. Jelley. "Cerenkov radiation and its applications". In: *British Journal of Applied Physics* 6.7 (July 1955), p. 227. DOI: 10.1088/0508-3443/6/7/301.

[54] Enrica Nappi and Jacques Seguinot. "Ring Imaging Cherenkov Detectors: The state of the art and perspectives". In: *Nuovo Cimento Rivista Serie* 28 (July 2005), pp. 1–130. DOI: 10.1393/ncr/i2006-10004-6.

[55] *An introduction to cherenkov radiation*. URL: http://large.stanford.edu/courses/2014/ph241/alaeian2/#:~:text=However%20if%20the%20particle%20moves,the%20direction%20of%20particle%20motion..

[56] R. Abbasi et al. "Evidence for neutrino emission from the nearby active galaxy NGC 1068". In: *Science* 378.6619 (Nov. 2022), pp. 538–543. ISSN: 1095-9203. DOI: 10.1126/science.abg3395.

[57] Morten Medici and for theIceCube Collaboration. "Indirect Dark Matter Searches with IceCube". In: *Journal of Physics: Conference Series* 1342.1 (Jan. 2020), p. 012074. DOI: 10.1088/1742-6596/1342/1/012074.

[58] IceCube Collaboration. *Measurement of atmospheric neutrino oscillation parameters using convolutional neural networks with 9.3 years of data in IceCube DeepCore*. 2024. arXiv: 2405.02163 [hep-ex].

[59] IceCube Collaboration et al. *The IceCube Neutrino Observatory - Contributions to ICRC 2017 Part II: Properties of the Atmospheric and Astrophysical Neutrino Flux*. 2017. arXiv: 1710.01191 [astro-ph.HE].

[60] G. A. Askar'yan. "Excess negative charge of an electron-photon shower and its coherent radio emission". In: *Zh. Eksp. Teor. Fiz.* 41 (1961), pp. 616–618.

[61] Maddalena Cataldo. "Status of RNO-G: Radio Neutrino Detector Greenland". In: *PoS* EPS-HEP2023 (2024), p. 076. DOI: 10.22323/1.449.0076.

[62] Pauline Harris and Rice Collaboration. "Radio Ice Cherenkov Experiment". In: *Astronomy, Cosmology and Fundamental Physics*. Ed. by Peter A. Shaver, Luigi Dilella, and Alvaro Giménez. Jan. 2003, p. 457. DOI: 10.1007/10857580_53.

[63] Kara Hoffman. "The Askaryan Radio Array (ARA)". In: *PoS* ICRC2021 (2022), p. 014. DOI: 10.22323/1.395.0014.

[64] Niraj Bhatta and Geetha Priya .M. "RADAR and its applications". In: 10 (Jan. 2017), pp. 1–9.

[65] Krijn D. de Vries, Kael Hanson, and Thomas Meures. "On the feasibility of RADAR detection of high-energy neutrino-induced showers in ice". In: *Astroparticle Physics* 60 (Jan. 2015), pp. 25–31. ISSN: 0927-6505. DOI: 10.1016/j.astropartphys.2014.05.009.

[66] Krijn D. de Vries et al. *On the Radar detection of high-energy neutrino-induced cascades in ice; From Radar scattering cross-section to sensitivity*. 2018. arXiv: 1802.05543 [astro-ph.HE].

[67] P. M. S. Blackett and A. C. B. Lovell. "Radio Echoes and Cosmic Ray Showers". In: *Proceedings of the Royal Society of London Series A* 177.969 (Jan. 1941), pp. 183–186. DOI: 10.1098/rspa.1941.0003.

[68] Bernard Lovell. "The Blackett-Eckersley-Lovell Correspondence of World War II and the Origin of Jodrell Bank". In: *Notes and Records of the Royal Society of London* 47.1 (1993), pp. 119–131. ISSN: 00359149. URL: http://www.jstor.org/stable/531399 (visited on 03/25/2024).

[69] A. C. B. Lovell, C. J. Banwell, and J. A. Clegg. "Radio echo observations of the Giacobinids meteors, 1946". In: *Monthly Notices of the Royal Astronomical Society* 107.2 (June 1947), pp. 164–175. ISSN: 0035-8711. DOI: 10.1093/mnras/107.2.164. eprint: https://academic.oup.com/mnras/article-pdf/107/2/164/8076905/mnras107-0164.pdf.

[70] E. V. Appleton and J. H. Piddington. "The Reflexion Coefficients of Ionospheric Regions". In: *Proceedings of the Royal Society of London. Series A, Mathematical and Physical Sciences* 164.919 (1938), pp. 467–476. ISSN: 00804630. (Visited on 03/25/2024).

[71] R. Abbasi et al. "Telescope Array Radar (TARA) observatory for Ultra-High Energy Cosmic Rays". In: *Nuclear Instruments and Methods in Physics Research Section A: Accelerators, Spectrometers, Detectors and Associated Equipment* 767 (2014), pp. 322–338. ISSN: 0168-9002. DOI: https://doi.org/10.1016/j.nima.2014.08.015.

[72] J. Stasielak et al. "Feasibility of radar detection of extensive air showers". In: *Astroparticle Physics* 73 (2016), pp. 14–27. ISSN: 0927-6505. DOI: https://doi.org/10.1016/j.astropartphys.2015.07.003.

[73] S. Prohira and D. Besson. "Particle-level model for radar based detection of high-energy neutrino cascades". In: *Nuclear Instruments and Methods in Physics Research Section A: Accelerators, Spectrometers, Detectors and Associated Equipment* 922 (2019), pp. 161–170. ISSN: 0168-9002. DOI: https://doi.org/10.1016/j.nima.2018.12.027.

[74] S. Prohira et al. "The Radar Echo Telescope for Cosmic Rays: Pathfinder experiment for a next-generation neutrino observatory". In: *Physical Review D* 104.10 (Nov. 2021). ISSN: 2470-0029. DOI: 10.1103/physrevd.104.102006.

[75] Wikipedia. *Scintillator — Wikipedia, The Free Encyclopedia*. http://en.wikipedia.org/w/index.php?title=Scintillator&oldid=1209209969. [Online; accessed 08-April-2024]. 2024.

[76] S. Agostinelli et al. "Geant4—a simulation toolkit". In: *Nuclear Instruments and Methods in Physics Research Section A: Accelerators, Spectrometers, Detectors and Associated Equipment* 506.3 (2003), pp. 250–303. ISSN: 0168-9002. DOI: https://doi.org/10.1016/S0168-9002(03)01368-8.

[77] C.A. Balanis. *Antenna Theory: Analysis and Design*. 3rd. Wiley-Interscience, 2012. ISBN: 9781118585733.

[78] G. Puppi, H.S. Bridge, and K. Greisen. *Progress in Cosmic Ray Physics. Vol. 3. Edited by J.G. Wilson ... Contributors: K. Greisen, H.S. Bridge, R.W. Thompson, G. Puppi*. North-Holland Publishing C°, 1956.

[79] Huege, T. and Falcke, H. "Radio emission from cosmic ray air showers - Coherent geosynchrotron radiation". In: *Astronomy & Astrophysics* 412.1 (2003), pp. 19–34. DOI: 10.1051/0004-6361:20031422.

[80] Krijn D. de Vries, Kael Hanson, and Thomas Meures. "On the feasibility of RADAR detection of high-energy neutrino-induced showers in ice". In: *Astroparticle Physics* 60 (2015), pp. 25–31. ISSN: 0927-6505. DOI: https://doi.org/10.1016/j.astropartphys.2014.05.009.

[81] Koichi Kamata and Jun Nishimura. "The Lateral and the Angular Structure Functions of Electron Showers". In: *Progress of Theoretical Physics Supplement* 6 (Feb. 1958), pp. 93–155. ISSN: 0375-9687. DOI: 10.1143/PTPS.6.93. eprint: https://academic.oup.com/ptps/article-pdf/doi/10.1143/PTPS.6.93/5270594/6-93.pdf.

[82] D.Z. Besson et al. “In situ radioglaciological measurements near Taylor Dome, Antarctica and implications for ultra-high energy (UHE) neutrino astronomy”. In: *Astroparticle Physics* 29.2 (2008), pp. 130–157. ISSN: 0927-6505. DOI: `https://doi.org/10.1016/j.astropartphys.2007.12.004`.

[83] Matthijs P. De Haas et al. “Nanosecond time-resolved conductivity studies of pulse-ionized ice. 1. The mobility and trapping of conduction-band electrons in water and deuterium oxide ice”. In: *The Journal of Physical Chemistry* 87.21 (1983), pp. 4089–4092. DOI: `10.1021/j100244a019`. eprint: `https://doi.org/10.1021/j100244a019`.

[84] P. C. Gregory. *Bayesian Logical Data Analysis for the physical sciences a comparative approach with Mathematica Support*. Cambridge University Press, 2005.

[85] Douglas C. Giancoli. *Physics for scientists and engineers with modern physics*. Pearson, 2009.

[86] Jan Danckaert. *Lecture notes: Vaste stof en stralingsfysica, Deel2: Elektromagnetisme*. Sept. 2020.

[87] Yves Rolain. *Lecture notes: Elektromagnetisme.* Aug. 2020.

[88] J.R. Taylor. *Classical Mechanics*. 1st. University Science Books, 2005. ISBN: 9781891389221.